Crashworthiness and Material Characterization of Multi-Cellular AA6063 Extrusions

by

Asmir Zhumagulov

A thesis

presented to the University of Waterloo

in fulfillment of the

thesis requirement for the degree of

Master of Applied Science

in

Mechanical and Mechatronics Engineering

Waterloo, Ontario, Canada, 2017

AUTHOR'S DECLARATION

I hereby declare that I am the sole author of this thesis. This is a true copy of the thesis, including any required final revisions, as accepted by my examiners.

I understand that my thesis may be made electronically available to the public.

Abstract

This thesis investigates the crashworthiness characteristics of the AA6063-T6 aluminum extrusions with two different multi-cellular cross-sections. The profiles under study are referred to as the Omega cross-section which is used in a commercially produced automobile and the UWR4 cross-section developed by Kohar et al. (Kohar C. Internationla Journal of Impact Engineering, vol 95, 2016) to improve the energy absorption properties of the axial rails. The aluminum profiles were crushed in the axial direction in dynamic and quasi-static crush modes. Peak loads, average crush loads, energy absorption and specific energy absorption of the different cross sections are then compared. Based on these comparisons, the UWR4 cross-section was found to display superior energy absorption properties compared to the Omega profile. Overall, the UWR4 profile developed by Kohar et al. improved the specific energy absorption of the rails (compared to the Omega cross-section) by 35.8% and 43.2% in dynamic and quasi-static axial crush experiments, respectively.

The aluminum alloy used in this work was studied for strain rate sensitivity through uniaxial tensile experiments in different strain rate regimes (10^{-3} s^{-1} – 10^{3} s^{-1}). These experiments are performed using miniature dog bone tensile samples developed to study strain rate sensitivity on various tensile frames. Simple shear experiments were also performed to better understand the hardening behaviour of the aluminum alloy. The results of these experiments were then used to model the constitutive behaviour of the alloy using a generalized Voce constitutive model.

The anisotropy of the aluminum alloy was characterized through tensile tests performed in the extrusion, diagonal and transverse directions. These experiments revealed the presence of a strong directional dependence of the mechanical properties of the alloy. The geometrical constraints of the rails made it impractical to utilize biaxial tension tests; instead, through-thickness compression tests were used to characterize the biaxial tension region of the yield surface. These results were then used to calibrate the YLD2000-2d anisotropic yield surface. The results of the yield surface fit showed a good agreement with the experimental values.

The results of the yield surface calibration along with the constitutive equation were used to model the dynamic and quasi-static axial crush experiments of the respective aluminum rails.

The results of the numerical models predicted the average loads of the aluminum rails within 10% of the experimental values. Some improvement in the predictions should be possible through the use of brick elements rather than the current shell elements.

Acknowledgements

Bismillah-irRahman-irRahim (*In the name of God, the most gracious, the most merciful*)

First and foremost, I would like to thank my supervisor, Dr. Michael Worswick, for the providing the great opportunity to contribute to this project as a part of his team. I would like to express my gratitude to him for the amount of supervision and support he put towards guiding me in this research.

I would like to acknowledge the support for this project by General Motors Canada - Automotive Partnership Canada (Grant No. 441668-12), Natural Science and Engineering Research Council, the Ontario Research Fund, the Canada Foundation for Innovation and the Canada Research Chairs Secretariat.

I would like to thank Dr. Jose Imbert and Mr. Jeff Wemp for all the help provided in performing axial crush experiments and making sure the safety is paramount.

I would like to thank Dr. Clifford Butcher for all the help and guidance he provided in fitting the constitutive behavior of the aluminum alloy. His meaningful discussions made it easier to correlate the experiments to the material modeling.

Thanks to Dr. Michael Nemcko for joining the project at the crucial time and doing a great job on fracture characterization on the material under study.

I would like to thank Armin Abedini, Kaab Omer, Sante DiCecco and Taamjeed Rahmaan for guidance and help in performing the experiments and adding meaning to use of the much loved DIC. Special thanks to Taamjeed Rahmaan for finding time to do the high rate tensile experiments.

These three years would not be as much fun without the company of other graduate students. Thanks for all the support and words of encouragement throughout this project: Sam Kim, Cale Peister, Jacqueline Noder, Cameron O'Keeffe, Kyu Bin Han, Pedram Samadian.

Dedicated to my loving family

Table of Contents

AUTHOR'S DECLARATION ii

Abstract iii

Acknowledgements v

List of Figures x

List of Tables xv

Nomenclature xvi

1 Introduction 1

1.1 Crashworthiness 2

1.2 Strain Rate Sensitivity 8

1.3 Anisotropy in Aluminum Alloys 10

1.4 Yield Functions 11

1.5 Fracture Modeling 16

1.6 Axial Crush Modeling 19

1.7 Summary of previous work and scope of the current work 20

2 Experimental Setup 22

2.1 Aluminum Extrusions 22

2.2 Material Characterization Experiments 24

2.2.1 Tensile Geometry 24

2.2.2 Low Strain rates – MTS apparatus 26

2.2.3 Intermediate Strain Rates - Hydraulic Intermediate Strain Rate Apparatus 27

2.2.4 High strain rate tensile testing 28

2.3 Shear experiments 28

2.4 Through-Thickness Compression Experiment 30

2.5 Digital Image Correlation 31

2.6 Crush Experiments 34
2.6.1 Dynamic Crush Setup 34
2.6.2 Quasi-Static Crush Setup 39
3 Experimental Results 41
3.1 Uniaxial Tensile experiments 41
3.2 Compression experiments 46
3.3 Strain rate sensitivity 49
3.4 Shear experiments 51
3.5 Crush Experiments 53
3.5.1 Dynamic axial crush 54
3.5.2 Quasi-static axial crush 62
3.6 Comparison of crush response of the Omega and UWR4 profiles 67
4 Axial Crush Model Development 72
4.1 Constitutive material model 72
4.1.1 YLD2000-2d 72
4.1.2 Hardening and strain rate sensitivity fitting 75
4.2 Axial crush simulations 79
4.2.1 Aluminum rail model 79
4.2.2 Fracture criterion 80
4.2.3 Mounting fixtures 83
4.2.4 The crash sled 84
4.2.5 Boundary conditions – dynamic axial crush 85
4.2.6 Boundary conditions – quasi-static axial crush 86
5 Modeling results 87
5.1 Omega profile axial crush model results 87

5.1.1 Dynamic axial crush 88
5.1.2 Quasi-static axial crush 90
5.2 UWR4 profile axial crush model results 95
5.2.1 Dynamic axial crush 97
5.2.2 Quasi-static axial crush 99
6 Conclusions and Recommendations 103
6.1 Conclusions 103
6.2 Recommendations 104
References 105

List of Figures

Figure 1 Folded axial rails a) model prediction b) experimentally folded rail [6] 2
Figure 2 Illustration of inextensional and extensional deformation paths [9] 3
Figure 3 Basic folding mode with continuous and smooth displacement field [9] 4
Figure 4 Specific energy absorptions of various types of columns [11] 5
Figure 5 Crush box profiles (left); Force-displacement curves for profiles under study [12] 5
Figure 6 Effect of mass and impact velocity on average dynamic load: constant velocity and varying mass (left); constant mass and varying impact velocity (right) [14] 6
Figure 7 Comparison of experimental and predicted flow stress ratios (left) and r-values (right) to the with respect to the tensile test directions for AA6063-T6 [30] 11
Figure 8 Isotropic yield loci corresponding to equation (8) for n values between 1 and 2.767 [37] 13
Figure 9 Damage evolution: (a) initial void, (b) void nucleation, (c) void growth, (d) void coalescence [44] 16
Figure 10 Damage element [45] 17
Figure 11 A comparison of force-displacement curves between experimental results and simulation results [39] 19
Figure 12 Extruded aluminum profiles (left-Omega, right-UWR4) 23
Figure 13 Through thickness texture of as received AA6063 aluminum extrusion [55] 24
Figure 14 Samples for experiments from top wall - baseline extrusion AA6063-T6 25
Figure 15 Tensile specimen geometries (a) JIS; (b) MJIS; (c) Mini-DB 26
Figure 16 Tensile sample geometry comparison 26
Figure 17 Tensile experiment setup on MTS tensile frame 27
Figure 18 HISR apparatus schematic [27] 28
Figure 19 Mini-Shear Specimen Geometry (All dimensions are in millimeters) [57][58] . 29
Figure 20 Shear experiment setup on MTS apparatus 30
Figure 21 Through-thickness compression test setup 30
Figure 22 Typical Speckle Patterns (not to scale) 32
Figure 23 Schematic of specimen mounted for impact test 35
Figure 24 Specimen mounted on wall 35

Figure 25 Omega (left) and UWR4 (right) bosses for rail mounts..... 36
Figure 26 Trigger system..... 38
Figure 27 Top (left) and side (right) views of the specimen from Photron cameras..... 38
Figure 28 Quasi-Static Crush Setup 39
Figure 29 AA6063-T6 tensile test results using MJIS samples (Extrusion Direction) 42
Figure 30 AA6063-T6 tensile test results using MJIS samples (Diagonal Direction) 42
Figure 31 AA6063-T6 tensile test results using MJIS samples (Transverse Direction) 43
Figure 32 DIC analysis images of tensile tests performed using MJIS samples (ED). Contours are of Hencky strain. 44
Figure 33 DIC analysis images of tensile tests performed using MJIS samples (DD). Contours are of Hencky strain. 44
Figure 34 DIC analysis images of tensile tests performed using MJIS samples (TD). Contours are of Hencky strain. 45
Figure 35 AA6063-T6 through-thickness compression test results 47
Figure 36 DIC image of though-thickness compression experiment. Contours are of Hencky strain. 48
Figure 37 DIC image of mini DB tensile experiment in extrusion direction (10^{-1} s^{-1}). Contours are of Hencky strain. 49
Figure 38 Strain rate sensitivity of the AA6063-T6 alloy in the extrusion direction. Note that the data at 1000 s-1 was provided by Rahmaan [71]..... 50
Figure 39 Strain rate sensitivity of the AA6063-T6 alloy in the diagonal direction 50
Figure 40 Strain rate sensitivity of the AA6063-T6 alloy in the transverse direction 51
Figure 41 Shear stress - shear strain response of AA6063-T6 alloy in the ED..... 52
Figure 42 Shear stress - shear strain response of AA6063-T6 alloy in the DD 52
Figure 43 The average shear stress - shear strain response of AA6063-T6 alloy ED *vs.* DD 53
Figure 44 Dynamic force-displacement curves for Omega AA6063-T6 rails 56
Figure 45 Dynamic energy absorption curves for Omega AA6063-T6 rails 56
Figure 46 Dynamic force-displacement curves for UWR4 AA6063-T6 rails 57
Figure 47 Dynamic energy absorption curves for UWR4 AA6063-T6 rails 58

Figure 48 UWR4 dynamic axial crush images from high-speed cameras. The circles highlight regions in which cracking was observed. 58
Figure 49 Dynamic force-displacement curves for Omega AA7003-T6 rails 60
Figure 50 Dynamic energy absorption curves for Omega AA7003-T6 rails 60
Figure 51 AA7003-T6 Omega extrusion dynamic axial crush images. The circles highlight regions in which cracking was observed. 61
Figure 52 Quasi-static force-displacement curves for Omega AA6063-T6 rails 62
Figure 53 Quasi-static energy absorption curves for Omega AA6063-T6 rails 63
Figure 54 Quasi-static force-displacement curves for UWR4 AA6063-T6 rails 64
Figure 55 Quasi-static energy absorption curves for UWR4 AA6063-T6 rails 64
Figure 56 Quasi-static axial crush of UWR4 AA6063-T6 aluminum rails 65
Figure 57 Quasi-static force-displacement curves for Omega AA7003-T6 rails 66
Figure 58 Quasi-static energy absorption curves for Omega AA7003-T6 rails 66
Figure 59 Quasi-static axial crush of Omega AA7003-T6 aluminum rails 67
Figure 60 Dynamic and quasi-static axial crush experiment summary – average loads 68
Figure 61 Dynamic and quasi-static axial crush experiment summary – peak loads 69
Figure 62 Dynamic and quasi-static axial crush experiment summary – absorbed energy 70
Figure 63 Dynamic and quasi-static axial crush experiment summary – specific energy absorbed 71
Figure 64 True stress *vs.* plastic work for tensile, compression and shear experiments 73
Figure 65 YLD2000 yield surface for AA6063-T6 alloy *vs.* isotropic Von-Mises 74
Figure 66 Normalized stress and r-value fits for YLD2000 plotted against material angle 75
Figure 67 True stress-plastic strain curves obtained from uniaxial tension and simple shear experiments 77
Figure 68 Generalized Voce model a) hardening behaviour b) strain rate sensitivity 79
Figure 69 Omega & UWR4 rail mesh broken into sections 80
Figure 70 Experimental GISSMO curve [52] 81
Figure 71 Sample geometries (a) mini shear, (b) hole tension, (c) regular notch, (d) plane strain notch [52] 82
Figure 72 Mesh regularization curve [54] 83
Figure 73 Omega and UWR4 fixture mesh 84

Figure 74 Axial crush model setup 85
Figure 75 Progressive folding of Omega rail (dynamic prediction) at various crush distances 87
Figure 76 Omega rails crushed dynamically: Experiment vs Numerical prediction 88
Figure 77 Predicted load-displacement curves for dynamic axial crush of Omega rails 89
Figure 78 Predicted energy-displacement curves for dynamic axial crush of Omega rails 90
Figure 79 Time scale factor vs. average crush load error convergence 90
Figure 80 CPU run time vs. time scale factor 91
Figure 81 Predicted load-displacement curves for quasi-static axial crush of Omega rails 92
Figure 82 Predicted energy-displacement curves for quasi-static axial crush of Omega rails 92
Figure 83 Omega axial crush: summary of model predictions and experiments – average loads 93
Figure 84 Omega axial crush: summary of model predictions and experiments – Peak loads 94
Figure 85 Omega axial crush: summary of model predictions and experiments – Absorbed energy 94
Figure 86 Progressive folding of UWR4 rail (dynamic prediction) at various crush distances 95
Figure 87 UWR4 rails crushed dynamically: Experiment vs Numerical prediction 96
Figure 88 UWR4 rails crushed quasi-statically: Experiment vs Numerical prediction 97
Figure 89 Predicted load-displacement curves for dynamic axial crush of UWR4 rails 98
Figure 90 Predicetd energy-displacement curves for dynamic axial crush of UWR4 rails 98
Figure 91 Predicted load-displacement curves for quasi-static axial crush of UWR4 rails 99
Figure 92 Predicted energy-displacement curves for quasi-static axial crush of UWR4 rails 100
Figure 93 UWR4 axial crush: summary of model predictions and experiments – Average loads 101
Figure 94 UWR4 axial crush: summary of model predictions and experiments – Peak loads 101

Figure 95 UWR4 axial crush: summary of model predictions and experiments – Absorbed energy 102

List of Tables

Table 1 Chemical Composition of AA6063 Aluminum Alloy (wt%) 23
Table 2 Normalized masses of aluminum extrusions 23
Table 3 Material characterization tests parameters 34
Table 4 Axial crush experiment matrix 40
Table 5 AA6063-T6 tensile experiment results 46
Table 6 r-values from through thickness compression experiments 48
Table 7 Crush experiment test parameters 54
Table 8 Omega AA6063-T6 dynamic axial crush summary 57
Table 9 UWR4 AA6063-T6 dynamic axial crush summary 59
Table 10 Omega AA7003-T6 dynamic axial crush summary 61
Table 11 Omega AA6063-T6 quasi-static axial crush summary 63
Table 12 UWR4 AA6063-T6 quasi-static axial crush summary 65
Table 13 Omega AA7003-T6 quasi-static axial crush summary 67
Table 14 Experimental stress ratios and Lankford parameters used for calibrating YLD2000-2d (taken at the plastic work level of 10.1 MJ/m^3) 73
Table 15 YLD2000 coefficients 75
Table 16 Generalized Voce model coefficients for AA6063-T6 alloy 78
Table 17 Profile shell thicknesses in crash modeling 80
Table 18 Steel elastic constants for rigid material model 83
Table 19 Coefficients of friction employed in the LS-Dyna models 86

Nomenclature

σ_{true}	True stress
A	Yield stress (Johnson-Cook model)
B	Hardening constant (Johnson-Cook model)
C	Strain rate sensitivity constant (Johnson-Cook model)
n	Hardening exponent (Johnson-Cook model)
$\dot{\varepsilon}^*$	Normalized strain rate
$\dot{\varepsilon}_0$	Strain rate in the reference direction
ε_p	Equivalent plastic strain
$\Delta\sigma_G$	Stress component independent of temperature (Zerilli-Armstrong model)
$\sigma_{THERMAL}$	Stress component correcting for temperature and strain rate (Zerilli-Armstrong model)
C_2	Material constant (Zerilli-Armstrong model)
C_3	Material constant (Zerilli-Armstrong model)
T	Absolute temperature
σ_{sat}	Saturation stress (Voce model)
σ_y	Yield Stress
ε_r	Relaxation strain (Voce model)
D	Strain rate parameter (Voce model)
$\sigma_1, \sigma_2, \sigma_3$	Principal stress
m	Yield function material coefficient
$\bar{\sigma}$	Effective flow stress
H, F, G, N, L, M	Material parameters for Hill48 yield function
a, c, h, p	Material constants for Barlat 89 yield function
ϕ	Plane stress yield criterion (Yld2000-2d)
ϕ', ϕ''	Linearly transformed isotropic functions (Yld2000-2d)
X_i', X_i''	Principal stresses of linearly transformed Cauchy stress (Yld2000-2d)
$L',\ L''$	Linear transformation tensors (Yld2000-2d)
$\alpha_1 - \alpha_8$	Yld2000-2d coefficients

D	Damage parameter
S	Total area of representative unit volume
S_D	Area of cavities in a representative unit volume
ε_f	Equivalent plastic strain at fracture
η	Stress triaxiality
ξ	Lode parameter
h	Hencky strain
U	Right stretch component of deformation gradient
F	Deformation gradient
R	Rotation tensor
r_θ	Lankford (r-value) parameter (angle θ with respect to extrusion direction)
ε_θ^w	Width strain (angle θ with respect to extrusion direction)
ε_θ^t	Thickness strain (angle θ with respect to extrusion direction)
r_b	Biaxial (r-value)
ε_{TD}	Strain in transverse direction (with respect to extrusion direction)
ε_{ED}	Strain in extrusion direction
τ	Shear stress
F_{shear}	Shear load
A_{shear}	Area of the shear region
L_{shear}	Length of the shear region
t_{shear}	Thickness of the shear sample
v	Sled velocity
d	Axial crush displacement
$E_{(l)}$	Energy absorbed during axial crush of rail at crush distance *l*
F_{ave}	Average axial crush load
E_{SEA}	Specific absorbed energy
$m_{(l)}$	Mass of the rail corresponding to crush distance *l*
W_p	Plastic work
R_θ	Stress ratio (with respect to reference direction)

σ_θ	Flow stress (angle θ with respect to extrusion direction)
σ_{0^o}	Flow stress in the extrusion direction
G	Shear modulus
$\beta_1 - \beta_4$	Generalized Voce coefficients (hardening behavior)
a, b, c	Generalized Voce coefficients (strain rate sensitivity)

1 Introduction

The current trend in the automotive industry to reduce vehicle emissions has resulted in significant interest in the use of lightweight materials for vehicle structural components. Such lightweight materials include advanced high-strength steels, aluminum and magnesium alloys and composite materials. Of these, aluminum alloys offer high strength-to-density ratio and good corrosion resistance. Another advantage of using aluminum alloys is the low energy requirements to recycle the material, which offers good sustainability. The current thesis addresses the use of extruded aluminum alloys in crush regions of automotive structures, in particular focussing on frontal crush boxes which are required to absorb crash energy.

Due to the crystallographic texture resulting from the extrusion process, aluminum alloys show strong anisotropy in their mechanical properties. For example the yield strength and Lankford coefficient (r-value) display significant variations when measured along different orientations with respect to the extrusion direction [1]. The mode of the deformation during the extrusion process generally results in orthotropic symmetry.

During the dynamic axial crush, the strain rate at the folds can reach up to 500/s [2], thus it is important to understand the effect of strain rate on stress-strain response. In addition, aluminum alloys are susceptible to fracture at large strains which can greatly reduce the energy absorbing properties of the crush rail. As a consequence, energy-absorbing structures have to be tested to assess the fracture caused by the geometrical constraints [3].

The crush mechanics of lightweight structures has been studied extensively in the last several decades. Understanding crush mechanics has allowed use of optimization software along with artificial intelligence algorithms to improve the crashworthiness of energy absorbing structures [4]. Kohar *et al.* [4] developed a framework for optimizing the sizing of multi-cellular aluminum alloy extrusions for automotive crashworthiness applications. The axial rails were extruded from AA6063 and AA7xxx aluminum alloys in T6 temper conditions. The aim of this thesis is to assess the crashworthiness of these profiles and characterize the strain rate sensitivity and anisotropy of the material. The balance of this chapter reviews relevant literature concerning axial crush elements in crashworthiness applications, as well as material modelling for crash safety prediction.

1.1 Crashworthiness

The design of new automotive structural components has to be balanced with crashworthiness assessment to ensure passenger safety in the event of a crash. The front rails of a vehicle structure play an important role in energy absorption management during a head-on collision. While these components have to be strong enough to minimize the crush distance, they have to plastically deform in a controlled manner to reduce the force transferred to the passenger [5].

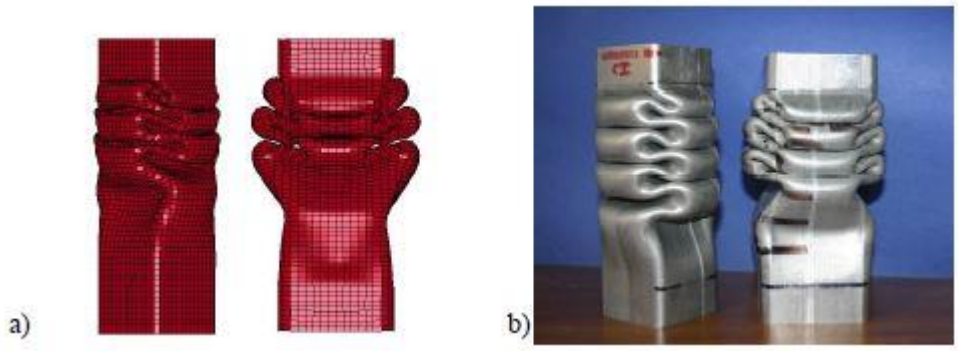

Figure 1 Folded axial rails a) model prediction b) experimentally folded rail [6]

Early work aimed to understand the crush mechanics in thin walled structures was done by Alexander in 1960 [7] for cylindrical shells. In this work, Alexander proposed an approximate equation for calculating the mean force required to form a symmetric fold, which resulted in good predictions compared to the experiments. Wierzbicki and Abramowicz in 1983 [8] experimented with rectangular shells and developed a theory for fold formation during a progressive collapse. In this work, Wierzbicki and Abramowicz have divided the rectangular cross-section into four identical two-flange corners. The main assumptions in this work were that the folds develop progressively; the wavelength within each fold stays constant. Further simplifications to the problem involved assuming a rigid-perfectly plastic isotropic material model. The energy dissipated during the fold formation was related to the localized inextensional and extensional deformation at each corner. The definitions of extensional and inextensional modes of deformation are given in work by Hayduk and Wierzbicki (1983) [9].

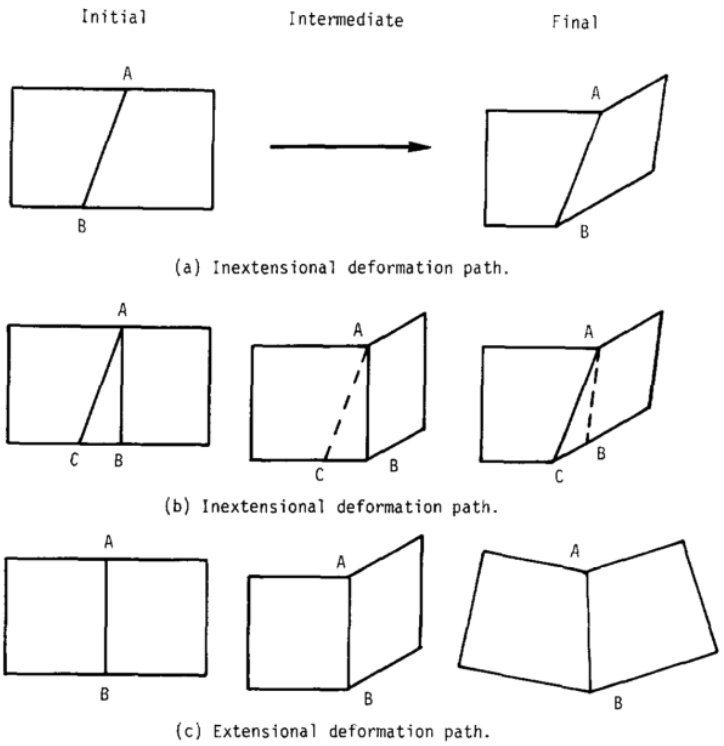

Figure 2 Illustration of inextensional and extensional deformation paths [9]

In Figure 2a, a flat element is folded along line AB (which is considered to be inextensible) to a final state. The same state can be achieved by folding along AB initially and along lines AB and AC simultaneously as illustrated in Figure 2b. These deformations are inextensional as well. An extensional deformation mode is shown in Figure 2c, where the initial flat element is folded inextensibly as in previous cases, followed by two halves rotating extensibly to come to the final shape.

The relevance of extensional and inextensional modes of deformation can be seen on an example of a basic folding element shown in Figure 3. The folding element consists of four different sections [9]. Section I consists of a trapezoidal element that moves as a rigid body. Section II consists of a cylindrical surface which bends inextensionally. Section III consists of a conical surface that bends and re-bends as the fold progresses. Section IV is made of a toroidal surface that produces extension in a circumferential direction.

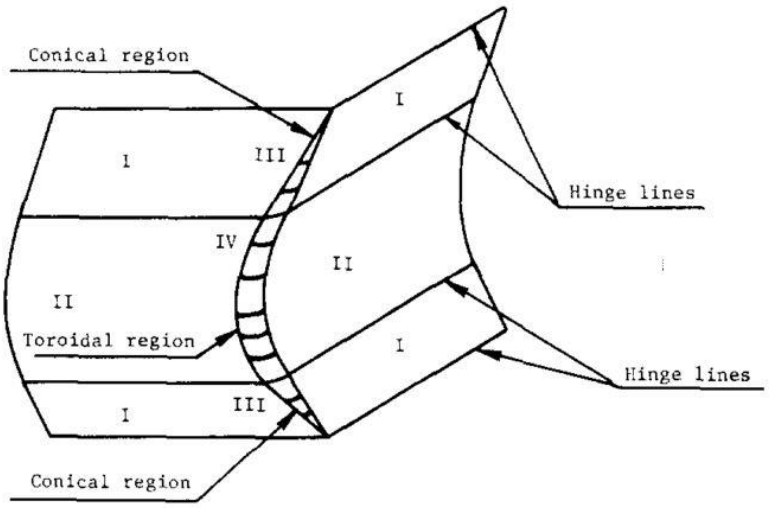

Figure 3 Basic folding mode with continuous and smooth displacement field [9]

It was concluded that the extensional deformations contribute to one-third and the inextensional deformations contribute to as much as two-thirds of the total dissipated energy. Later, in 1989, Abramowicz *et al.* extended this work, and proposed a folding mechanism for multi-corner tubes with arbitrary angles [10]. In this work, mean crush force equations for square, hexagonal, and rhomboidal columns were presented. The main conclusion from this work was that the plastic resistance, as well as the collapse mode, was strongly dependent on the angle between intersecting plates (i.e. corner angle). For acute angles, the deformation mode is quasi-inextensional, whereas, for the obtuse angles, the deformation mode is extensional. The importance of the deformation mode is given by the calculation showing that the extensional mechanism of deformation provides 30% less energy absorption compared to the quasi-inextensional deformation [10]. Later works by Chen and Wierzbicki[11] have compared the response of single and multiple cell crush boxes with and without foam filler. The findings reveal that the foam filled crush boxes are more efficient in absorbing energy compared to the ones without. The specific energy absorption of various types of crush boxes is shown in Figure 4. An interesting observation from this study is the absence of improvement in specific energy absorption between double and triple cell crush columns.

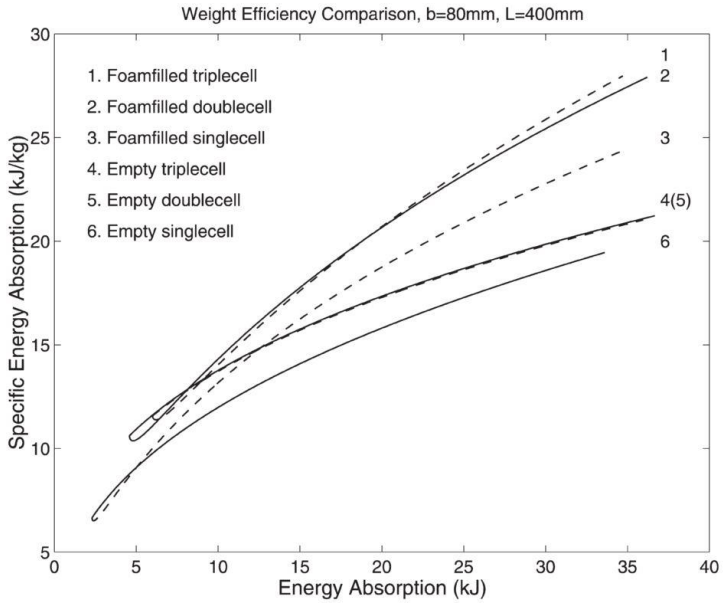

Figure 4 Specific energy absorptions of various types of columns [11]

Kim[12] studied various extruded multi-cell aluminum profiles for maximum energy absorption. The multi-cell cross section rail had 1.9 times the specific energy absorbed of the simple square crush column. The profile geometries and performance of the profiles in terms of force-displacement curves are shown in Figure 5.

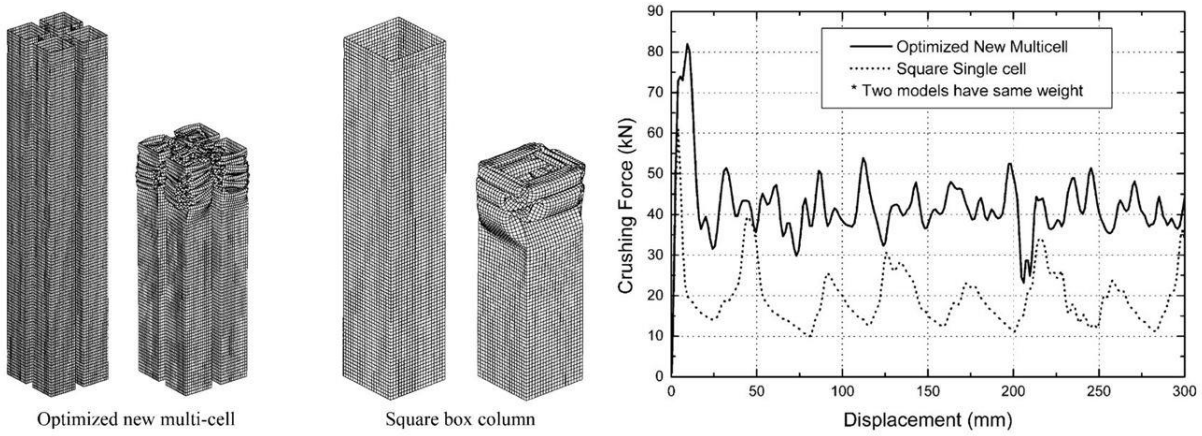

Figure 5 Crush box profiles (left); Force-displacement curves for profiles under study [12]

More recently, Najafi *et al.* have improved analytical predictions of axial crush predictions for multi-cell, multi-corner tubes [5]. Most of the analytical solutions were considered only for static loading and did not take into account the inertial effects. Langseth and Hopperstad [13] performed extensive experiments on aluminum extrusions with rectangular cross-section made of AA6060 alloy. The main variables of these experiments were the heat treatment and axial impact mode. They concluded that the impact mode (static *versus* dynamic) affects the crushing mode (symmetric *versus* non-symmetric) as well as the mean crushing force. The alloy chosen for the experiments was essentially strain rate insensitive, which led to a conclusion of a strong presence of inertial effects during dynamic axial crush. In subsequent work, Langseth *et al.* [14] experimented with varying impactor mass and impact velocity. It was concluded that varying the mass while keeping the impact velocity constant, does not have a significant impact on the resultant peak and average loads. On the other hand, with increasing velocity, while keeping the mass of the impactor constant, the peak, and average loads tend to increase as well. In the same work, the LS-DYNA explicit dynamic finite element code was used to simulate the axial crush of the square tubes. The authors used an isotropic material behavior obeying the Von-Mises yield criterion, along with isotropic hardening. Their numerical simulation results had a fair agreement with experimental results, with peak, and average loads predicted within 10% [14].

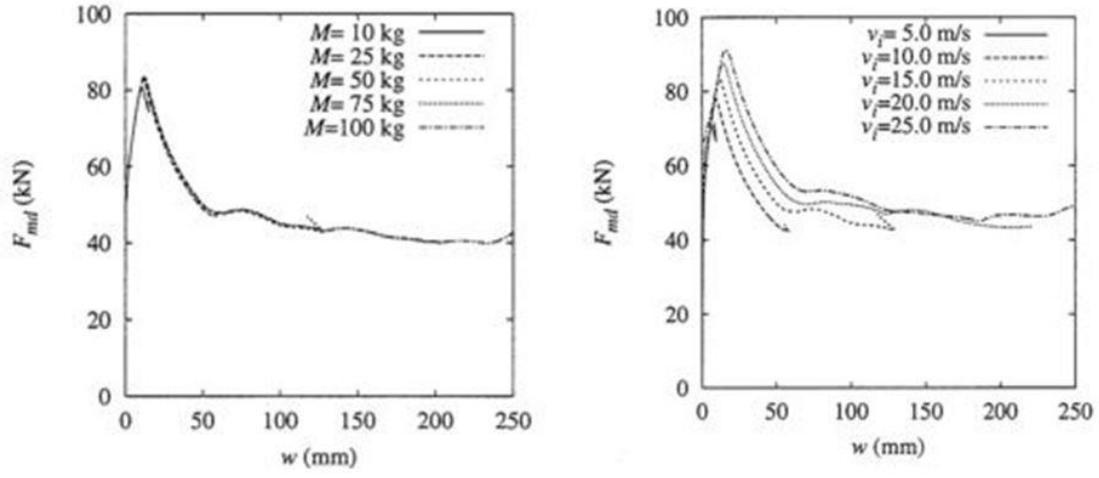

Figure 6 Effect of mass and impact velocity on average dynamic load: constant velocity and varying mass (left); constant mass and varying impact velocity (right) [14]

The crash performance of energy absorbing structures made of various steels and aluminum alloys has been studied extensively in the last three decades. Hsu and Jones [15]

studied quasi-static and dynamic axial crush response of thin-walled circular tubes made of stainless steel, mild steel, and AA6063-T6 aluminum alloy. Their experimental program involved parametric studies around the effects of tube length on the stability of the energy absorber during deformation. This study revealed that although tubes made of aluminum alloys absorbed the least amount of total energy, they are more efficient compared to steels in absorbing more energy per unit mass. The specimen lengths where the deformation mode changes from progressive folding to a global buckling was identical for all three materials [15].

Omer *et al.* [16] have investigated the effect of tailoring the properties of hot stamped axial crush rails on their energy absorption properties. In this work, Omer *et al.* compared non-tailored axial rails to rails with three different tailoring conditions where one half of the rails was quenched and the other half was formed at temperatures between 400 C^o and 700 C^o. The three tailoring conditions were forming at 400 C^o, 700 C^o, and a graded soft zone where the temperature ranged from 400 C^o to 700 C^o (graded soft zone). The axial crush experiments showed that tailoring the rails had positive impact on energy absorbed by the rail as well as the extent of fracture. The non-tailored rails absorbed the most energy; however, had the largest extent of fracture compared to the tailored rails. The greater extent of fracture in the rails resulted in a poor repeatability between the experiments. Among the tailored rails, the ones containing a graded soft zone showed high energy absorption as well as the least amount of fracture and global buckling [16].

Williams *et al.* assessed the crashworthiness characteristics of straight section hydroformed aluminum tubes made of EN-AW 5018 aluminum alloy [17]. The results of this study revealed the importance of carrying forward the forming history variables such as residual stresses, tubes thickness, and work hardening. The numerical model using Von-Mises yield criterion resulted in consistently over-predicted mean loads compared to those measured experimentally. Williams *et al.* recommended to focus on material anisotropy and fracture characterization to improve the accuracy of numerical predictions [17]. Similar conclusions were achieved by Grantab *et al.* [18] in his paper on numerical modeling of dual crush mode welded aluminum crash structure.

1.2 Strain Rate Sensitivity

As was mentioned earlier, the strain rate in the fold regions of the axial rails can reach 500/s [2]. Generally, aluminum alloys do not exhibit strong strain rate effects in the range of 10^{-4}-10^{3} s^{-1} [19]. Previous studies on aluminum alloys show that the strain rate sensitivity of the alloys depends on the alloying elements and in some cases on the heat treatment. Mukai *et al.* [20] studied the strain rate sensitivity of a high purity Al-Mg alloy with varying magnesium weight percentage. The tensile tests with strain rates ranging from 10^{-4} s^{-1} to 10^{-1} s^{-1} showed that the maximum flow stress decreases for Al-Mg alloys for strain rates below 10^{1} s^{-1}, but increases again above this rate [20]. Rahmaan et al. [21] found a similar transition between negative rates sensitivity for rates below 1 s^{-1}, and positive rate sensitivity for higher rates. They demonstrated that the rate sensitivity at lower rates is due to dynamic strain gaining and PLC band propagation which is suppressed at higher rates. Smerd *et al.* [19] also reported low rate sensitivity for 5000 series aluminum alloys. The strain rate sensitivity (increase in flow stress) of AA6060 in the strain rate regime ranging from 10^{-4} s^{-1} to 10^{3} s^{-1} is estimated to be 5-10% [13].

Over the years, many constitutive equations have been developed to describe the strain rate sensitivity of metals such as the models due to Johnson-Cook [22], and Zerilli-Armstrong [23], as well as modified rate sensitive versions of the Voce model [24]. These constitutive equations typically express flow stress as a function of strain, strain rate, and temperature. In 1983, Johnson and Cook [22] presented a constitutive model derived based on experimental results from 12 different materials. Their equation is given in the form:

$$\sigma_{true} = (A + B\varepsilon_p^n)(1 + Cln(\dot{\varepsilon}^*))(1 - T^{*m}) \quad (1)$$

where σ_{true} is the true stress, ε is the equivalent plastic strain, $\dot{\varepsilon}^* = \dot{\varepsilon}/\dot{\varepsilon}_0$ is a normalized strain rate in which the reference strain rate is $\dot{\varepsilon}_0$, and the last term in the equation captures the thermal softening of the material. $A, B, C, n,$ and m are material constants. A is the yield stress of the material, B and n represent the hardening behavior, C represents the strain rate sensitivity, and m describes the material softening. In some cases, the Johnson-Cook model fails to describe strain rates of complex materials due to the simplified multiplicative coupling of hardening rate, thermal softening response, and strain rate terms [25].

In the Zerilli-Armstrong material model the effects of the strain hardening, strain rate, and thermal softening are incorporated into a constitutive relation based on thermal activation analysis [23]. The general form of the equation is given as:

$$\sigma = \Delta\sigma_G + \Delta\sigma_{THERMAL} + kl^{-1/2} \quad (2)$$

where σ is the Von-Mises stress, $\Delta\sigma_G$ constitutes the athermal components of the stress, term $kl^{-1/2}$ takes into account the grain size of the material, and $\Delta\sigma_{THERMAL}$ takes into account temperature and strain rate effects on the flow stress. The Zerilli-Armstrong model is expected to be applied to materials under high strain rates and relatively low temperatures [23]. In this work, Zerilli and Armstrong proposed different equation forms for the $\sigma_{THERMAL}$ component depending on the material crystallographic structure, BCC or FCC. For FCC materials, such as aluminum alloys, the form of equation is given as:

$$\sigma_{THERMAL} = C_2\varepsilon^{1/2}\exp(-C_3T + C_4Tln\dot{\varepsilon}) \quad (3)$$

where C_2, C_3 and C_4 are material constants, ε is the equivalent plastic strain, $\dot{\varepsilon}$ is the strain rate component, and T is the absolute temperature.

The Voce material model [24] was proposed in 1948 to predict the hardening behavior of materials. Voce disagreed with the idea of the indefinite increase of strain hardening adopted in many material models, since experiments typically show leveling off of flow stress at some stress value [26], as supported by Bissot *et al.* [26]. The equation for this model is given by:

$$\sigma_V(\varepsilon_p) = \left[\sigma_{sat} + (\sigma_y - \sigma_{sat})e^{\left(-\varepsilon_p/\varepsilon_r\right)}\right] \quad (4)$$

where σ_{sat} is the saturation stress, σ_y is the yield stress, ε_p and ε_r are effective plastic strain and relaxation strain respectively. The original Voce model was modified by Bardelcik *et al.* to capture strain rate sensitivity of the materials [27] and given as:

$$\sigma_V(\varepsilon_p) = \left[\sigma_{sat} + (\sigma_y - \sigma_{sat})e^{\left(-\varepsilon_p/\varepsilon_r\right)}\right][1 + \dot{\varepsilon}^D] \quad (5)$$

where D is the strain rate parameter. Other strain rate sensitivity models can be used in a multiplicative way along with Voce model [25]. Constitutive models with fewer parameters are preferable to improve the computational time for the numerical analysis.

1.3 Anisotropy in Aluminum Alloys

Due to the extreme deformation during extrusion, aluminum profiles develop a preferred crystallographic orientation in which certain crystallographic planes tend to orient themselves in a preferred manner [28]. Fjeldly *et al.* compared capability of the Hill48, Barlat91, and Barlat94 yield functions in predicting yield behavior of an extruded AA7108 aluminum alloy [28]. Tensile tests in the $0^0, 35^0, 45^0, 55^0$, and 90^0 orientation, with respect to the extrusion direction, showed the presence of a strong anisotropy in flow stress. In a subsequent paper, Fjeldly and Roven [29] performed phenomenological-based modeling of the deformation behaviour of extruded AA7108 and AA7030 aluminum alloys. As in the previous study, tensile and shear experiments revealed the presence of strong directional anisotropy in flow stress and r-values for both aluminum alloys.

Kim [12] studied extruded multi-cell aluminum profiles made of AA6063-T6 and modeled the material as isotropic. Comparison of the numerical results to the experiments highlighted the importance of considering the microstructure of the material in the crush simulations. Achani *et al.* [30] studied the behavior of extruded AA7003 and AA6063 aluminum alloys, in T6 temper condition, under proportional and non-proportional strain paths. Both of the aluminum extrusions showed strong anisotropy in the flow stress and Lankford parameters. Tensile test and through-thickness compression test results were used to calibrate the Yld2000-2d and Yld2004-18p yield criteria developed by Barlat *et al.* [31][32]. The result of the comparison between the two yield criteria showed that the Yld2004-18p function provides superior prediction of the yield surface compared to the Yld2000-2d function; however, the Yld2004-18p yield function requires 18 parameters compared to 8 parameters for Yld2000-2d [30]. In addition, the Yld2000 yield function did provide a very close match to the experimental results. The results of the constitutive fitting to the Yld2000 and Yld2004 are shown in Figure 7, where strain ratios are weighted by w.

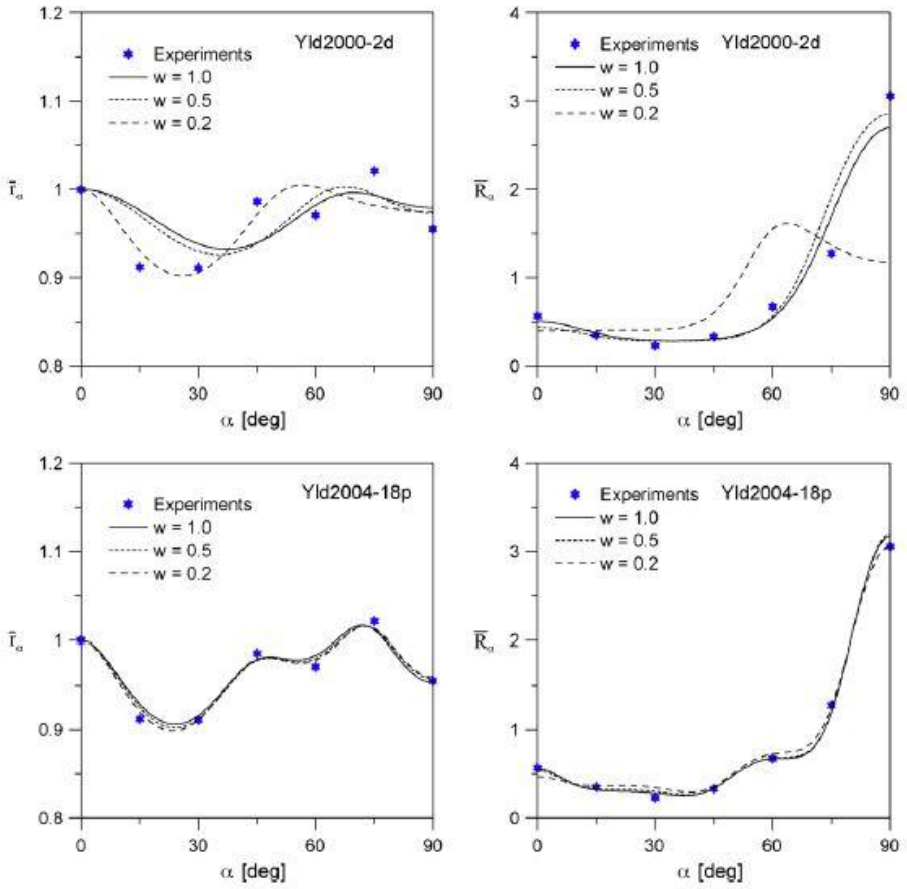

Figure 7 Comparison of experimental and predicted flow stress ratios (left) and r-values (right) to the with respect to the tensile test directions for AA6063-T6 [30]

1.4 Yield Functions

The plasticity and yielding behavior of polycrystalline materials can be described using crystal plasticity based or phenomenological continuum-based models. Crystal plasticity based models use crystallographic texture as the main input and have been successfully implemented into finite element (FE) codes [33][34][35][36]. Although these models were successful in predicting the evolution of anisotropy, their rather high computational cost limits their industrial application. On the other hand, phenomenological models offer much shorter computational time and are easier to implement in FE codes compared to crystal plasticity models. Given these advantages, the use of phenomenological models is more common in industrial application.

There has been a good progress in yield function development for isotropic materials since the introduction of the first yield function by Tresca in 1864. The Tresca criterion is given by the equation below [37].

$$\sigma_1 - \sigma_3 = \sigma_Y, \qquad \sigma_1 \geq \sigma_2 \geq \sigma_3 \tag{6}$$

The Von-Mises quadratic yield criterion was introduced in 1913 and is one of the most widely used yield functions for isotropic materials today.

$$\left[\frac{(\sigma_1 - \sigma_2)^2 - (\sigma_2 - \sigma_3)^2 - (\sigma_3 - \sigma_1)^2}{2}\right]^{1/2} = \sigma_Y \tag{7}$$

where $\sigma_1, \sigma_2, \sigma_3$ are the principal stresses and σ_Y is the yield stress in uniaxial tension [37].

In 1954, Hershey proposed non-quadratic yield criterion that had a better accuracy compared to that of Von-Mises yield criterion. Hosford [37] proposed a generalized non-quadratic isotropic yield criterion and showed that most of the randomly oriented bcc and fcc metals lie between Tresca and Von-Mises yield loci. It was established that this yield function offered better accuracy compared to the classical yield functions proposed by Tresca and Von-Mises and is defined by:

$$(\sigma_1 - \sigma_2)^m - (\sigma_2 - \sigma_3)^m - (\sigma_3 - \sigma_1)^m = 2\bar{\sigma}^m \tag{8}$$

where m is a material parameter and $\bar{\sigma}$ is the effective stress, expressed as a function of effective plastic strain from the uniaxial flow stress. Figure 8 illustrates isotropic yield loci obtained from equation 8 including calculated points for a range of FCC and BCC structure materials. The yield loci were evaluated for n values between 1 and 2.767. For n values greater than 2.676, the yield loci start repeating the shapes of the yield loci at lower n values [37].

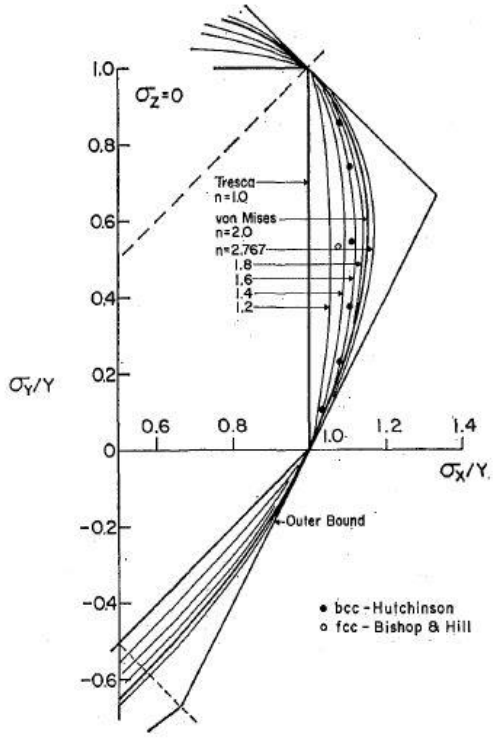

Figure 8 Isotropic yield loci corresponding to equation (8) for n values between 1 and 2.767 [37]

This yield function was modified and presented in generalized form by Barlat and Richmond [38] in 1987 to simulate forming of rolled sheets using a plane stress assumption and showed good accuracy for face-centred cubic (fcc) crystal-structured materials. Bai and Weirzbicki [39] proposed an isotropic yield function with Lode parameter dependence based on the results of experiments and simulations on flat and notched tensile specimens.

The effects of the material anisotropy on yield behaviour have been studied extensively. The first anisotropic yield criterion was presented by Von-Mises in 1928. This yield function was modified and presented by Hill [40] and is referred to commonly as the Hill48 model, given as

$$\sqrt{H(\sigma_1-\sigma_2)^2+F(\sigma_2-\sigma_3)^2+G(\sigma_3-\sigma_1)^2+2N{\tau_{xy}}^2+LN{\tau_{yz}}^2+2M{\tau_{xz}}^2}=\sigma_0 \qquad (9)$$

where H, F, G, N, L, and M are material parameters identified by using yield and shear stresses in three orthogonal axes of anisotropy. Predictions of plastic flow using the Hill48 yield function showed good results for the traditional steels but were somewhat inaccurate for more advanced

alloys and non-ferrous materials. This yield criterion is still popular in the industry for material modeling due to the simplicity of the calibration process.

A large framework of yield functions for anisotropic materials is developed by Barlat *et al.* [38][41][42][43][31][32]. Barlat and Lian [41] proposed an anisotropic yield criterion based on a linear transformation of the stress tensor given in equation (10):

$$\begin{gathered} 2\bar{\sigma}^m = a|K_1 + K_2|^m + a|K_1 - K_2|^m + c|2K_2|^m \\ K_1 = \frac{\sigma_{xx} + h\sigma_{yy}}{2} \\ K_2 = \left(\frac{\sigma_{xx} + h\sigma_{yy}}{2}\right)^2 + p^2{\sigma_{xy}}^2 \end{gathered} \tag{10}$$

where *a*, *c*, *h* and *p* are material constants obtained from experimental tests in different orientations. The linear transformations in this criterion allow users to put different weights on the components of the stress deviator to closely predict the anisotropy level. This yield criterion is able to capture the variation of the Lankford parameters (r-values) or the yield stress variation, but does not offer enough flexibility to capture both anisotropy characteristics. Yld91 and Yld96 were developed to improve the shortcomings of the previous yield functions [42][43].

Barlat *et al.* (2003) proposed the Yld2000-2d [31] yield function for modeling 2-D plane stress anisotropic behavior in sheet metals, with applications focussing on aluminum alloy sheet. Later, this yield criterion was extended to fully three-dimensional stress states and proposed the as Yld2004 yield criterion [32]. The improvements offered by the fully three-dimension formulation come at an expense of a more complicated calibration process, as well as longer computational time.

The Yld2000-2d [31] is based on linear transformations of the stress deviator. The plane stress yield criterion is given as

$$\phi = \phi' + \phi'' = 2\bar{\sigma}^m \tag{11}$$

where exponent a was shown to be connected to the crystal structure and normally taken as equal to 8 for body-centred cubic (bcc) materials and 6 for fcc materials, and ϕ' and ϕ'' are linearly transformed isotropic functions such that

$$\phi' = |X_1' - X_2''|^m$$
$$\phi'' = |2X_2'' + X_1''|^a + |2X_1'' + X_2''|^m \tag{12}$$

where X_i' and X_i'' are principal stresses of linearly transformed Cauchy stress, σ. The transformation is given as

$$X' = L'\sigma \qquad X'' = L''\sigma \tag{13}$$

where L' and L'' are linear transformations tensors defined as

$$L' = \begin{bmatrix} L_{11}' & L_{12}' & 0 \\ L_{21}' & L_{22}' & 0 \\ 0 & 0 & L_{66}' \end{bmatrix} \qquad L'' = \begin{bmatrix} L_{11}'' & L_{12}'' & 0 \\ L_{21}'' & L_{22}'' & 0 \\ 0 & 0 & L_{66}'' \end{bmatrix} \tag{14}$$

The coefficients L_{ii}' and L_{ii}'' are expressed as

$$\begin{bmatrix} L_{11}' \\ L_{12}' \\ L_{21}' \\ L_{22}' \\ L_{66}' \end{bmatrix} = \begin{bmatrix} 2/3 & 0 & 0 \\ -1/3 & 0 & 0 \\ 0 & -1/3 & 0 \\ 0 & 2/3 & 0 \\ 0 & 0 & 1 \end{bmatrix} \begin{bmatrix} \alpha_1 \\ \alpha_2 \\ \alpha_7 \end{bmatrix} \qquad \begin{bmatrix} L_{11}'' \\ L_{12}'' \\ L_{21}'' \\ L_{22}'' \\ L_{66}'' \end{bmatrix} = \frac{1}{9} \begin{bmatrix} -2 & 2 & 8 & -2 & 0 \\ 1 & -4 & -4 & 4 & 0 \\ 4 & -4 & -4 & 1 & 0 \\ -2 & 8 & 2 & -2 & 0 \\ 0 & 0 & 0 & 0 & 9 \end{bmatrix} \begin{bmatrix} \alpha_3 \\ \alpha_4 \\ \alpha_5 \\ \alpha_6 \\ \alpha_8 \end{bmatrix} \tag{15}$$

where the coefficients α_i (i from 1 to 8) are determined by fitting eight parameters obtained from the tensile experiments. These parameters are normally calibrated with the three yield stresses and three Lankford parameters extracted from tensile experiments oriented at $0^o, 45^o$ and 90^o with respect to the extrusion direction. The last two constitutive data points are normally taken as the yield stress and Lankford coefficient obtained from a balanced biaxial tension experiment. The principal values of X' and X'' are defined as (with corresponding prime and double prime indices):

$$X_1 = \frac{1}{2}\left(X_{xx} + X_{yy} + \sqrt{\left(X_{xx} - X_{yy}\right)^2 + 4X_{xy}^2}\right)$$
$$X_2 = \frac{1}{2}\left(X_{xx} + X_{yy} - \sqrt{\left(X_{xx} - X_{yy}\right)^2 + 4X_{xy}^2}\right) \tag{16}$$

1.5 Fracture Modeling

Qiao *et al.* [3] studied the crashworthiness of square aluminum extrusions considering damage evolution. The AA6063-T6 aluminum alloy was modeled using a Von-Mises yield criterion for isotropic materials. The predicted load-displacement curves were higher than that of the experiments. It is worth noting that including damage criteria in the simulation resulted in better predictions, thus it is important to account for fracture in assessing the crashworthiness of energy absorbing structures. This section will outline some of the approaches taken in modeling fracture.

Fracture prediction models are usually categorised into micromechanical, continuum damage mechanics and phenomenological models. In micromechanical and continuum damage based models, where the constitutive plasticity and fracture models are coupled. Phenomenological approach, on the other hand, offers uncoupled modeling approach, where fracture is can be treated as a sudden event when the damage criteria reach prescribed levels. This approach allows utilizing standard metal plasticity models.

In micromechanical damage models the facture is induced by the nucleation, growth and coalescence of voids. The process of void growth and coalescence can be seen in Figure 9.

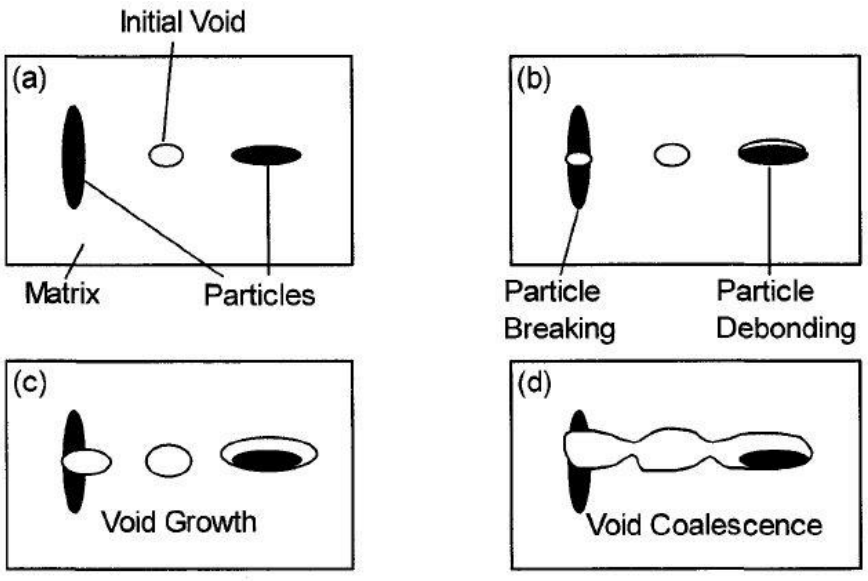

Figure 9 Damage evolution: (a) initial void, (b) void nucleation, (c) void growth, (d) void coalescence [44]

The initial second phase particles as well as inclusions in the material create sites for initial voids as shown in Figure 9 a. Once the material starts to deform, nucleation of new voids occur in addition to growth of existing voids (Figure 9 b and c). At certain level of deformation, the voids will coalescence to cause ductile fracture in the material [44].

Lemaitre introduced a continuum damage model in 1985 [45], where the details of void nucleation, growth and coalescence are ignored. Instead, he proposed to use damage parameter *D*. In this approach, *D* is an inner state variable defined as:

$$D = \frac{S_D}{S} \tag{17}$$

where S and S_D are total area and total area of cavities as shown in Figure 10.

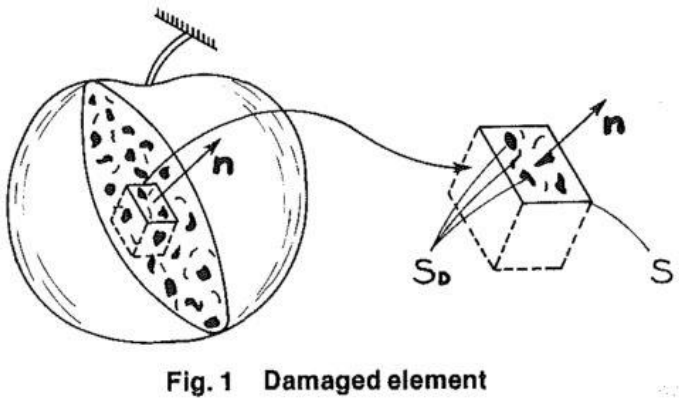

Fig. 1 Damaged element

Figure 10 Damage element [45]

For an undamaged state D is 0, and 1 for element rupture into two parts. From an industry point of view, fracture prediction models should be easily calibrated experimentally and efficiently implemented into FE codes. The micromechanical and continuum damage models still struggle in that sense [46]. Earlier phenomenological fracture models accounted only for the stress triaxiality [47][48].

A common approach is to use the "generalized incremental stress state dependent damage model" (GISSMO) [49][50][16]. This model was developed by Daimler and DYNAmore for modeling ductile failure of materials [51]. The main objective in using the GISSMO model is to

improve numerical simulations involving fracture that involve strain path dependent deformation [52].

The damage parameter in the GISSMO model is defined as

$$D = \left(\frac{\varepsilon_p}{\varepsilon_f}\right)^n \tag{18}$$

where ε_p and ε_f are equivalent plastic strain and equivalent plastic strain at failure respectively and n is an exponent used to introduce non-linearity. The equivalent plastic strain at failure depends on the loading condition, and the above expression is assumed to hold true for proportional loading (the ratio of stress components remain constant). However, real structural components undergo non-proportional loading during progressive buckling. Hence, an incremental damage approach is utilized in order to account for non-proportional loading:

$$dD = \frac{n}{\varepsilon_f(\eta, \xi)} D^{\frac{n-1}{n}} d\varepsilon_p \tag{19}$$

where dD, D, η, ξ and $d\varepsilon_p$represent incremental damage, accumulated damage, stress triaxiality, Lode parameter, and incremental plastic strain, respectively. Failure occurs once the accumulated damage reaches unity [51].

The main input to the GISSMO model is the measured fracture strain as a function of stress triaxiality obtained experimentally. Recent studies by Bai and Wierzbicki have identified the role of the Lode parameter in addition to stress triaxiality in predicting fracture [39]. In their work, they showed that correcting for both, hydrostatic pressure as well as Lode angle results in better load-displacement predictions for AL2024-T351 aluminum alloy, as shown in Figure 11.

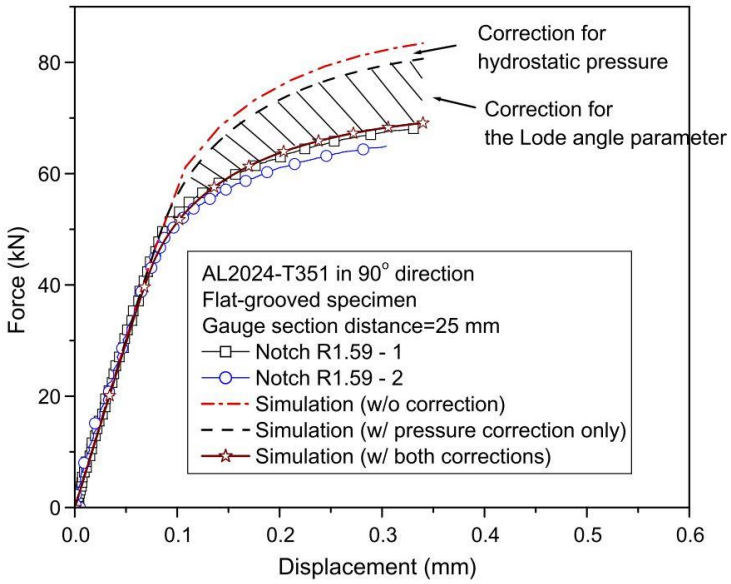

Figure 11 A comparison of force-displacement curves between experimental results and simulation results [39]

Recently, Bai and Wierzbicki [39] have developed a Modified Mohr-Coulomb (MMC) failure criterion by transforming the Mohr-Coulomb model into stress triaxiality, equivalent strain and Lode parameter space. This criterion is simplified to a 2D curve for applications where a plane stress assumption can be employed. The calibration of the MMC failure criterion involves testing material behaviour under a wide range of stress states. These stress states are obtained by testing material in simple shear, hole tension, regular notch and plain strain notch experiments. This approach was adopted for the current thesis using calibration of the MMC fracture model for crash prediction, as described in detail by Nemcko *et al.* [52]. The GISSMO model is calibrated using coupon level test, which involves using finer mesh sizes compared to those of the impact models. As a result, the MMC fracture criterion should be scaled as a function of mesh size.

1.6 Axial Crush Modeling

Modeling of crash experiments usually involves using rigid, non-deformable properties for the impactor [16][53][18]. A common approach is to use 4 node shell elements in modeling crush rails [11][53][50]. The impactor is usually given a constant velocity or initial velocity as well as mass (inertia) [50]. The contact is defined between the parts that are contacting during the axial crush experiment. The reaction forces at the fixed end of the rails are used in obtaining the force-displacement curves [50]. There are a wide variety of material models available in the

standard LS-Dyna library. The constitutive behaviour of the material is modeled using the equations described in earlier sections.

1.7 Summary of previous work and scope of the current work

As is evident from the foregoing literature review, considerable past work has addressed the development of models of the anisotropic constitutive and fracture behaviour of a wide range of automotive alloys. There have also been a number of studies of the impact response of aluminum alloy axial crush members, the focus of the current thesis. However, there remains a need to better assess the predictive capability of current constitutive and fracture models in simulating crush structures and energy absorbing components, particularly for aluminum extrusions.

The objectives of the current work are twofold: (i) to compare the crashworthiness of various multicellular aluminum extrusions and assess the relative improvements gained from changes in profile geometry; and, (ii) assess the anisotropic constitutive and fracture models adopted to predict the crush response of the rails under investigation.

In the current work, the crashworthiness of aluminum rails with two different cross-sections, extruded from aluminum alloy AA6063-T6 is examined. Two profiles are considered, a current commercially-employed cross-section denoted as the "Omega" profile and the other the result of a recent optimization study due to Kohar *et al.* [4] denoted as the "UWR4" profile. Although this alloy has been studied by previous researchers, the compositional range for AA6063 is wide which can result in significant performance variation. For this reason, all of the material characterization experiments (described in detail in Section 2.1) are performed on the as-extruded Omega profile (the UWR4 profile was extruded under similar conditions and compositional specifications).

In this work, the anisotropy, strain rate sensitivity and work-hardening behaviour of the baseline alloy are characterized through tensile, through-thickness compression and simple shear experiments. The strain rate sensitivity of the material is studied by performing tensile experiments at strain rates ranging from 10^{-3} s^{-1} to 10^{3} s^{-1}. The hardening behaviour and strain rate sensitivity of the AA6063-T6 alloy are fit to a generalized Voce model incorporating an exponential logarithmic strain rate term. The anisotropy of the alloy is captured using the

Yld2000-2d [31] yield locus. The fracture behaviour of this alloy was not characterized in the current work, however, characterization experiments on the same extrusion and model fits performed by Nemcko *et al.* [52] have been applied in the current models. The crashworthiness of the extrusions is characterized by performing axial crush experiments under dynamic (7.8 m/s) and quasi-static (0.508 mm/s) conditions. Numerical models of the crush experiments are developed, incorporating the material characterization. Comparison of the predicted and measured crush response is used to evaluate the models.

The balance of this thesis is organized as follows. Chapter 2 presents the experimental methodology comprising constitutive characterization and axial crush testing of the extrusions. Chapter 3 presents the experimental results. The numerical models are described in Chapter 4 which includes fits of the constitutive models to the measured material data due to Butcher [54]. Chapter 5 presents the numerical predictions of the axial crush behaviour of the extrusions including comparison with experiment. Chapter 6 offers conclusions and areas for future work stemming from this research.

2 Experimental Setup

This chapter presents the experimental methods used for the material characterization effort and the axial crush experiments. The thesis focused on a number of AA6063-T6 extrusions that were delivered in several cross-sections (Section 2.1) and were tested under quasi-static and dynamic axial crush conditions, as described in Section 2.3. As part of this research, material characterization experiments were also performed on specimens extracted from one of the extrusion profiles, as detailed in Section 2.2.

2.1 Aluminum Extrusions

This research focused on two AA6063-T6 extrusion profiles, referred to as the "Omega cross-section" and the UWR4 cross-section. The two rail geometries are shown in Figure 12. The Omega cross-section was adopted as a "baseline" profile and is used in a current automotive commercial front end structure. The UWR4 cross-section was developed by Kohar *et al.* [4] utilizing optimization software along with an artificial intelligence algorithm to develop a geometry with improved energy absorption properties. Both sections were extruded using AA6063-T6, a moderate strength aluminum alloy, the chemical composition of which is given in Table 1.

Crush experiments were also performed on a higher strength AA7003-T6 aluminum alloy extruded into the Omega cross-section. The performance of this alloy was used to assess the relative improvement of the new UWR4 cross-section. The main aim of developing the new extrusion profile [4] is to be able to use the relatively less expensive AA6063 material compared to a more expensive 7000-series alloys while maintaining energy absorption performance.

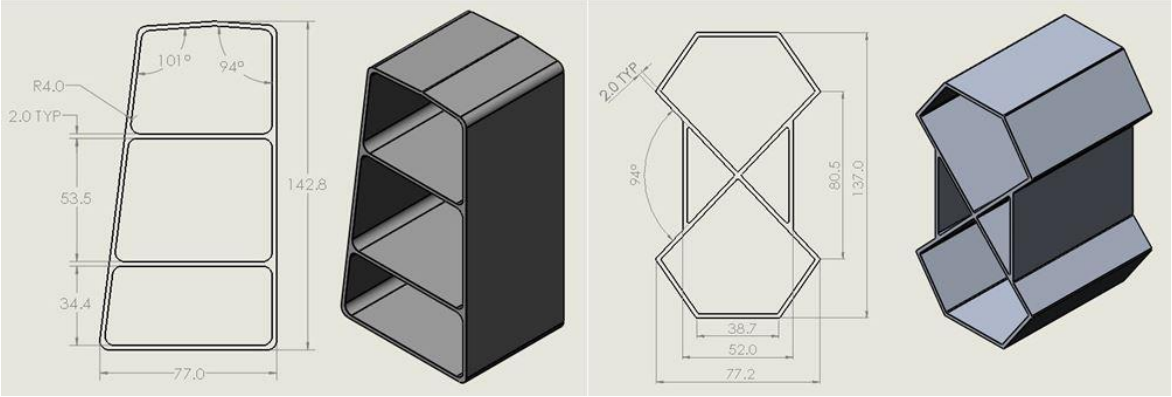

Figure 12 Extruded aluminum profiles (left-Omega, right-UWR4)

The omega rail was extruded using both alloys, and the UWR4 rail was extruded using AA6063 alloy only. The composition of the aluminum alloy is given in the Table 1.

Table 1 Chemical Composition of AA6063 Aluminum Alloy (wt%)

Mg	Mn	Fe	Si	Cu	Ti	Al
0.490	0.029	0.160	0.400	0.010	0.010	Bal

The masses of the aluminum extrusions have slight differences due to the geometric differences of the profiles and density of the alloys. These differences are accounted during the crashworthiness assessment of the rails. Table 2 summarizes the normalized masses of different profile and alloy combinations.

Table 2 Normalized masses of aluminum extrusions

Extrusion profile	Extrusion alloy	Normalized mass [g/mm]	Mass (120 mm rail crush) [g]
Omega	AA6063-T6	2.794	335.2
	AA7003-T6	3.217	386.0
UWR4	AA6063-T6	2.657	318.8

Muhammad *et al.* [55] performed EBSD (Electron Backscatter Diffraction) measurements of the as extruded AA6063 alloy as shown in Figure 13. Extrusion and through thickness

directions are denoted as ED and ND in the image. As shown in the EBSD image, the through thickness texture of the aluminum extrusion is different in the center compared to the outer surface. The average grain size of the alloy is around 63 μm. Pole figures suggest that the texture of the material is Cube followed by weaker Goss texture [55].

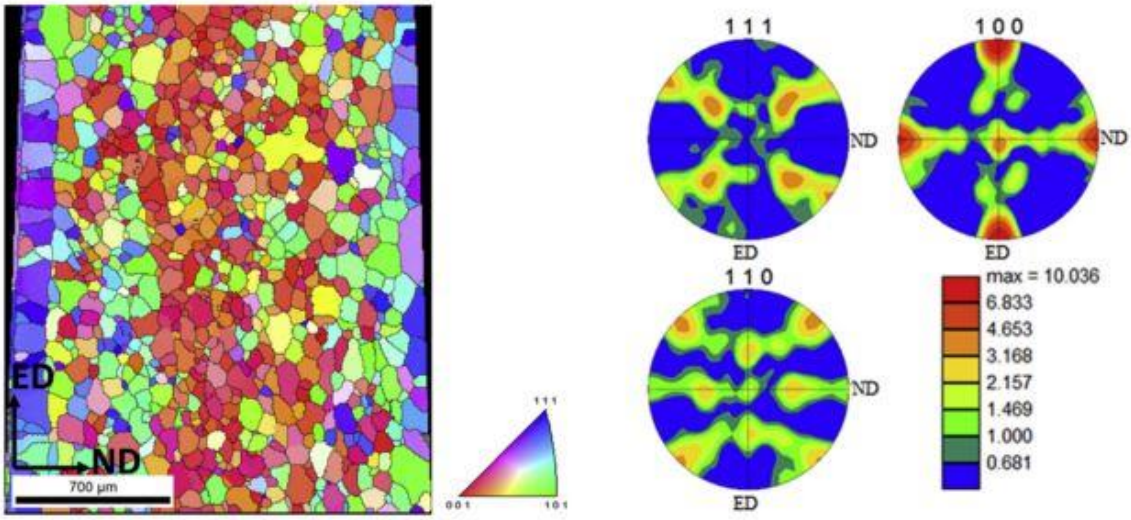

Figure 13 Through thickness texture of as received AA6063 aluminum extrusion [55]

2.2 Material Characterization Experiments

Uniaxial tensile tests were performed on samples taken from the AA6063-T6 extruded Omega cross-section to characterize the hardening response and anisotropy in the as-extruded condition. This data was used to develop a constitutive model of the crush response. A downside to uniaxial tensile tests is the early onset of necking instability which limits the useful range of strain achievable; this shortcoming of the tensile tests was remedied through performing shear experiments which are capable of reaching much higher plastic strains.

2.2.1 Tensile Geometry

All of the tensile samples were machined from the baseline extrusions made of AA6063-T6 alloy. Tensile experiments machined from 11 different walls of the baseline profile showed little variation in mechanical properties, except for the internal webs [4]. To reduce the variation

in mechanical response of the material, all of the specimens used in experiments were machined from the same wall as shown in Figure 14.

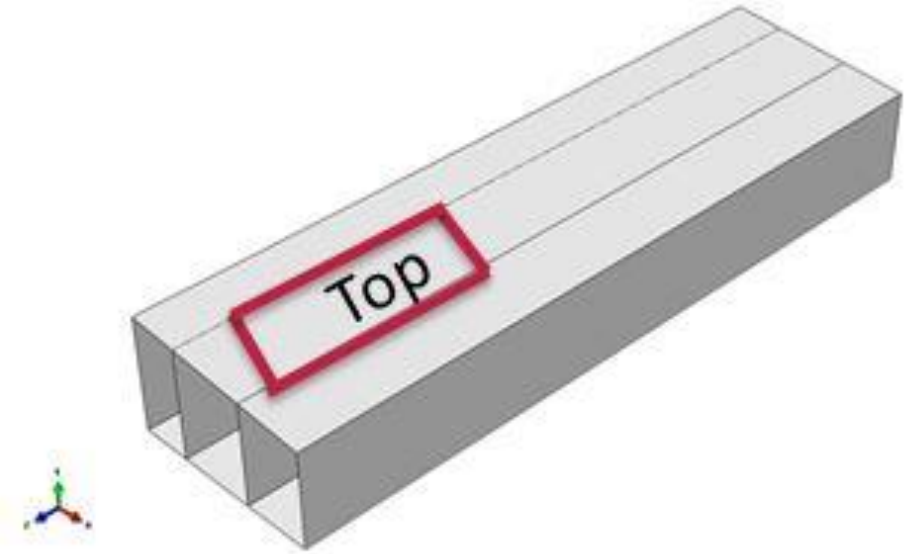

Figure 14 Samples for experiments from top wall - baseline extrusion AA6063-T6

The mechanical properties of AA6063-T6 were obtained using the Japanese Industrial Standard tensile geometry (JIS) shown in Figure 15a. Due to geometrical constraints of the aluminum extrusions, the JIS samples were machined only in the extrusion direction, and scaled down to 50% of the original sample dimensions (mini – JIS or MJIS) to obtain the parameters in other directions. The dimensions of the MJIS sample are shown in Figure 15b. The engineering stress-strain curves of the MJIS tensile experiments were validated against those of the JIS samples in the extrusion direction. The yield stress ratios and Lankford parameters in the $0^o, 45^o,$ and 90^o orientations were obtained from MJIS samples at the strain rate of 0.001 s^{-1}.

The strain rate sensitivity analysis of the aluminum alloy in the 0.001 s^{-1} – 1000 s^{-1} strain rate regime was performed using miniature dog-bone (Mini-DB) specimens. The miniature dog-bone specimen geometry is shown in Figure 15c and was developed by Smerd *et al*. [19] for aluminum sheet metal. It was established [19] that the stress versus strain curves of the miniature dog-bone specimen matched those of the conventional ASTM: E8M specimen for aluminum alloys.

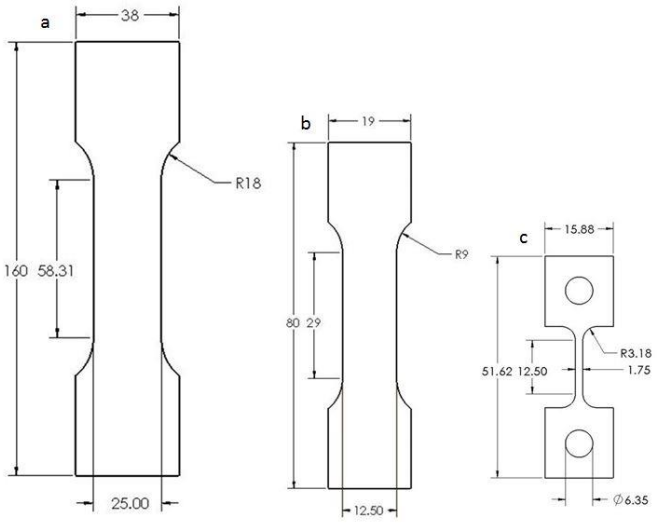

Figure 15 Tensile specimen geometries (a) JIS; (b) MJIS; (c) Mini-DB

The stress-strain responses of the different tensile geometries show good agreement up to uniform tensile strength as shown in Figure 16.

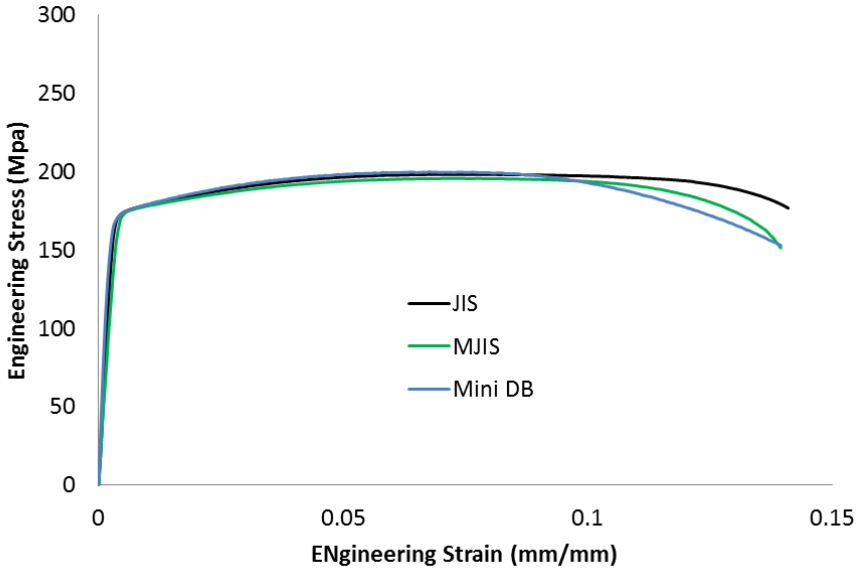

Figure 16 Tensile sample geometry comparison

2.2.2 Low Strain rates – MTS apparatus

Tensile experiments in the strain rate regime of 0.001 s^{-1}-0.1 s^{-1} were conducted on the MTS criterion Model 45 testing frame with 100 kN force capacity. A 10 kN load cell was used

in order to capture the load data from the experiment. The setup of the tensile experiments performed on the MTS tensile frame is shown in Figure 17.

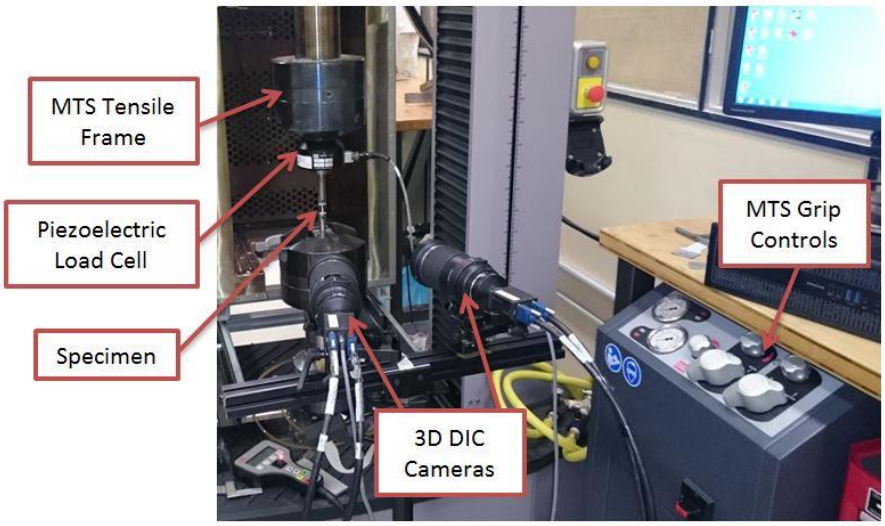

Figure 17 Tensile experiment setup on MTS tensile frame

2.2.3 Intermediate Strain Rates - Hydraulic Intermediate Strain Rate Apparatus

The intermediate strain rate tensile experiments were performed using the hydraulic intermediate strain rate (HISR) machine developed at the University of Waterloo [27]. The schematic of the HISR apparatus is shown in Figure 18. The HISR apparatus deploys a servo-valve to achieve a maximum of 1500 mm/s cross-head velocity and total displacement of 101.6 mm. The specimen is mounted between the upper and lower grips. The load exerted to the tensile specimen during experiment is measured using a KISTLER piezoelectric load cell attached directly to the upper grip. The engagement sleeve accelerates to a constant velocity and drives the engagement piston to apply uniaxial tension to the mounted specimen. A damper is used to reduce the ringing upon metal to metal contact between the sleeve and piston. Use of rubber O-ring imposes an additional ramp up time before the piston achieves a constant velocity, but the constant velocity is achieved at a relatively low strain level and observed to have small effects on the material response [27]. Cross-head velocities of 12.5 mm/s, 125 mm/s and 1250 mm/s were used to achieve strain rates of 1 s^{-1}, 10 s^{-1} and 100 s^{-1} respectively.

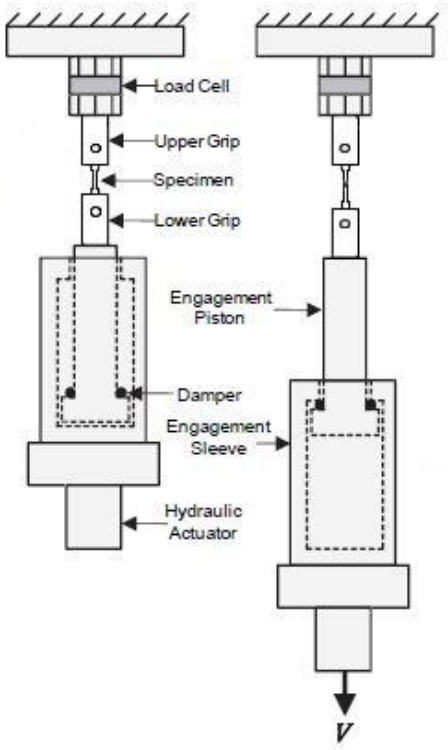

Figure 18 HISR apparatus schematic [27]

The load data from the piezoelectric load cell is acquired by the National Instrument data acquisition module connected to a personal computer. As in the low strain rate experiments, a DIC system was used to measure the strain distribution on the sample surface.

2.2.4 High strain rate tensile testing

The highest strain rate testing (10^3 s^{-1}) of the AA6063-T6 aluminum alloy was performed using a tensile split Hopkinson bar apparatus (TSHB) by Taamjeed Rahmaan, a PhD candidate at the University of Waterloo. The experimental setup for the TSHB apparatus is explained in the work by Rahmaan *et al.* [56][21].

2.3 Shear experiments

Shear experiments are fundamental for understanding the plastic behaviour of metals. Contrary to uniaxial tensile and compression tests, shear experiments can take material deformation to large strains without plastic instabilities [57]. Peirs *et al.* have developed the so-called "mini-shear" specimen that can be tested by means of a conventional tensile testing machine. The mini-shear specimen geometry is shown in Figure 19. Abedini *et al.* [58],

Abedini *et al.* [59] and Abedini *et al.* [60] used mini-shear specimens to characterize the fracture strains under shear loading conditions for magnesium ZEK100, steel DP600 and DP780 alloys and have demonstrated the advantages of the specimen geometry for constitutive plastic and fracture characterization of these various materials.

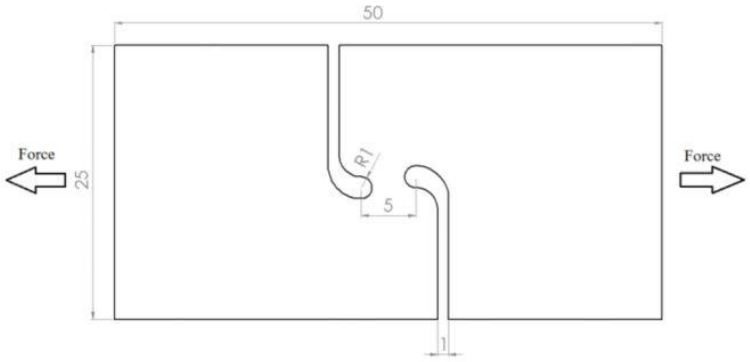

Figure 19 Mini-Shear Specimen Geometry (All dimensions are in millimeters) [57][58]

The mini-shear tests were performed using the MTS criterion 45 tensile testing apparatus described above. The setup for the mini-shear tests was similar to that of the uniaxial tensile experiments. The strain field was measured using DIC techniques. The shear experiments were performed with the loading axis aligned in the extrusion and diagonal directions. Due to orthotropic symmetry in extruded aluminum alloys [1], the shear experiments in the transverse direction were deemed redundant. The results of the shear experiments were used to calibrate the hardening behaviour of the alloy at large strains. Figure 20 illustrates the shear experiment mounted on the MTS tensile frame.

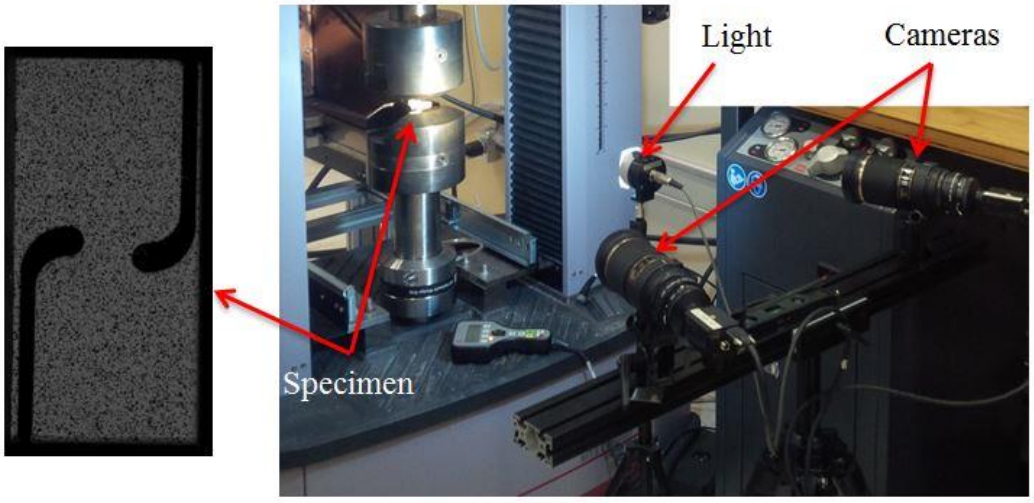

Figure 20 Shear experiment setup on MTS apparatus

2.4 Through-Thickness Compression Experiment

The dimensional constraints of the extrusions limit the possibility of using conventional equal-biaxial tension tests for yield function calibration. For this reason, the equal-biaxial tension test was replaced with through-thickness compression tests (TTCT). The use of compression tests is justified by Barlat *et al.* [31][61]. Through-thickness compression tests were performed using an Instron model 1331 servo-hydraulic testing machine. The setup for this experiment is shown in Figure 21. The specimen preparation and experimental setup were similar to those described by Steglich *et al.* [62] and Kurukuri *et al.* [63][64].

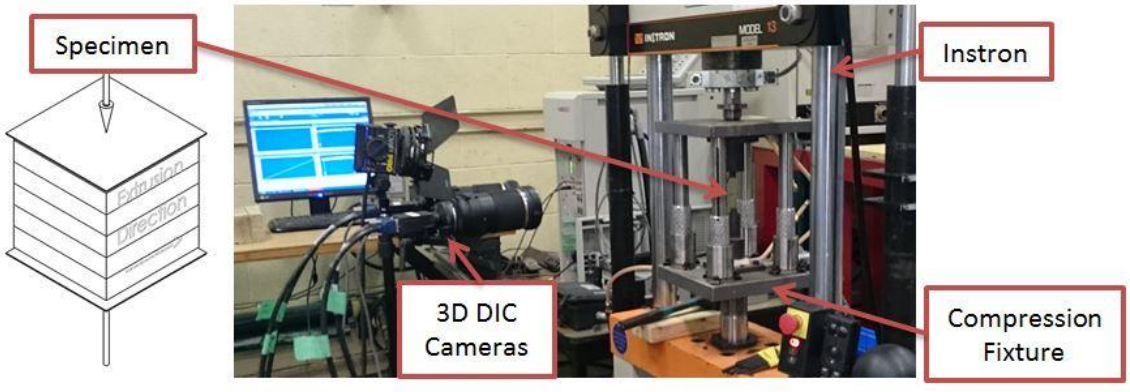

Figure 21 Through-thickness compression test setup

Cubic specimens for the compression tests were prepared by gluing five layers of aluminum extrusions using J-B Weld® adhesive [62]. Each layer was machined along the extrusion and transverse directions. The surfaces of each single layer were roughened using sand paper to improve the performance of the adhesive. The thickness of overall cube specimen consisted of five aluminum layers and adhesive between each layer, which resulted in a thickness slightly above 9.3 mm, with each layer of aluminum being 1.85 mm. All the surfaces of the cubic specimen were polished after the adhesive had fully cured. To reduce friction between the specimen and the compressing platens, the platen surfaces were mirror polished and lubricated using Teflon spray.

The specimens for the compression tests were prepared by stacking square aluminum cut-outs attached to each other using adhesive. All the aluminum cut-outs were aligned to have same orientation within the sample (i.e. the extrusion direction was oriented in the same direction for each layer). Once the adhesive bonding the layers fully cured, imperfections and extra adhesive were removed by polishing.

2.5 Digital Image Correlation

A digital image correlation (DIC) system was used to measure strain fields in the samples during the uniaxial tension, simple shear, and through-thickness compression experiments. The DIC system offers the ability to measure whole-field true strains compared to conventional extensometers [65] which are limited to specific gauge lengths and orientations. The principles for 2D and stereographic DIC strain measurements are explained in detail in [66].

In the DIC method, the samples are painted using white paint as a background, and black foreground paint to create a random speckle pattern on the sample surface. During the experiment, the motion of the speckles is tracked using either two stereo cameras in case of stereographic DIC or one camera in the case of 2D DIC. The image is divided into small areas, so-called subsets, and the intensity of the pixels in each subset is calculated. The deformation in the specimen is calculated by comparing the consecutive images from the test [25].

The accuracy of the DIC calculations depend on the quality of the speckle pattern applied to the specimen. A typical speckle pattern is shown in Figure 22.

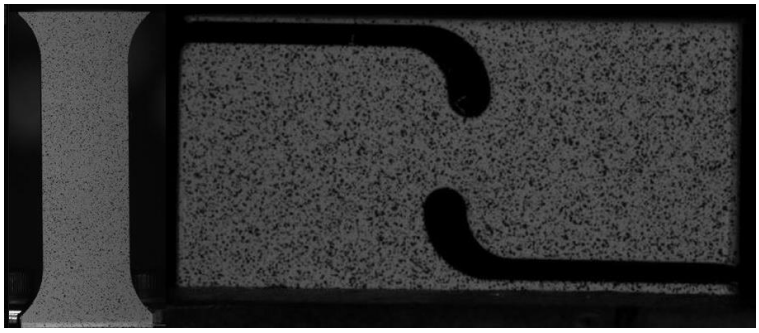

Figure 22 Typical Speckle Patterns (not to scale)

In this work, the strain fields in the tensile experiments performed at strain rates of 10^{-3} s^{-1}, 10^{-2} s^{-1}, and 10^{-1} s^{-1}, the through-thickness compression tests and the simple shear experiments were measured using a stereographic DIC configuration. The longitudinal tensile experiments at 1 s^{-1}, 10 s^{-1}, and 100 s^{-1} were performed using 2D DIC measurements. The experimental matrix used for material characterization is listed in

Table 3. The images acquired during the experiments were processed using the Correlated Solutions Vic3D and Vic2D software for images obtained from stereographic DIC and 2D DIC respectively.

The DIC calculations are dependent on the subset size, step size, and filter size used in the analysis of the acquired images. The dependence of these parameters on the Virtual Strain Gage Length (VSGL) is described in detail in the work done by Rahmaan *et al*. [67].

The VSGL values reported in this work are calculated as shown in equation 20 :

$$VSGL = Resolution\ of\ the\ area\ of\ interest * Step\ Size * Filter\ Size \quad (20)$$

Table 3 Material characterization tests parameters

Experiment	Direction [deg] (With respect to extrusion)	Strain Rate [s^{-1}]	Number of Repeats	Frame Rate [fps]	Resolution	VSGL [mm]
Tension	0^o	0.001	3	4	2445x2045	~0.9
		0.01	3	25	2047x2047	
		0.1	3	150	2047x2047	
		1	4	1500	256x840	
		10	4	15000	256x840	
		1000	8	N/A	N/A	
	45^o	0.001	3	4	2445x2045	
		0.01	3	25	2047x2047	
		0.1	3	150	2047x2047	
		1	4	1500	256x840	
		10	4	15000	256x840	
	90^o	0.001	3	4	2445x2045	
		0.01	3	25	2047x2047	
		0.1	3	150	2047x2047	
		1	4	1500	256x840	
		10	4	15000	256x840	
Through-Thickness Compression	Normal to the plane	0.003	4	4	2047x2047	~0.55
Shear	11^o	0.03	3	7	2447x2047	~0.86
	56^o	0.03	3	7	2447x2047	

2.6 Crush Experiments

2.6.1 Dynamic Crush Setup

The dynamic axial crush experiments were performed using an instrumented 169 kJ impact crash sled. The sled is equipped with two accelerometers to measure the deceleration during the impact which is integrated to determine transient velocity and displacement versus time. Figure 23 is a schematic of the dynamic axial crush experiment, while Figure 24 is a photograph showing the test specimen and key elements of the experimental setup.

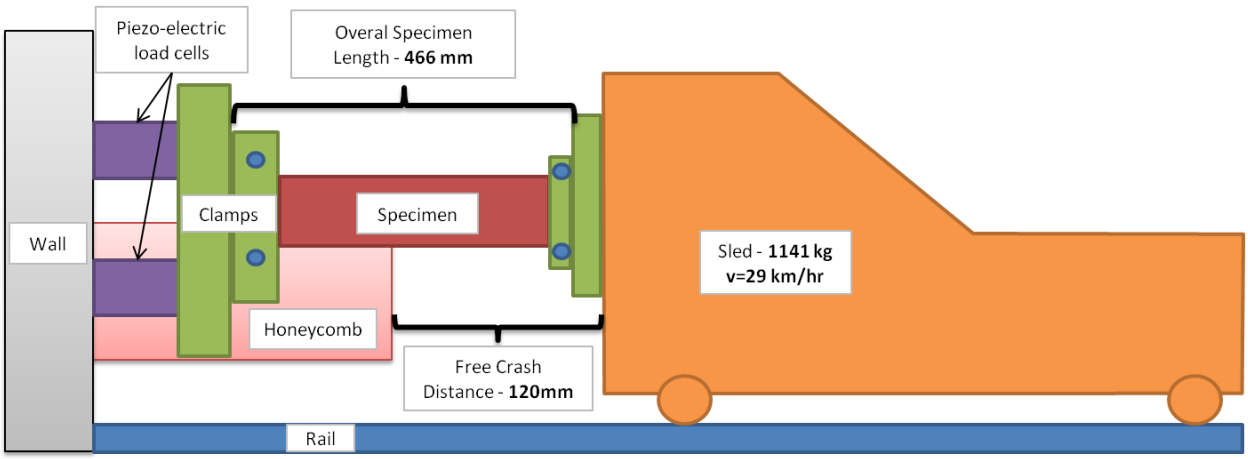

Figure 23 Schematic of specimen mounted for impact test

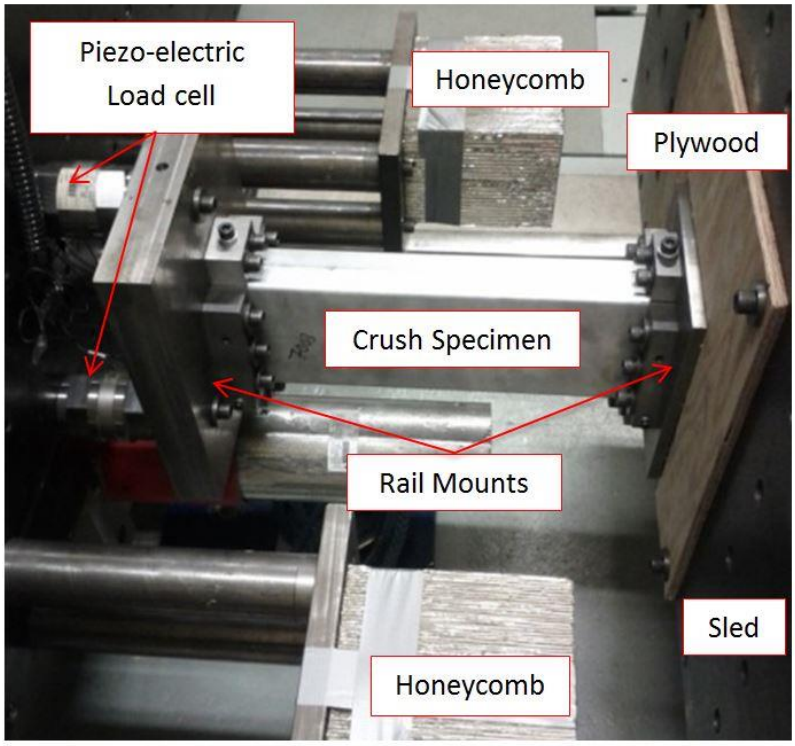

Figure 24 Specimen mounted on wall

Aluminum extrusions (rails) were cut to the test length of 466 mm and fixed horizontally between the rail mounts as shown in Figure 24. 12.5 mm (½" thick) veneer core plywood was placed at the impact face of the sled in order to reduce the ringing in the load cells that would result from metal-to-metal contact.

The combined mass of the sled and sled-mounted vertical reaction wall was 855 kg and an additional 286 kg was added in the form of ballast weight and hardware fixing the ballast; hence, the total impact mass was 1141 kg. The impact velocity of the sled was 28.8 km/s for all of the dynamic tests.

The rails were mounted 220 mm above the base of the sled. The mounts were designed using clamps fit to the outer profile of the rails as well as internal bosses to prevent the rail walls from buckling. The plates between the rails and load cells were 50 mm thick and the bosses at the wall mounts were 38 mm thick. The plates on the other end of the rails (the impacted end) were 12.5 mm thick with boss thicknesses of 19 mm. This arrangement results in 409 mm of unclamped rail length. The clamping screws for the bosses on the wall end of the rails were located 19 mm from the wall end of the rail and 10 mm from the impacted end of the rails.

The bosses were mounted to the back plate using M12x1.75 screws. The profile of the rail was clamped by internal and external bosses using M10x1.5 and M6x1.0 screws. The CAD model of the wall end clamp assembly for both cross-sections is shown in Figure 25. The screw holes on the rails were drilled to align with the corresponding locations of the mounting holes on the bosses and clamps. All of the fixtures were machined from low carbon steel.

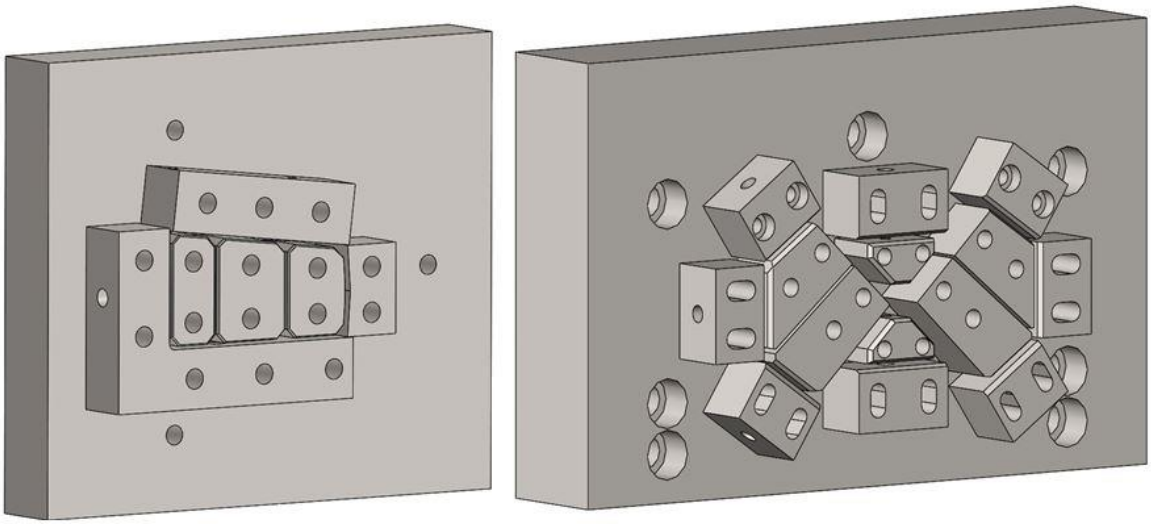

Figure 25 Omega (left) and UWR4 (right) bosses for rail mounts

The kinetic energy of the sled prior to impact exceeds the energy that can be absorbed by the extruded aluminum rails. This excess energy and large sled mass serves to reduce the velocity variation during crush of the rail, but does require an "arrestor system" to absorb the excess energy and stop the sled. For these experiments, the arrestor is composed of two Plascore 5056 aluminum honeycomb blocks (shown in Figure 24), with 3.69 Mpa (535 psi) compressive strength, used to arrest the excess energy and bring the sled to a full stop in a safe manner. For safety reasons, the honeycomb cores were sized to be able to absorb the entire kinetic energy generated from the sled. In order to balance the forces applied on the sled, two honeycomb cores were used, one on each side of the rails. The width, length and depth of the honeycomb cores were 150x200x200 mm respectively. These cores were pre-crushed to approximately to198 mm in order to reduce the force required to initiate folding. The aluminum honeycomb cores were mounted on standoffs which left 120 mm of rail for "free crush" before the sled face impacts the honeycomb arrestors.

Piezo-electric load cells were used to capture the forces exerted on the specimen by the sled. The load cells used in the experiments had 120 kN capacity. Three Kistler Quartz Force Link (model #9371B) load cells were used to measure the crush load for the Omega rails. The UWR4 rails had a higher crush load such that four load cells were used. These load cells captured the force exerted on the rail by the sled. The total force applied by the sled was calculated by summing the forces from the individual load cells. Load cells were arranged in triangular and rectangular patterns for the Omega and UWR4 cross-sections, respectively. The forces exerted by the sled were sampled at the rate of 10,000 data points per second. All of the data acquisition systems were triggered using a laser trigger mounted on the sled rail as shown in Figure 26, activated moments before the sled impacts the specimen. Data from the load cells, accelerometers and cameras were recorded using the DTS Slice DAQ system.

The axial movement of the sled was achieved by running the sled on the rails. Compressed air drives a piston which pulls a tow rope attached to the sled. The sled has two accelerometers located under the sled, one on the left and one on the right side. The absence of rotational (yaw) acceleration was checked by comparing the readings from both accelerometers. The velocity of the sled is calculated by the trigger system. The trigger system contains a 303 mm gate (shown in Figure 26), which triggers the laser switch. The time required for the sled to travel 303 mm is

measured, and the sled velocity is calculated. The displacement of the sled was calculated by integrating the recorded acceleration twice with respect to time. The data was sampled at the same rate as the load cells on the wall.

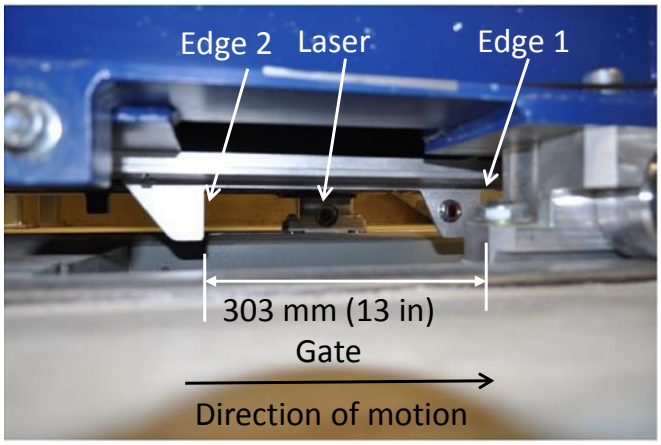

Figure 26 Trigger system

The dynamic experiments were recorded using two high-speed Photron SA4 and SA5 digital cameras operated at 5000 frames per second. One camera recorded the top view of the specimen (SA4), while the other (SA5) recorded the side view of the specimen. The side and top views from the cameras can be seen from Figure 27.

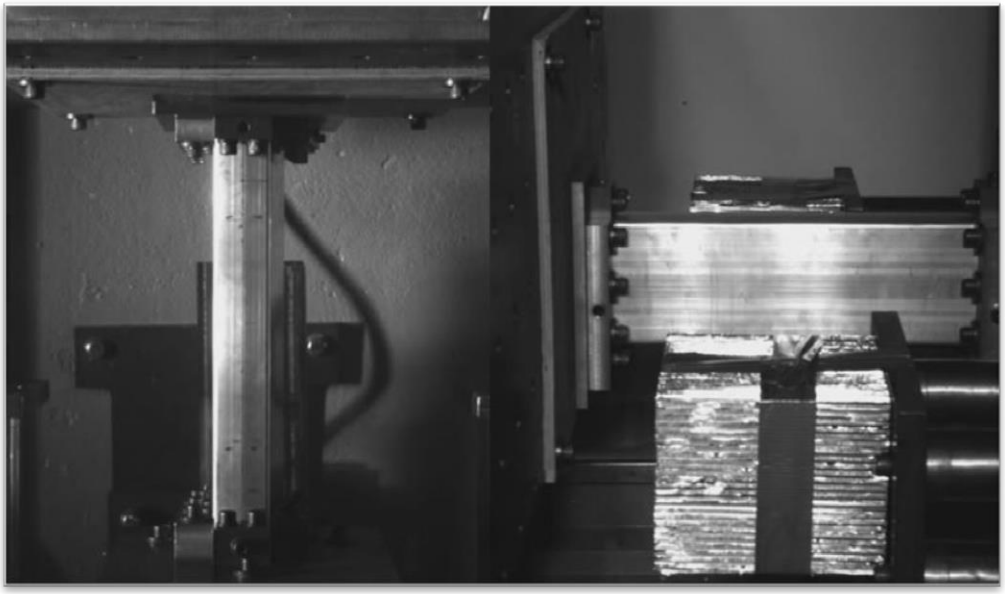

Figure 27 Top (left) and side (right) views of the specimen from Photron cameras

2.6.2 Quasi-Static Crush Setup

Figure 28 illustrates the experimental setup for the quasi-static crush tests. The specimen was mounted on the horizontal platen of the test frame using the same mounting fixtures used for the dynamic crush experiments. The mounts were clamped down to the platen using T-slot clamps. The hydraulic actuator with 500 kN load capacity, was operated under closed-loop servo-control, with a constant velocity of 0.508 mm/sec which corresponds to a nominal strain rate of 0.001 s^{-1}. The duration of each quasi-static experiment was 5 minutes which resulted in 152 mm of crush. The force-displacement data was sampled at 4 Hz using a DAQ board within a PC controlled using a custom Labview program. The hydraulic actuator is controlled using an MTS Flex Test SE controller. The quasi-static experiments were recorded using a Nikon digital camera.

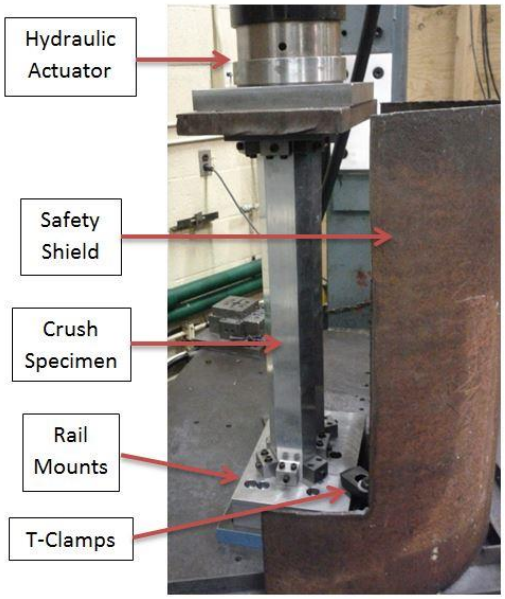

Figure 28 Quasi-Static Crush Setup

Table 4 summarizes the test matrix for axial crush experiments including the crush mode, test designation and extrusion alloys.

Table 4 Axial crush experiment matrix

Crush mode	Test	Material
Dynamic [7.8 m/s]	Omega_29_4	AA6063-T6
	Omega_29_5	
	Omega_29_6	
	UWR4_29_4	
	UWR4_29_5	
	UWR4_29_6	
	Omega_7003_29_1	AA7003-T6
	Omega_7003_29_2	
	Omega_7003_29_3	
Quasi-Static [0.508 mm/s]	Omega_QS_3	AA6063-T6
	Omega_QS_4	
	Omega_QS_5	
	UWR4_QS_2	
	UWR4_QS_3	
	UWR4_QS_4	
	Omega_7003_QS_1	AA7003-T6
	Omega_7003_QS_2	

3 Experimental Results

This chapter presents the results of the material characterization experiments, followed by the static and dynamic axial crush experiments.

3.1 Uniaxial Tensile experiments

The tensile load-displacement data obtained from the uniaxial tensile experiments was converted to true stress-strain data using the formulae shown below:

$$\sigma_{true} = \sigma_{eng}(1 + \varepsilon_{eng})$$
$$\varepsilon_{true} = \ln(1 + \varepsilon_{eng}) \quad (21)$$

Where $\sigma_{true}, \sigma_{eng}, \varepsilon_{eng}$ and ε_{true} are true stress, engineering stress, engineering strain and true strain respectively. Note that equation (21) is valid strictly for conditions prior to the onset of necking at the material ultimate tensile strength (UTS). The true strain is further converted to effective plastic strain as shown below:

$$\varepsilon_{pl} = \varepsilon_{true} - \left({}^{\sigma_{true}}/_{E}\right) \quad (22)$$

Where ε_{pl} and E are effective plastic strain and Young's modulus. As was mentioned in Section 2.2.1, the mechanical parameters of AA6063-T6 alloy were obtained using Mini JIS (MJIS) samples taken from the baseline Omega rail. It was shown that all three tensile geometries used in this study have a good agreement up to UTS **(**see Figure 16**)**.

Figure 29-Figure 31 illustrate the tensile test results for the AA6063-T6 aluminum alloy in the ED, DD and TD. The tensile experimental results revealed a variability of +/-5 MPa between repeats. A similar level of scatter was reported by Lademo *et al.* [1], Tryland *et al.* [68] and Clausen *et al.* [69] for tests on 6000-series aluminum extrusions. The scatter in the engineering stress-strain response is similar in all directions.

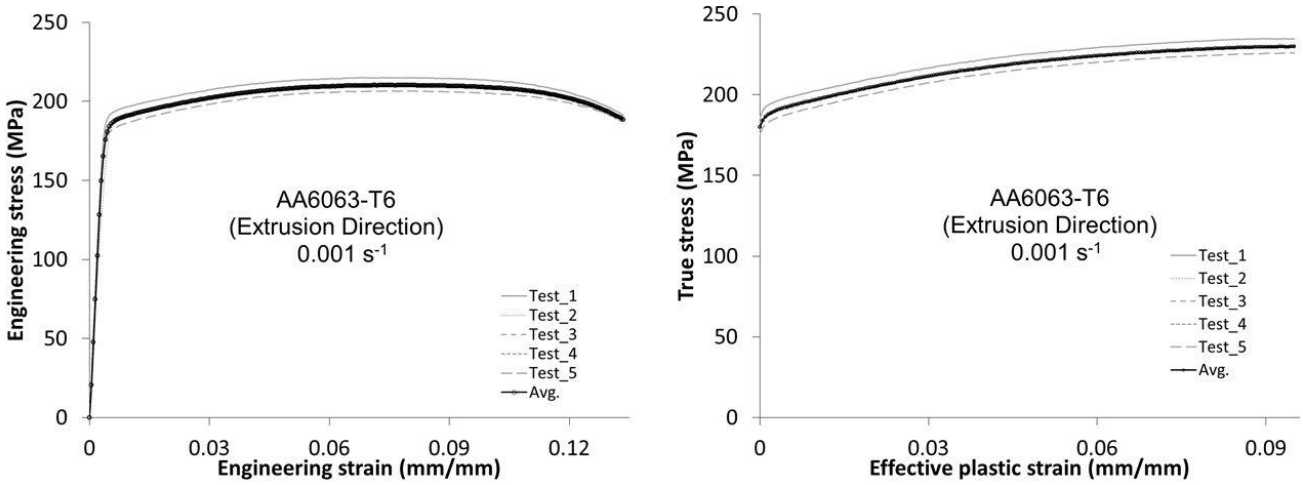

Figure 29 AA6063-T6 tensile test results using MJIS samples (Extrusion Direction)

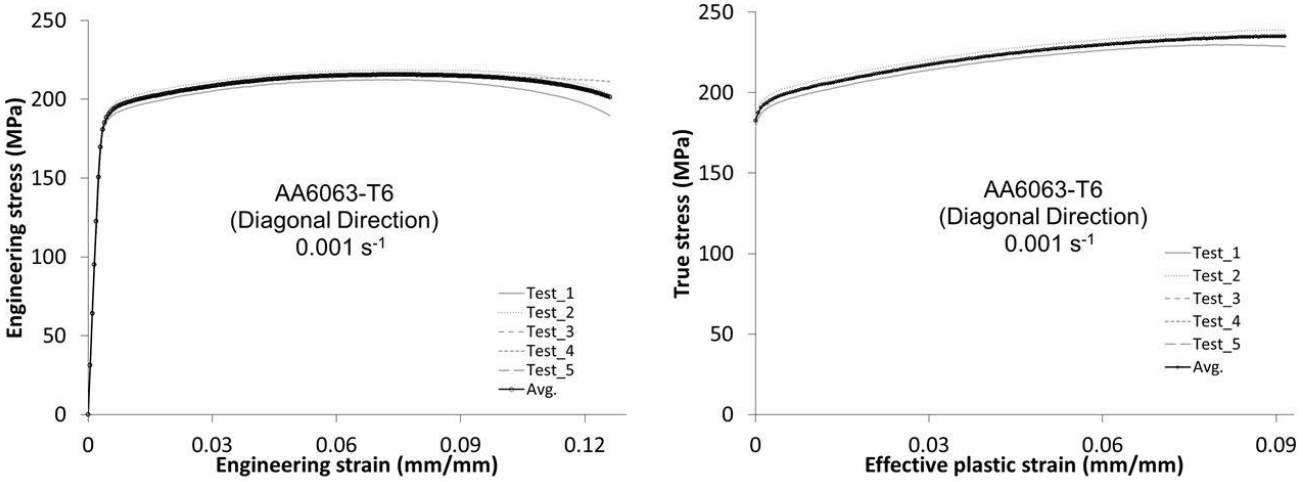

Figure 30 AA6063-T6 tensile test results using MJIS samples (Diagonal Direction)

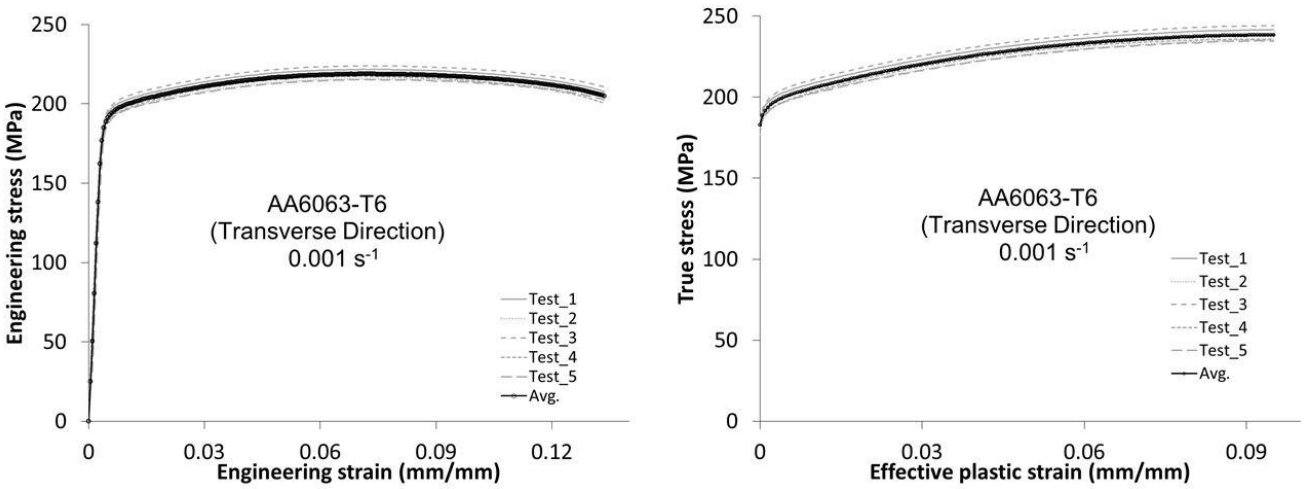

Figure 31 AA6063-T6 tensile test results using MJIS samples (Transverse Direction)

The DIC analysis of the tensile specimens showed a uniform distribution of the strain field in the gauge region of the specimens prior to necking. Figure 32-Figure 34 illustrate contours of the Hencky strain within the gage region of the tensile specimens at various nominal strains during deformation. Hencky strain, also known as natural or logarithmic strain, is an appropriate measure of large deformation under condition where the principal direction of strain undergo rotation [70]. Accounting for rotation of principle strain rotation is important in shear experiments, during which the material undergoes large deformation and rotation. Hencky strain is expressed as:

$$h = ln\, U \tag{23}$$

where h represents the Hencky strain. U is a right stretch component of the deformation gradient F. Deformation gradient can be decomposed to pure rotation and pure stretch tensors through polar decomposition theorem as:

$$F = RU \tag{24}$$

where R is rotation tensor.

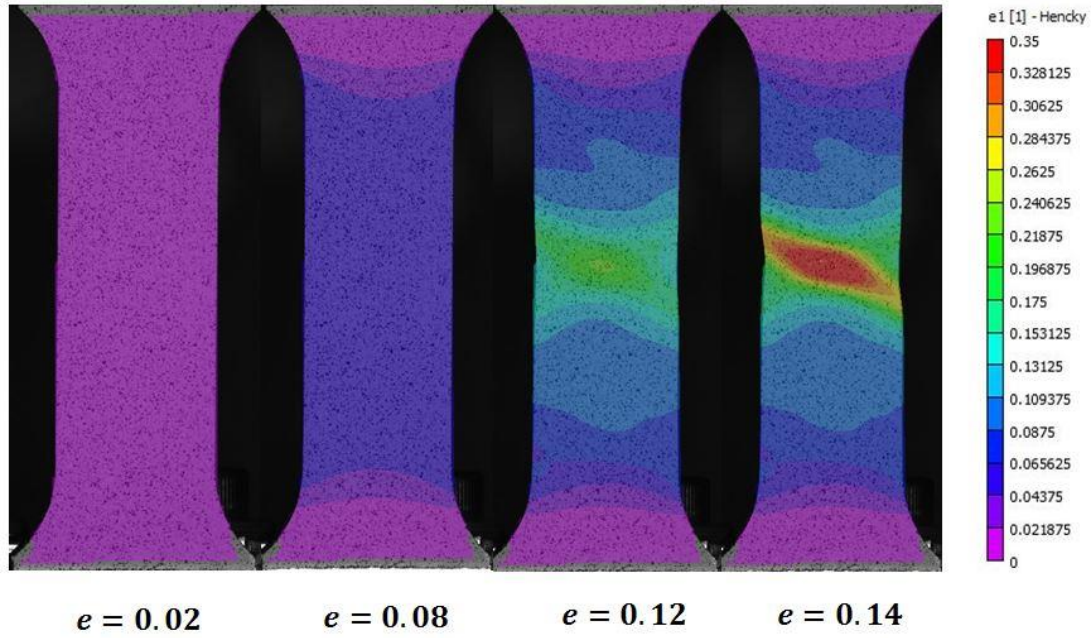

Figure 32 DIC analysis images of tensile tests performed using MJIS samples (ED). Contours are of Hencky strain.

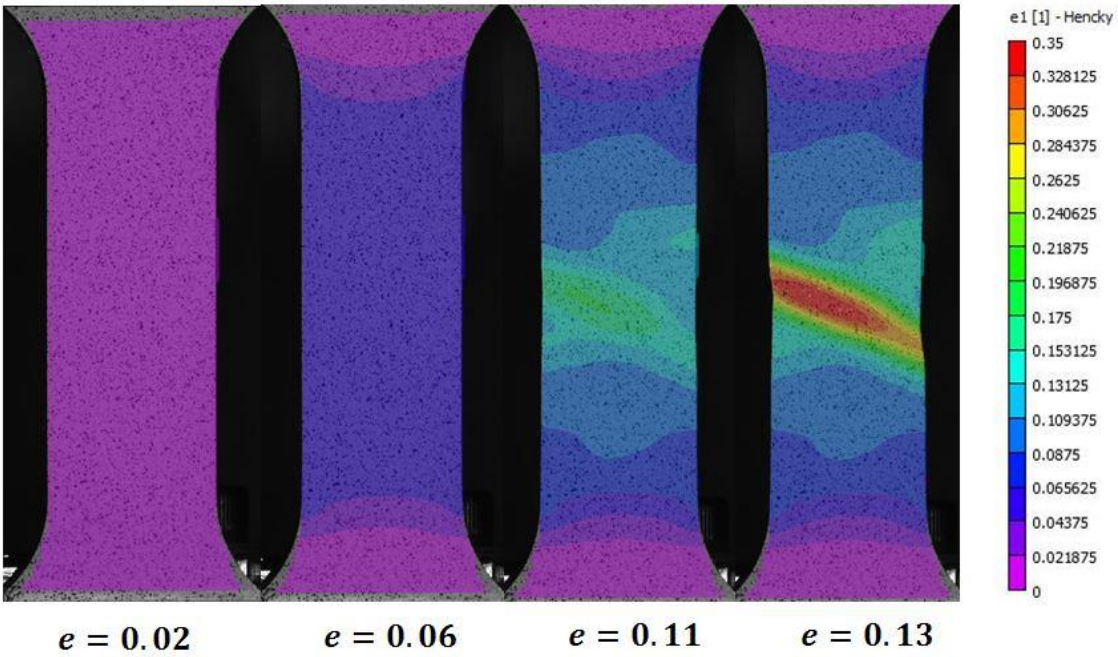

Figure 33 DIC analysis images of tensile tests performed using MJIS samples (DD). Contours are of Hencky strain.

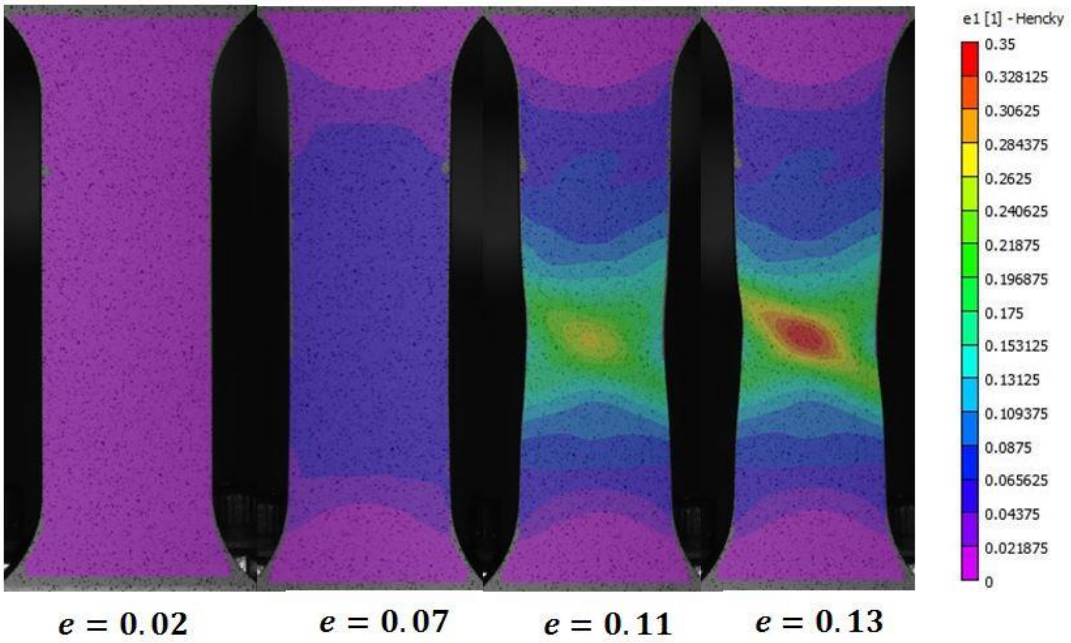

Figure 34 DIC analysis images of tensile tests performed using MJIS samples (TD). Contours are of Hencky strain.

The strain measurements are obtained from the DIC software by placing three virtual extensometers with 25mm strain gage length along the specimen image and averaging the strain values. In addition, the r-values are measured from the uniaxial tension experiments by calculating the ratio of the plastic strain in the width and thickness directions of the specimen. The Lankford coefficients can be calculated as follows:

$$r_\theta = \frac{\varepsilon_\theta^w}{\varepsilon_\theta^t} \tag{25}$$

Where r_θ, ε_θ^w and ε_θ^t denote the Lankford parameter and plastic strains in the width and thickness directions, respectively, for tensile tests Oriented at various angles (theta) with respect to the extrusion direction.

The mechanical properties of tensile experiments are summarized in Table 5.

Table 5 AA6063-T6 tensile experiment results

Tensile Loading Direction	σ_{yld} [MPa]	Average (σ_{yld})	Std. Dev (σ_{yld})	r-value	Average (r-value)	Std. Dev (r-value)
0^o	164.4	166.4	6.5	0.36	0.37	0.01
	159.7			0.36		
	175.2			0.39		
	166.2			0.37		
45^o	181.6	183.3	2.0	0.44	0.43	0.005
	185.6			0.43		
	181.7			0.43		
	184.4			0.44		
90^o	177.8	180.1	6.6	0.83	0.92	0.07
	185.8			0.88		
	171.9			0.97		
	185.1			0.98		

3.2 Compression experiments

Through-thickness compression tests were performed on an Instron model 1331 servo-hydraulic testing machine. The elastic region of the engineering stress-strain response is influenced by the seating of the sample and adhesive bonding [30]. Consequently, the elastic slopes observed in these compression tests are typically different from those obtained in uniaxial tension tests. The results of the compression tests are shown in Figure 35.

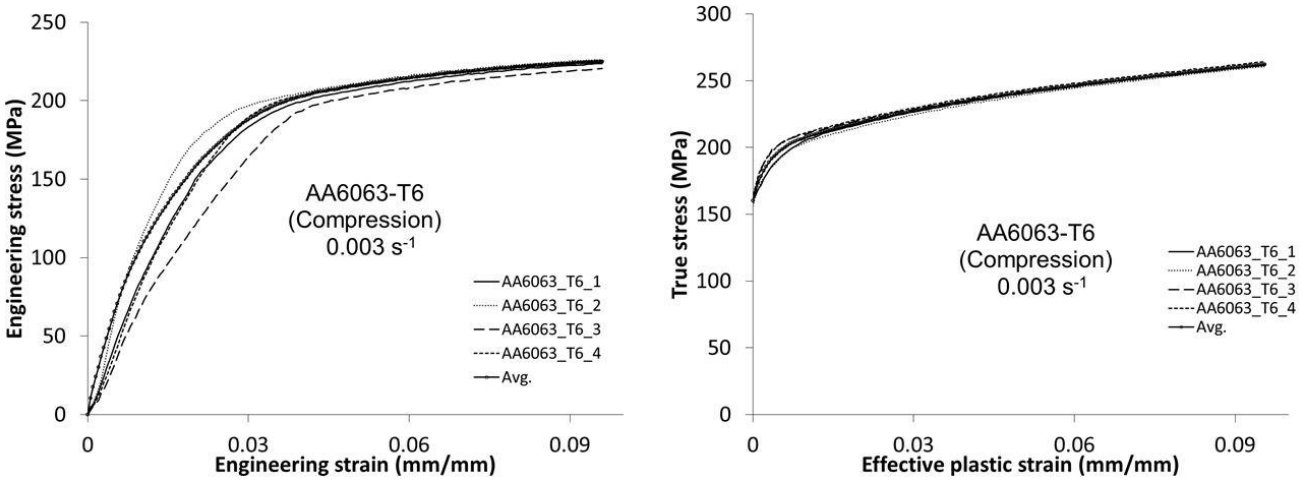

Figure 35 AA6063-T6 through-thickness compression test results

As can be seen from Figure 35, the elastic region exhibits a considerable amount of variability. The primary cause for this scatter is speculated to be associated with the inconsistency in the adhesive layer from sample to sample. Removing the elastic strains from each experiment using the measured modulus resulted in good agreement in the measured compressive stress-strain behavior between tests. The compression strain measurements are obtained using DIC techniques in a similar manner to that of the tensile experiments. The compression sample maintains a rectangular shape until around 10-12% compression strain, after which, the sliding occurs. Figure 36 illustrates the snapshot of the DIC analysis of the compression specimen. As can be seen from the image, the specimen is compressed uniformly at the early stages of the experiment. The data used for the yield surface calibration under biaxial tension is extracted from the region of the sample which exhibits uniform compression through-thickness.

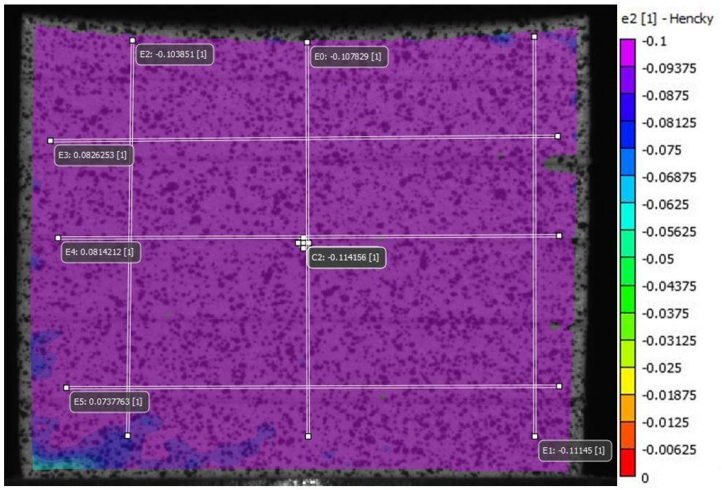

Figure 36 DIC image of though-thickness compression experiment. Contours are of Hencky strain.

The biaxial r-value is calculated by taking the ratio of plastic strain in the width and length directions [31]:

$$r_b = \frac{\varepsilon_{TD}}{\varepsilon_{ED}} \tag{26}$$

Where r_b, ε_y and ε_x represent the equal-biaxial r-value, and plastic strain components in the transverse and extrusion directions, respectively. Table 6 shows the r-values obtained from the through-thickness compression (TTCT) experiments.

Table 6 r-values from through thickness compression experiments

Through thickness compression	**σ_b [MPa]**	**r-value**
6063-T6_1	160.8	0.52
6063-T6_2	156.4	0.34
6063-T6_3	159.5	0.34
6063-T6_4	164.5	0.21
Average	**3.3**	**0.36**
Std. Dev	**160.3**	**0.13**

The average biaxial r-value is 0.36. Similar levels of variability from TTCT were reported by Achani *et al.* [30]. In the same work, the biaxial r-value of 0.48 was obtained from TTCT experiments.

3.3 Strain rate sensitivity

Due to mechanical limitations of the intermediate and high strain rate tensile testing apparatuses, the strain rate sensitivity of the alloy was studied using Mini DB specimens. The major strain contours are overlaid on the surface of a Mini DB specimen at various levels of deformation in Figure 37. This sample was tested in the extrusion direction at strain rate of 10^{-1} s^{-1}. The true strain is distributed uniformly along the gauge length of the specimen until localization when necking of the specimen initiates.

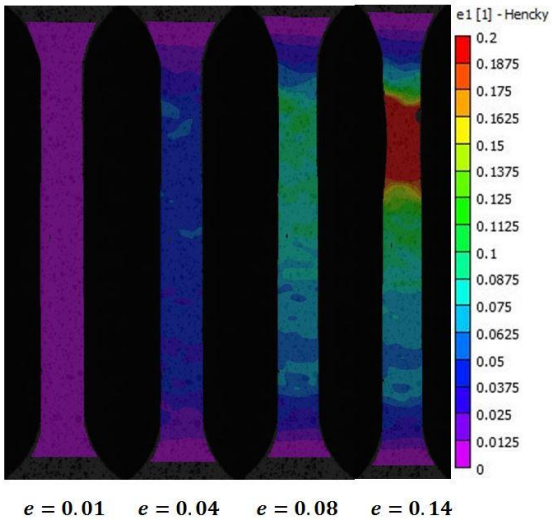

Figure 37 DIC image of mini DB tensile experiment in extrusion direction (10^{-1} s^{-1}). Contours are of Hencky strain.

The strain rate sensitivity is characterized in terms of the flow stress for a given plastic strain level as a function of strain rate. This data is plotted for the extrusion direction in Figure 38 where the equivalent stress is plotted against strain rate at 2%, 4% and 6% plastic strains. The horizontal axis is plotted as a logarithmic scale.

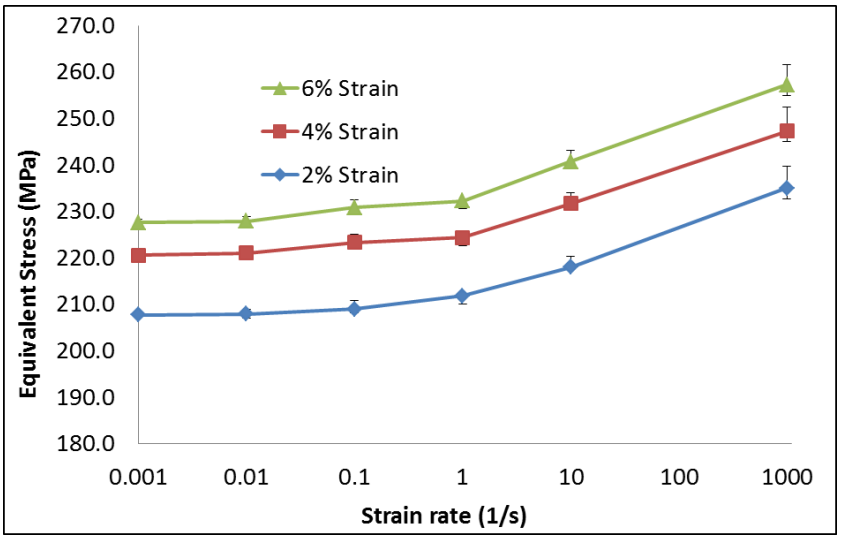

Figure 38 Strain rate sensitivity of the AA6063-T6 alloy in the extrusion direction. Note that the data at 1000 s-1 was provided by Rahmaan [71].

The AA6063-T6 alloy exhibits low strain rate sensitivity in the regime between 10^{-3} s^{-1} and 10^{-1} s^{-1}. The rate sensitivity becomes significant after a strain rate of 1 s^{-1} with an increase in flow stress of 25 MPa at a strain rate of 1000 s^{-1}. From the same graph, it can be seen that the alloy hardens by 20 MPa between 2% and 6% strain. Similar tensile tests at different strain rates were performed in the diagonal and transverse directions as well. Figure 39 and Figure 40 illustrate the AA6063-T6 alloy strain rate sensitivity associated with these directions.

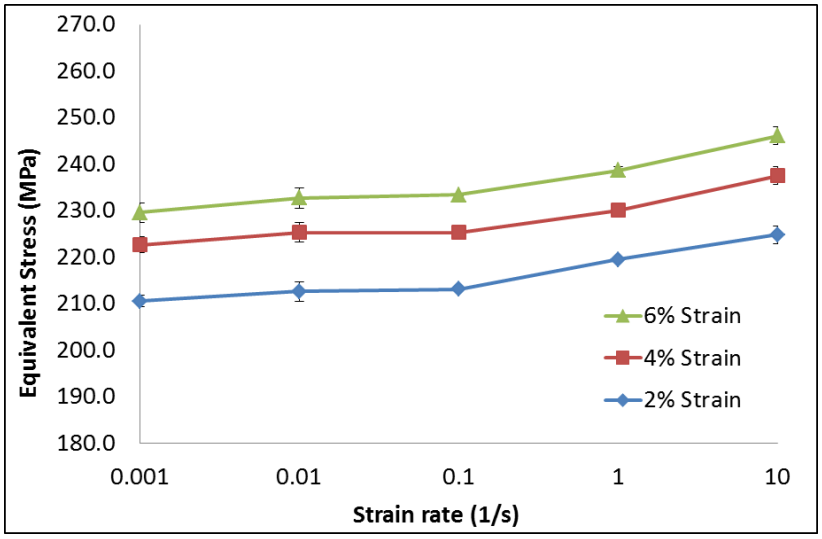

Figure 39 Strain rate sensitivity of the AA6063-T6 alloy in the diagonal direction

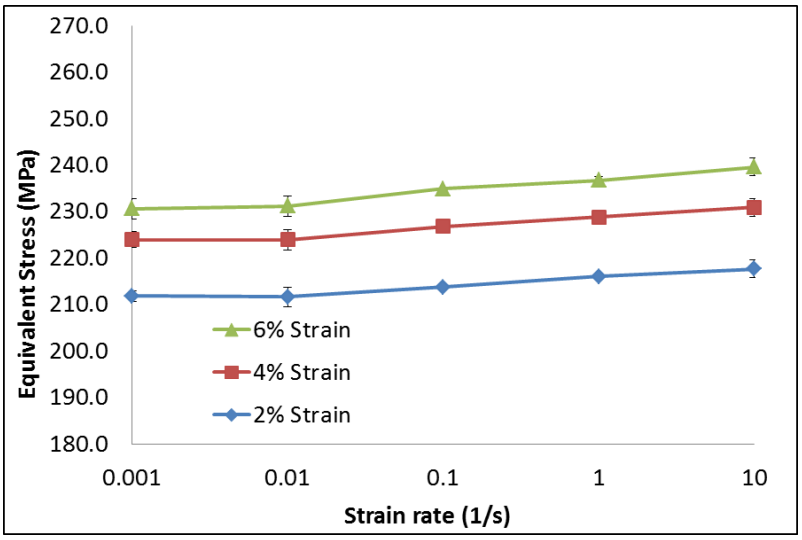

Figure 40 Strain rate sensitivity of the AA6063-T6 alloy in the transverse direction

Note that due to the limited availability of the TSHB apparatus, tensile experiments at 1000 s^{-1} were performed only in the ED. The flow stress in the ED, DD and TD directions increased by 10, 14 and 6 MPa, respectively, for a change in strain rate from 10^{-3} s^{-1} to 10 s^{-1}. This level of rate sensitivity is generally viewed as moderate.

3.4 Shear experiments

The shear stress from the shear experiments was calculated by dividing the measured force by the shear gage area as shown in the equation below [57]:

$$\tau = \frac{F_{shear}}{A_{shear}} = \frac{F_{shear}}{L_{shear} t_{shear}} \tag{27}$$

where τ, F_{shear}, L_{shear} and t_{shear} are the shear stress, the shear force, the length of the shear region and the thickness of the sample respectively. The shear strains are measured using the DIC technique following the approach detailed by Abedini *et al*. [58]. It is important to note that the orientation of the sample does not align with the loading direction. The orientation has an offset of 45° due to the nature of the shear mechanics in addition to the 11° offset imposed by the notch eccentricity in the sample geometry. This means that the sample cut in the DD from the sheet has a principal loading in the ED, as described by Abedini *et al*. [58].

The shear experiments were performed on the samples machined in the ED and DD of the sheet. Each test condition was performed three times for repeatability. Figure 41-Figure 42

illustrate the results of the shear experiments obtained from the DIC analyses. The details of the shear experimental techniques are discussed in depth by Rahmaan *et al*. and Abedini *et al*. [56][58].

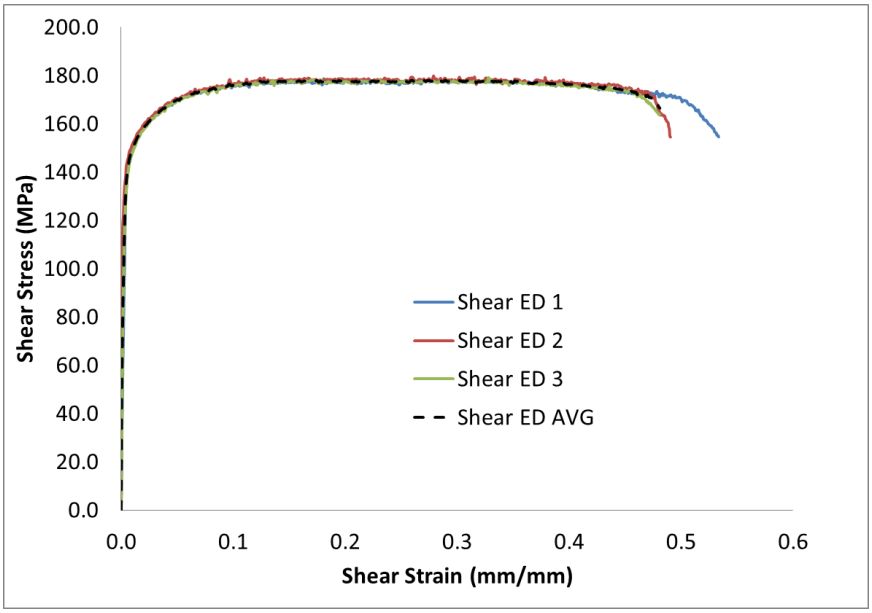

Figure 41 Shear stress - shear strain response of AA6063-T6 alloy in the ED

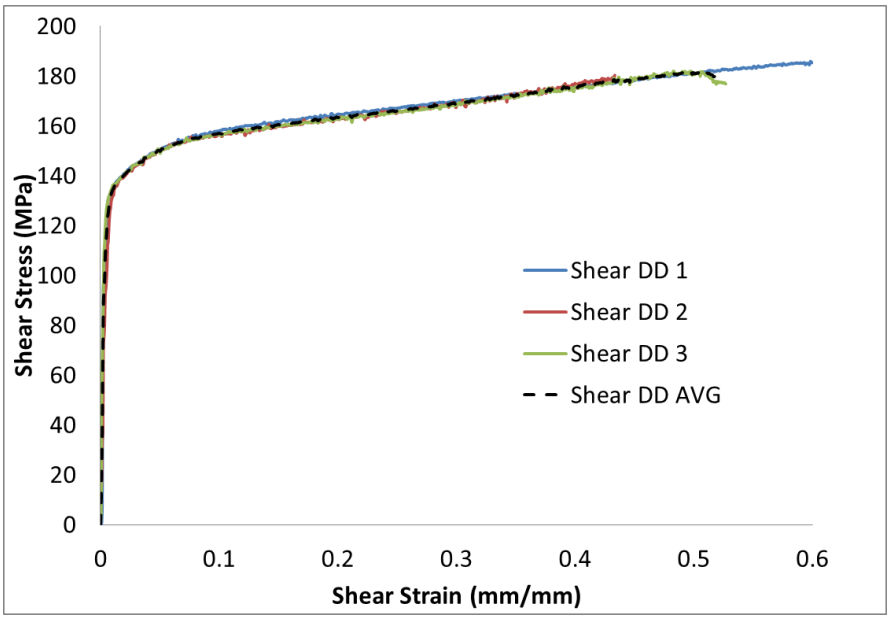

Figure 42 Shear stress - shear strain response of AA6063-T6 alloy in the DD

As can be seen from the figure above, the results from the shear experiments exhibit excellent repeatability. The main advantage of the shear experiment is that the material

undergoes a larger amount of deformation compared to the uniaxial experiment and gives a better basis for modeling the hardening behaviour of the alloy. Figure 43 shows the average shear stress-strain in the ED and DD plotted in the same graph.

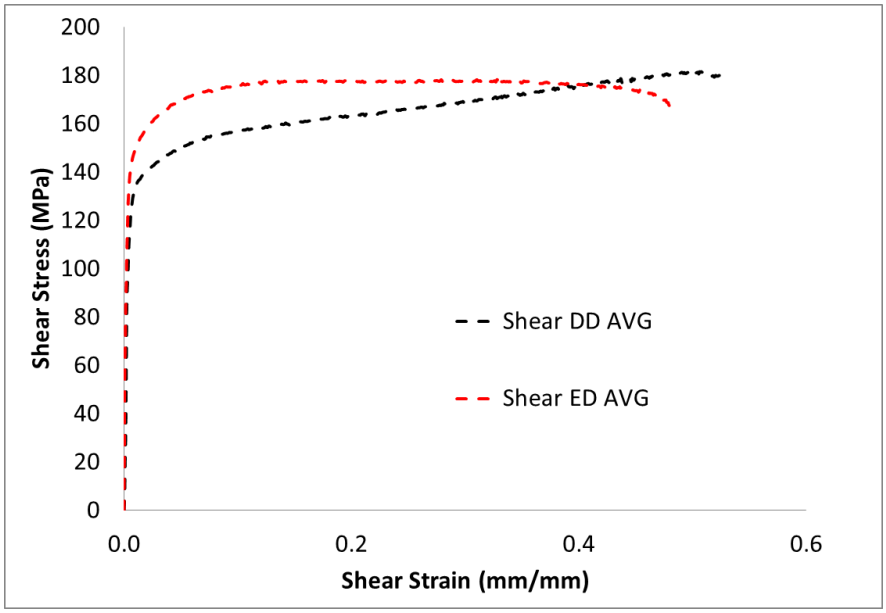

Figure 43 The average shear stress - shear strain response of AA6063-T6 alloy ED *vs.* DD

As can be seen from Figure 43, the shear stress-strain response varies depending on the loading direction. The first obvious difference is the yield stress between the two directions, ED being larger. Another difference is the hardening behaviour. The material starts softening in the ED after around 15% shear strain, whereas, in the DD, the material continues hardening until fracture.

3.5 Crush Experiments

As was mentioned earlier, three profile and extrusion material combinations were crushed axially in dynamic and quasi-static crush modes. Table 7 lists the test parameters used in the crush experiments.

Table 7 Crush experiment test parameters

Profile	Material	Impact velocity	Sled mass
Omega	AA6063-T6	7.8 m/s	1141 kg
		0.508 mm/s	N/A
Omega	AA7003-T6	7.8 m/s	1141 kg
		0.508 mm/s	N/A
UWR4	AA6063-T6	7.8 m/s	1141 kg
		0.508 mm/s	N/A

3.5.1 Dynamic axial crush

The crushing distance for the rails is calculated by double integrating the average sled deceleration obtained from the onboard accelerometers. The initial velocity is used to calculate the velocity profile:

$$v^{(i)} = v^{(i-1)} + a^{(i)}(t^{(i)} - t^{(i-1)}) \tag{28}$$

Where v is the velocity, t is the time and (i) and $(i-1)$ represent current and previous time respectively (note that the acceleration is negative). The crushing distance is then calculated from the velocity as:

$$d^{(i)} = d^{(i-1)} + v^{(i)}(t^{(i)} - t^{(i-1)}) \tag{29}$$

where d represents the crush distance. The energy absorption curves are calculated by integrating the force-displacement using the trapezoid rule as shown below [50]:

$$E^{(i)} = E^{(i-1)} + \frac{1}{2}(F^{(i)} + F^{(i-1)})(d^{(i)} - d^{(i-1)}) \tag{30}$$

where E represents the energy absorbed by the rail during the crush event. As discussed earlier, the uninterrupted crush length is different for rails with different cross-sections due to the specifics of the dynamic axial crush experimental setup. In order to enable a one-to-one comparison, the total energy absorbed and average load are calculated for 120 mm of uninterrupted progressive folding of each rail. The average load is calculated as shown below:

$$F_{ave} = \frac{E_{(l)}}{d_{(l)}} \tag{31}$$

where F_{ave} represents the average force and subscript l represents the crushing distance.

The specific energy is calculated by dividing the total energy absorbed at 120 mm of crushing distance by the mass of the 120 mm length of crushed rail. It should be noted that the energy absorbed by the rail at a certain crush length does not depend on the overall length of the rail (in the absence of global buckling). Hence, the crushed rail length is considered for calculations of the SEA of respective rails in this work. The formula for the specific energy absorbed is shown in the equation below [4]:

$$E_{SEA} = \frac{E_{(l)}}{m_{(l)}} \tag{32}$$

Where E_{SEA} and $m_{(l)}$ represent the specific energy absorbed (SEA) and mass of the rail with length l respectively.

The force-displacement curves of three dynamic axial crush experiments are shown in Figure 44. These experiments were carried out on rails composed of the baseline alloy extruded with the Omega profile. The initial peak in the force is due to the formation of the initial fold. The crush distance represents the uninterrupted crush where only the rail is resisting the force applied by the sled (prior to the sled contacting the honeycomb). For the Omega rail extruded from AA6063 alloy, this distance is equal to 124 mm. The honeycomb contact with the sled is seen distinctively on the force-displacement curve and corresponds to the onset of a higher level of oscillation in the crush force signal. The repeatability between the three tests is very good. The peak load for one of the tests is lower compared to the other two, possibly due to differences in mounting or alignment of the rail in the fixture. Figure 45 shows the energy absorption of the baseline profiles extruded from baseline alloy. The energy absorption of the rails exhibits very good repeatability.

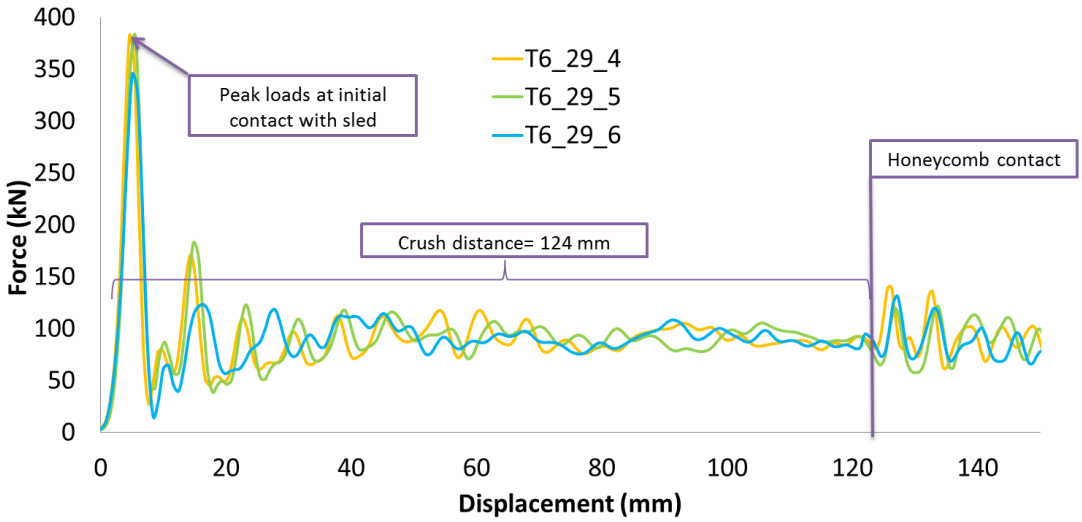

Figure 44 Dynamic force-displacement curves for Omega AA6063-T6 rails

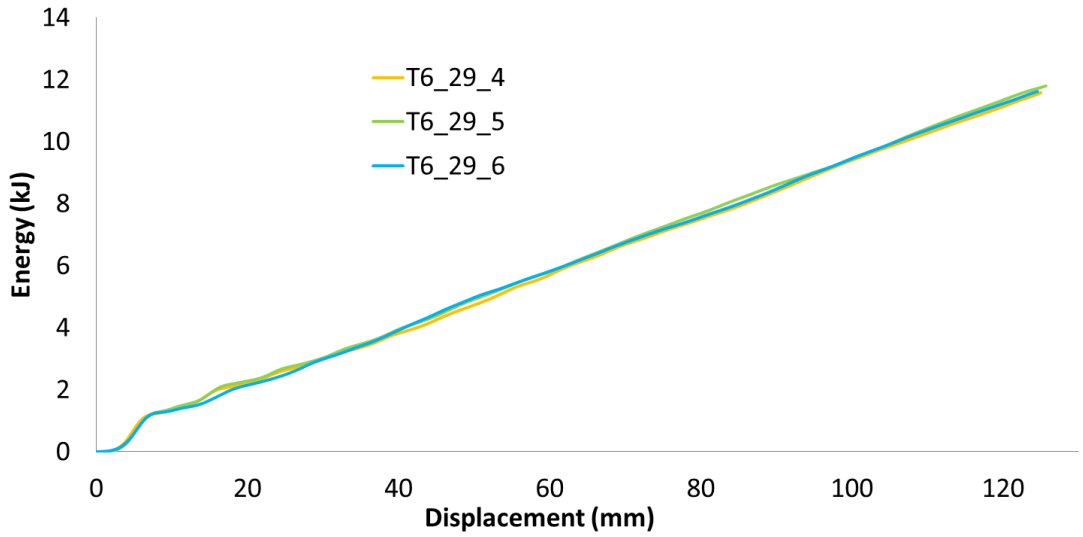

Figure 45 Dynamic energy absorption curves for Omega AA6063-T6 rails

Table 8 summarizes the dynamic crush performance of the Omega AA6063-T6 aluminum rails. The crushing distance considered in the calculations, peak loads, average loads, energy absorbption and specific energy absorbed are summarized for three repeats of the dynamic axial crush experiment. The average specific energy absorbed by the Omega AA6063-T6 rails during

dynamic axial crush is observed to be 33.5 kJ/kg. As was expected from the curves above, there is good repeatability across all the parameters measured during the axial crush experiment.

Table 8 Omega AA6063-T6 dynamic axial crush summary

Test #	Crush distance [mm]	Peak load [kN]	Average load [kN]	Energy absorbed [kJ]	Specific energy absorbed [kJ/kg]
Omega_29_4	120.7	382.5	92.8	11.2	33.2
Omega_29_5	120.6	382.6	94.5	11.4	33.8
Omega_29_6	120.5	345.3	93.5	11.3	33.5
Average	**120.6**	**370.1**	**93.6**	**11.3**	**33.5**
Std. Dev.	**0.1**	**21.5**	**0.85**	**0.1**	**0.3**

Figure 46 shows the force-displacement curves for dynamic axial crush of the UWR4 rails. The uninterrupted crush distance is 128 mm for this setup.

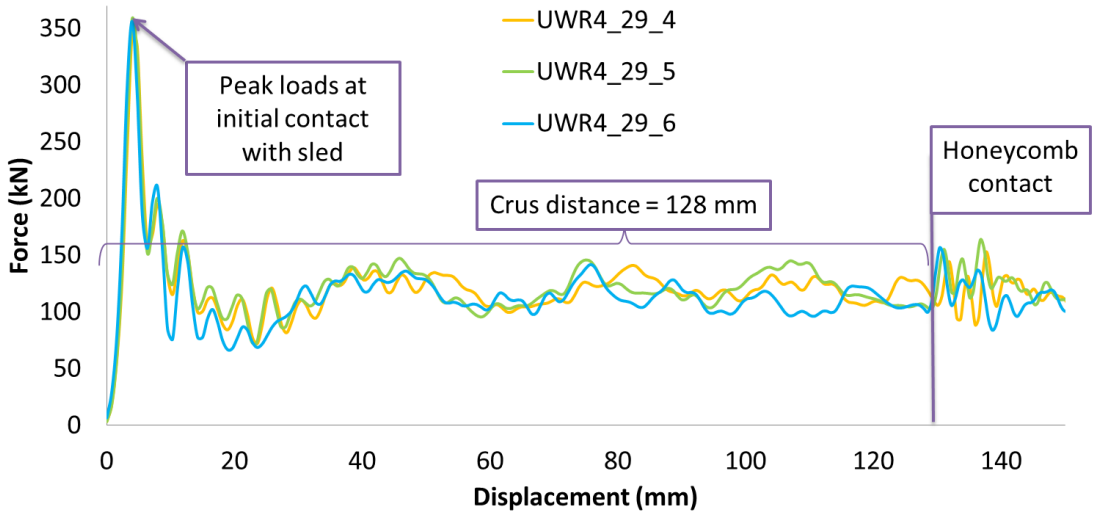

Figure 46 Dynamic force-displacement curves for UWR4 AA6063-T6 rails

Figure 47 illustrates the dynamic energy absorption curves for the UWR4 rails. The lower force-displacement shown by one of the tests resulted in a distinctively lower energy absorption for that case. This lower energy absorption is the result of the comparatively greater degree of visible fracture in this specimen on that particular rail, as described in the following.

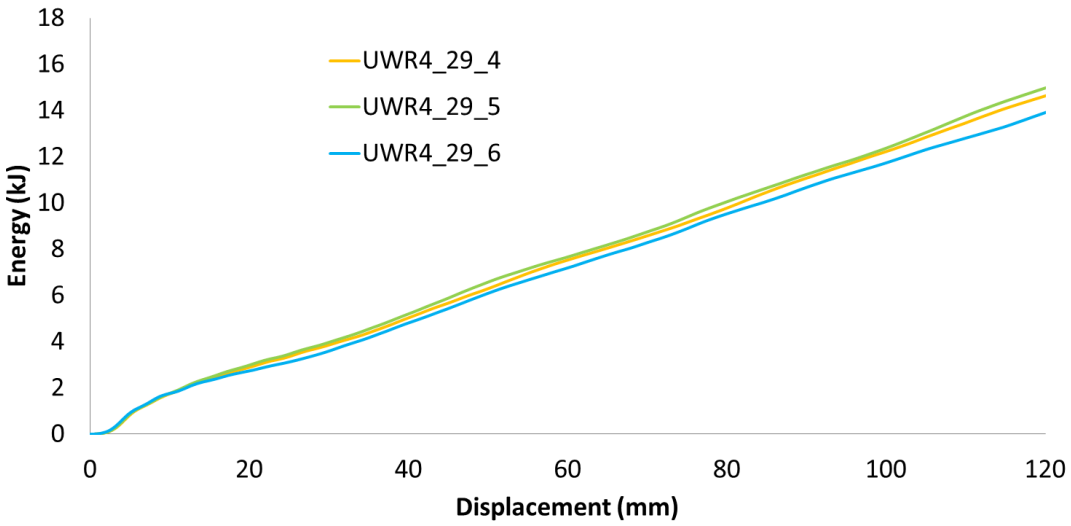

Figure 47 Dynamic energy absorption curves for UWR4 AA6063-T6 rails

Figure 48 shows top and side views of the axial crush event for two of the UWR4 aluminum rail. As can be seen from the top and side views of the UWR4_6063_D_3 experiment, severe fracture is present at the front end of the rail in the folded region.

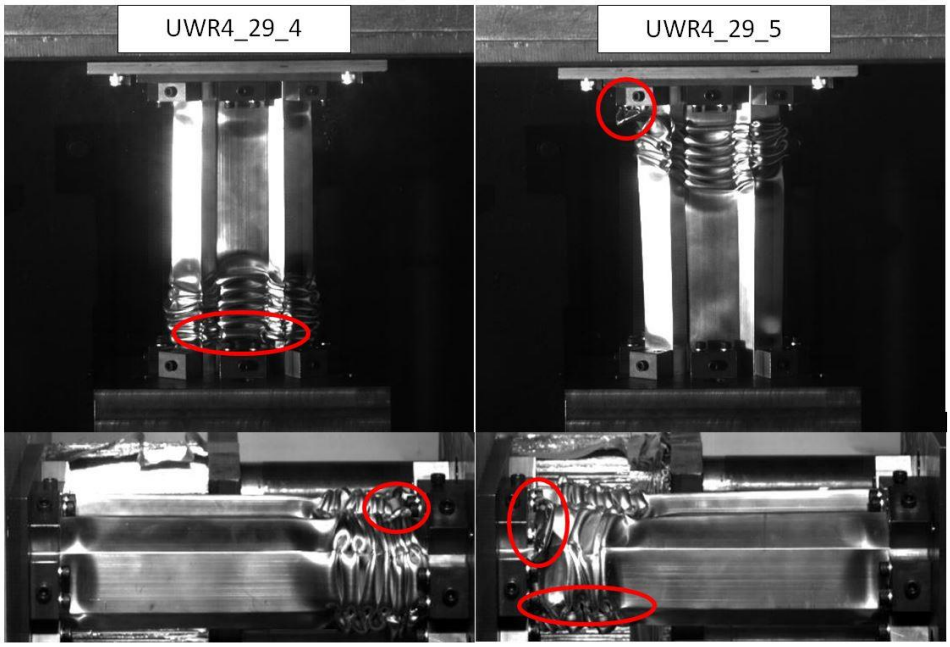

Figure 48 UWR4 dynamic axial crush images from high-speed cameras. The circles highlight regions in which cracking was observed.

The onset of the fracture is reflected in the energy absorption curve for the UWR4_6063_D_3 experiment which starts to deviate from the other two repeats after approximately 20 mm of crush.

Table 9 summarizes the three repeats of the axial crush experiments using UWR4 AA6063-T6 aluminum rails. As expected from the energy absorption curves shown in Figure 47, the average load for one of the repeats is lower compared to the other two repeats. The higher extent of the fracture in test three resulted in lower energy absorbed in axial crush. Even though the peak load for the first test listed is the lowest, the lowest specific energy absorbed is seen in the third test. The average specific energy absorbed for UWR4 AA6063-T6 aluminum rails is observed to be 45.3 kJ/kg.

Table 9 UWR4 AA6063-T6 dynamic axial crush summary

Test #	Crushing distance [mm]	Peak load [kN]	Average load [kN]	Energy absorbed [kJ]	Specific energy absorbed [kJ/kg]
UWR4_29_4	120.2	345.0	121.9	14.7	45.9
UWR4_29_5	120.4	358.2	124.8	15.0	47.0
UWR4_29_6	120.2	356.5	116.0	14.0	43.7
Average	**120.3**	**353.2**	**120.9**	**14.6**	**45.5**
Std. Dev.	**0.1**	**7.1**	**4.5**	**0.5**	**1.7**

Omega cross-section rails extruded from higher strength AA7003 alloy in T6 condition were axially crushed in dynamic and quasi-static modes as well. Figure 49 shows the dynamic force-displacement curves for the three repeat experiments on the Omega 7003-T6 rails. The uninterrupted crush distance was equal to 123 mm for these experiments. The Omega rails extruded from AA7003 alloy require higher loads to initiate the first fold. The repeatability between the experiments was relatively good.

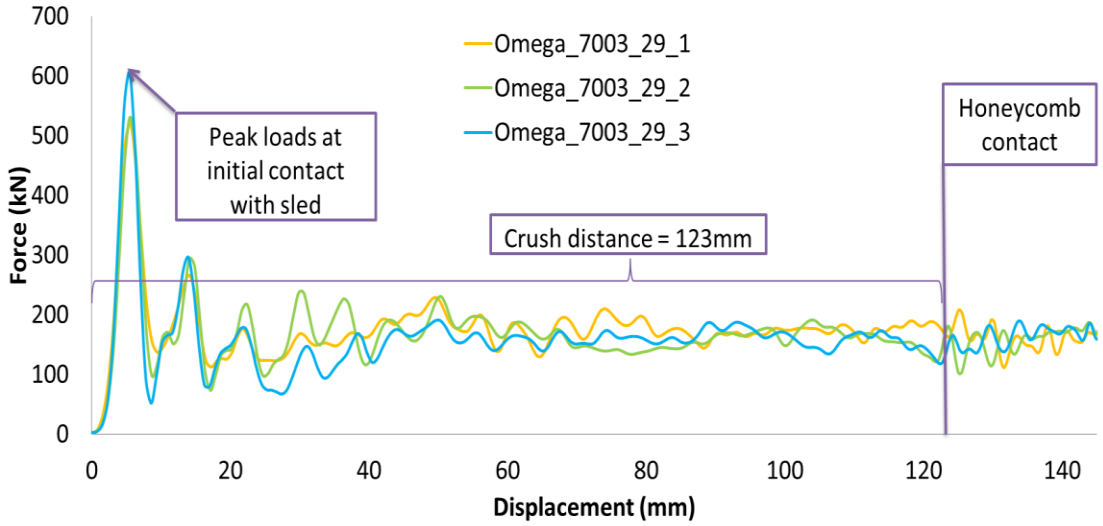

Figure 49 Dynamic force-displacement curves for Omega AA7003-T6 rails

Figure 50 illustrates the energy absorption curve for the rails composed of AA7003-T6 alloy with the Omega profile. One of the three repeats absorbed less energy compared to the other two experiments. The differences in final energy absorbed are again attributed to different degrees of the fracture in the rails after the experiment. Figure 51 shows images from high speed video taken of the Omega 7003 aluminum rails; as can be seen from the images, all three rails have different degrees of fracture taking place resulting in different amounts of absorbed energy.

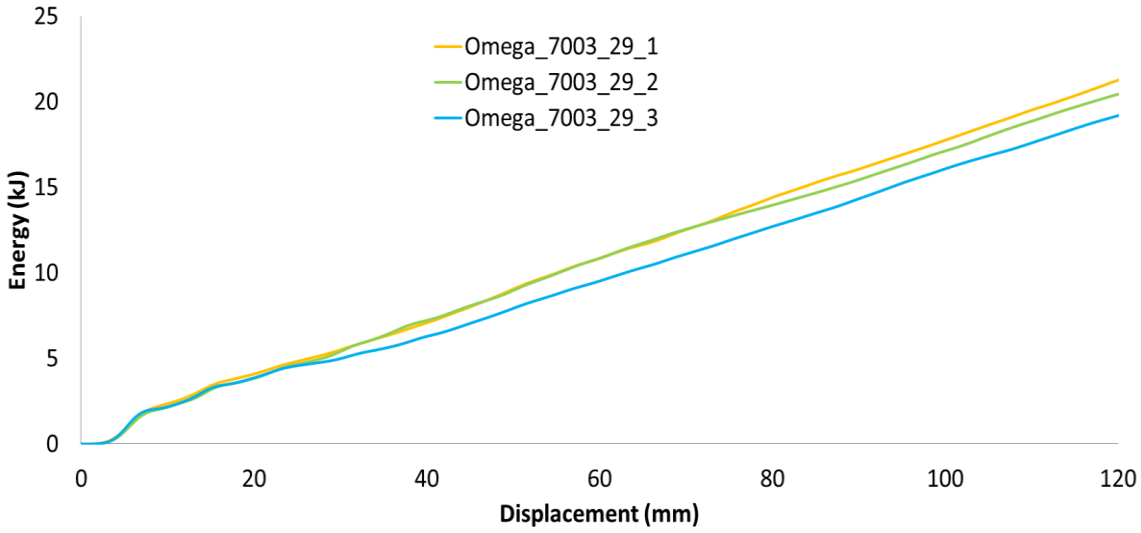

Figure 50 Dynamic energy absorption curves for Omega AA7003-T6 rails

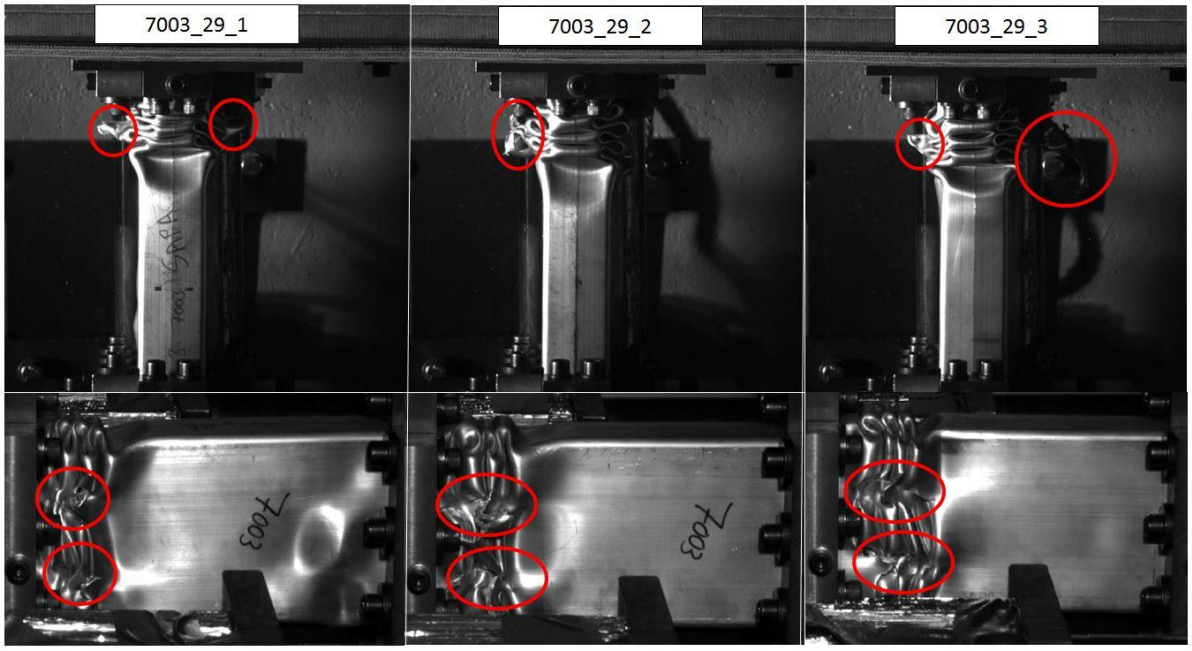

Figure 51 AA7003-T6 Omega extrusion dynamic axial crush images. The circles highlight regions in which cracking was observed.

Table 10 summarizes the dynamic axial crush experiments for the Omega AA7003-T6 rails.

Table 10 Omega AA7003-T6 dynamic axial crush summary

Test #	Crushing distance [mm]	Peak load [kN]	Average load [kN]	Energy absorbed [kJ]	Specific energy absorbed [kJ/kg]
7003_29_1	120.1	520.5	177.2	21.3	54.9
7003_29_2	120.1	530.8	170.3	20.4	52.8
7003_29_3	120.0	605.5	159.9	19.2	49.6
Average	**120.1**	**552.3**	**169.1**	**20.3**	**52.4**
Std. Dev.	**0.06**	**46.4**	**8.7**	**1.0**	**2.7**

As shown in Table 10 above, the peak loads for the Omega AA7003-T6 rails have higher variance compared to those of the Omega AA6063-T6 and UWR4 AA6063-T6 aluminum rails.

Also, the average load for 7003_29_3 is lower compared to that of the other two repeats. As can be seen from the images acquired by the high speed cameras, all three tests have different degrees of fracture. Consequently, there is a greater variance in the crashworthiness properties of the Omega AA7003-T6 rails. The average specific energy absorbed is calculated to be 52.4 kJ/g.

3.5.2 Quasi-static axial crush

The three extruded alloy-cross-section combinations were axially crushed under quasi-static conditions using a servo-hydraulic press following the procedure described in Section 2.6.2. The rails are crushed at a constant crosshead velocity of 0.508 mm/s. Similar to the dynamic axial crush response, the force-displacement curves in the quasi-static experiments start off with a high peak load required to initiate progressive folding. Figure 52 shows the measured force-displacement curves for the quasi-static experiments on the AA6063-T6 rails. The repeatability is similar to that of the corresponding dynamic crush experiments. The crosshead displacement of 122 mm was achieved at the end of the tests which corresponds to the free crush distance in the dynamic experiments. The peak loads are lower for the quasi-static experiment compared to the dynamic crush experiments.

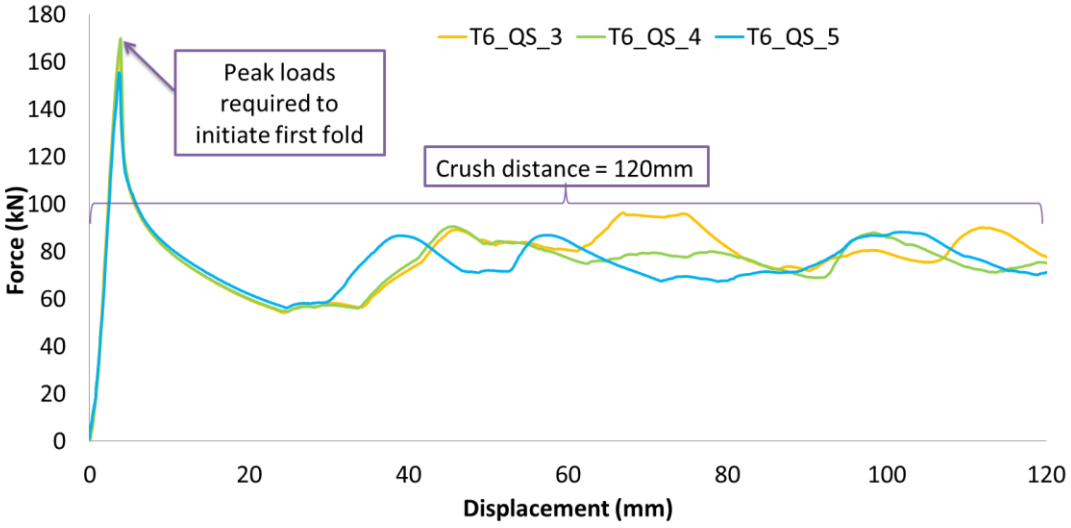

Figure 52 Quasi-static force-displacement curves for Omega AA6063-T6 rails

Figure 53 illustrates the quasi-static energy absorption curves for the same extrusions as mentioned above. The repeatability between three experiments is quite good.

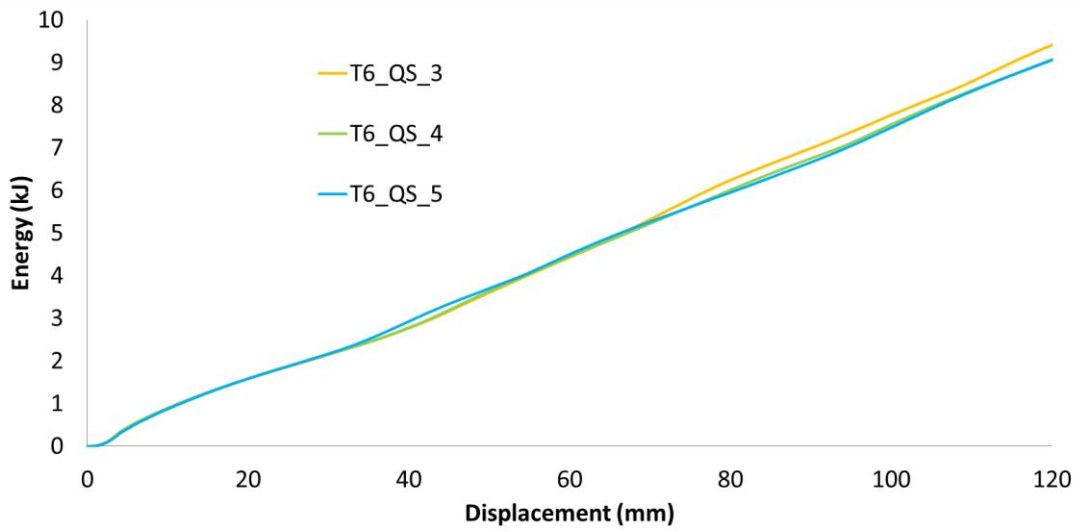

Figure 53 Quasi-static energy absorption curves for Omega AA6063-T6 rails

Table 11 summarizes the quasi-static axial crush experiments for the Omega AA7003-T6 aluminum rails. As in the dynamic axial crush cases, the Omega AA6063-T6 aluminum rails crushed under quasi-static conditions show good repeatability. The average specific energy absorbed for these experiments is calculated to be 27.4 kJ/g based on three repeats.

Table 11 Omega AA6063-T6 quasi-static axial crush summary

Test #	Crushing distance [mm]	Peak load [kN]	Average load [kN]	Energy absorbed [kJ]	Specific energy absorbed [kJ/kg]
Omega_QS_3	120.1	166.9	78.4	9.4	28.1
Omega_QS_4	120.1	169.6	75.7	9.1	27.1
Omega_QS_5	120.1	155.5	75.6	9.1	27.1
Average	**120.1**	**164.0**	**76.6**	**9.2**	**27.4**
Std. Dev.	**0**	**7.5**	**1.6**	**0.2**	**0.6**

Figure 54 illustrates the force-displacement for quasi-static experiments using the UWR4 cross-section and AA6063-T6 alloy rails. The UWR4 rails show very good repeatability in peak loads at the beginning of the crush event, as well as during progressive folding.

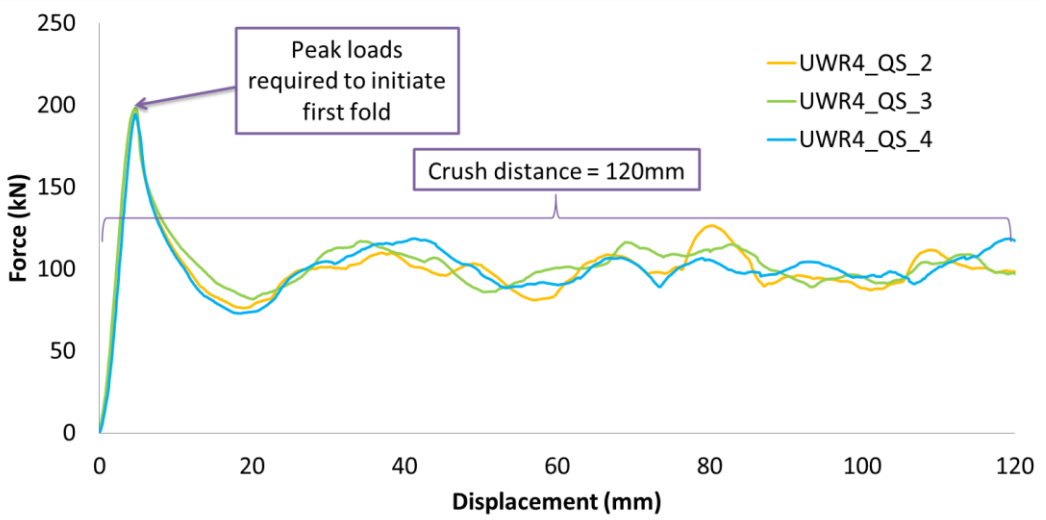

Figure 54 Quasi-static force-displacement curves for UWR4 AA6063-T6 rails

Figure 55 illustrates the quasi-static energy absorption curves for UWR4 AA6063-T6 rails. One of the tests is showing slightly higher energy absorbed overall compared to the rest of the repeats. The differences are due to fracture taking place during the quasi-static crush. In general, UWR4 profiles showed more fracture during quasi-static crush compared to the dynamic crush.

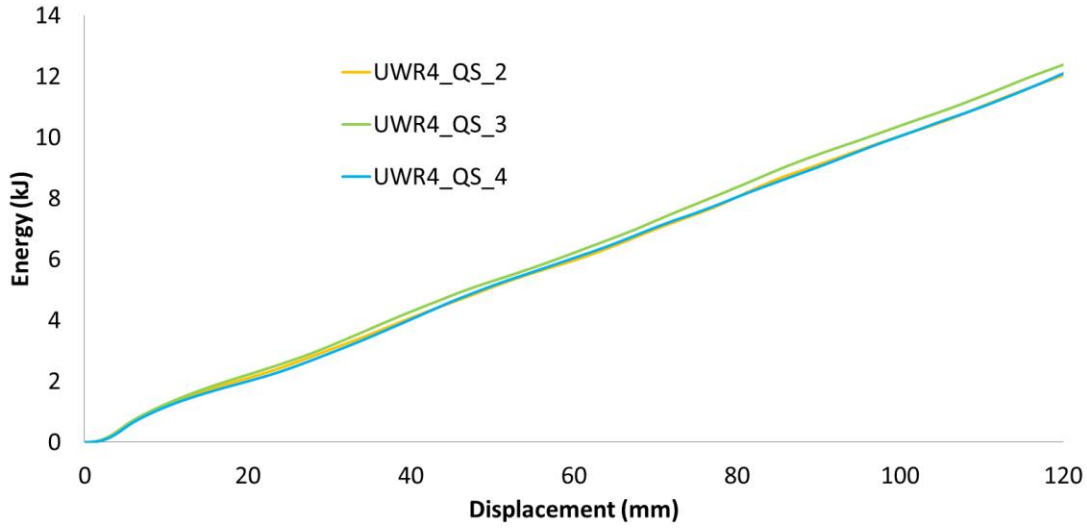

Figure 55 Quasi-static energy absorption curves for UWR4 AA6063-T6 rails

Table 12 summarizes the quasi-static crush experiments for UWR4 AA6063-T6 aluminum rails. All of the crashworthiness parameters acquired from quasi-static axial crush show good agreement between all three experiments. This is despite the fact that a significant amount of

cracking occurs during all three test repeats, as shown in Figure 56. The average specific energy absorbed by the UWR4 rails is calculated to be 38.1 kJ/g based on three repeats.

Table 12 UWR4 AA6063-T6 quasi-static axial crush summary

Test #	Crushing distance [mm]	Peak load [kN]	Average load [kN]	Energy absorbed [kJ]	Specific energy absorbed [kJ/kg]
UWR4_QS_2	120.0	197.6	100.3	12.0	37.7
UWR4_QS_3	120.0	198.4	103.2	12.4	38.8
UWR4_QS_4	120.0	194.7	100.8	12.1	37.9
Average	**120.0**	**196.9**	**101.4**	**12.2**	**38.1**
Std. Dev.	**0**	**1.9**	**1.5**	**0.2**	**0.6**

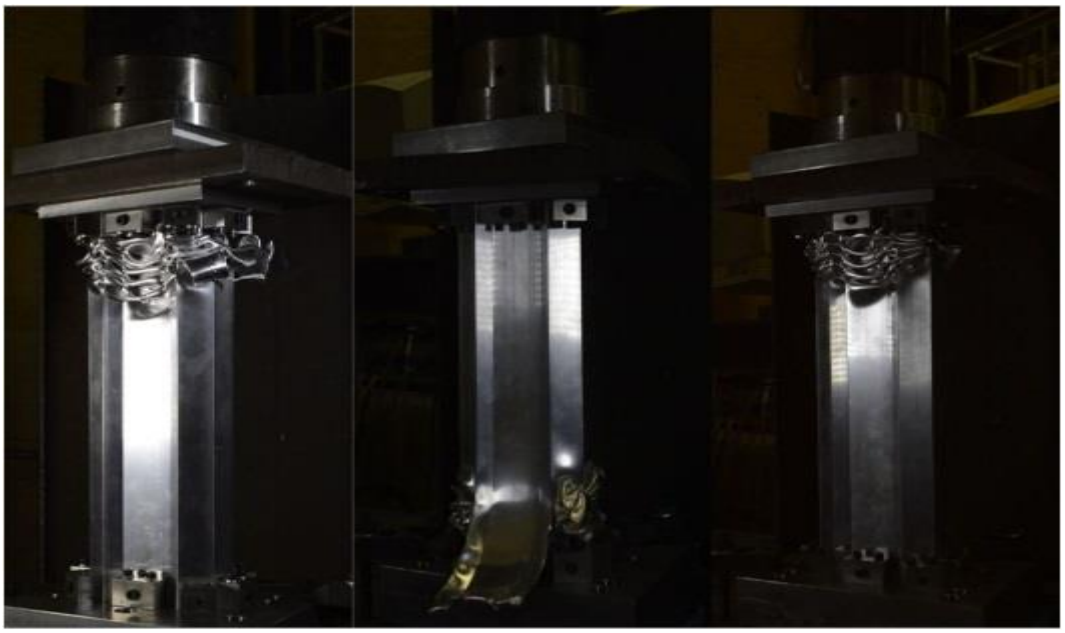

Figure 56 Quasi-static axial crush of UWR4 AA6063-T6 aluminum rails

Figure 57 shows the quasi-static force displacement curves for the baseline profile extruded from AA7003 alloy in the T6 temper condition. Only two quasi-static experiments were performed due to a limitation on the number of available extrusions for this alloy. The repeatability of these experiments was good.

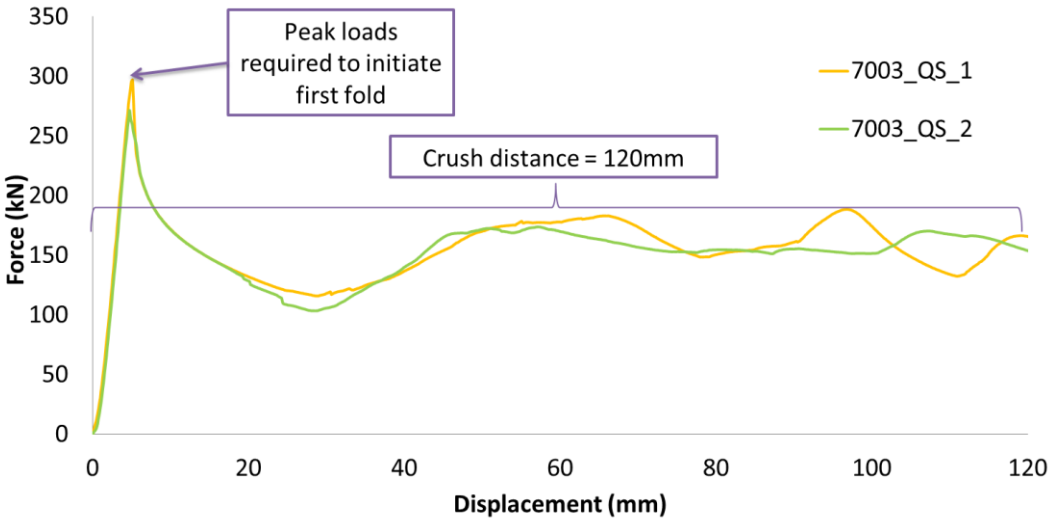

Figure 57 Quasi-static force-displacement curves for Omega AA7003-T6 rails

The quasi-static energy absorption curves for the AA7003 rails are shown in Figure 58. In contrast to the UWR4 rails extruded from AA6063 alloy, the Omega AA7003 rails showed less fracture during the quasi-static experiments compared to the dynamic crush response. Figure 59 shows images of Omega AA7003-T6 rails crushed axially in the quasi-static regime.

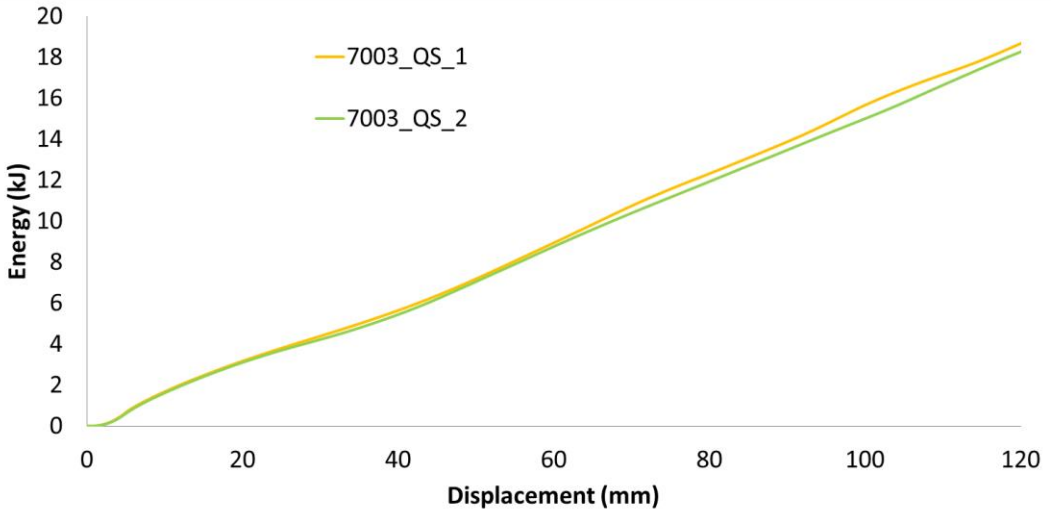

Figure 58 Quasi-static energy absorption curves for Omega AA7003-T6 rails

Table 13 summarizes the quasi-static axial crush response of the Omega AA6063-T6 aluminum rails. Despite the difference in peak load between two tests, the average loads are very close. The average specific energy absorbed for these tests is calculated to be 47.9 kJ/g.

Table 13 Omega AA7003-T6 quasi-static axial crush summary

Test #	Crushing distance [mm]	Peak load [kN]	Average load [kN]	Energy absorbed [kJ]	Specific energy absorbed [kJ/kg]
Omega_AA7003_QS_1	120.0	296.9	155.6	18.7	48.4
Omega_AA7003_QS_2	120.0	271.5	152.2	18.3	47.3
Average	**120.0**	**284.2**	**153.9**	**18.5**	**47.8**
Std. Dev.	**0**	**18.0**	**2.4**	**0.3**	**0.8**

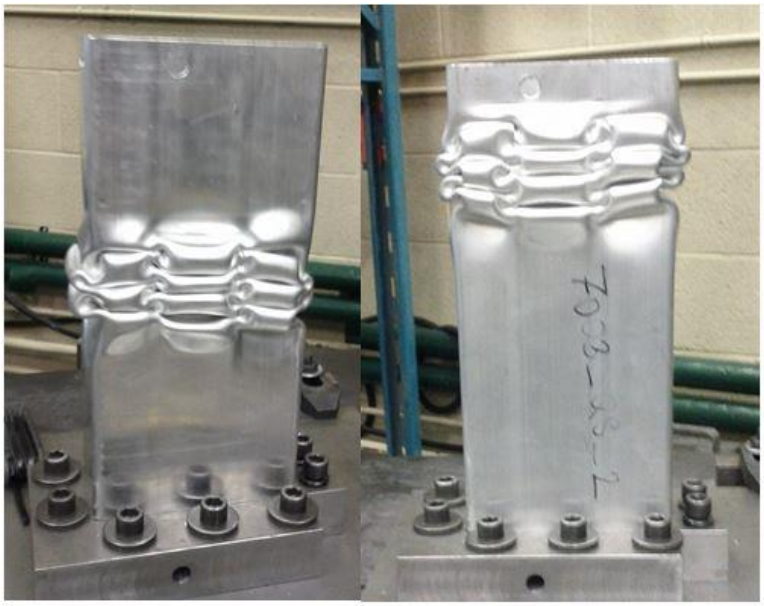

Figure 59 Quasi-static axial crush of Omega AA7003-T6 aluminum rails

3.6 Comparison of crush response of the Omega and UWR4 profiles

This section serves to compare the measured crush response of the AA6063 Omega rails, AA6063 UWR4 rails and AA7003 Omega rails crushed under dynamic and quasi-static loading. Figure 61 summarizes the average crush loads obtained from the dynamic and quasi-static axial crush experiments, whereas the peak loads are shown in Figure 60.

Figure 60 summarizes the average loads obtained from dynamic and quasi-static axial crush of the aluminum rails investigated. Comparing the various sections, the AA7003 Omega rails have the highest average load under both dynamic and quasi-static loading conditions (Figure 60).

The UWR4 rails exhibit crush loads that are intermediate to those of the AA6063-T6 and AA7003-T6 Omega rails. Adopting the AA6063-T6 Omega rails as a baseline, the AA6063-T6 UWR4 rails show a 32% increase in dynamic crush force, while the AA7003 Omega rails offer a 81% increase in crush load relative to the AA6063 Omega rails. Each rail configuration tested exhibited higher crush loads under dynamic versus quasi-static conditions. The two AA6063-T6 rails exhibited a 10-22% increase in average crush load under dynamic loading, while the AA7003-T6 rail exhibited a 10% increase. The increase for the AA6063-T6 rails is consistent with the positive strain rate sensitivity of this alloy shown in Figure 38. Similar material rate sensitivity is expected for AA7003-T6, although this was not evaluated in the current study.

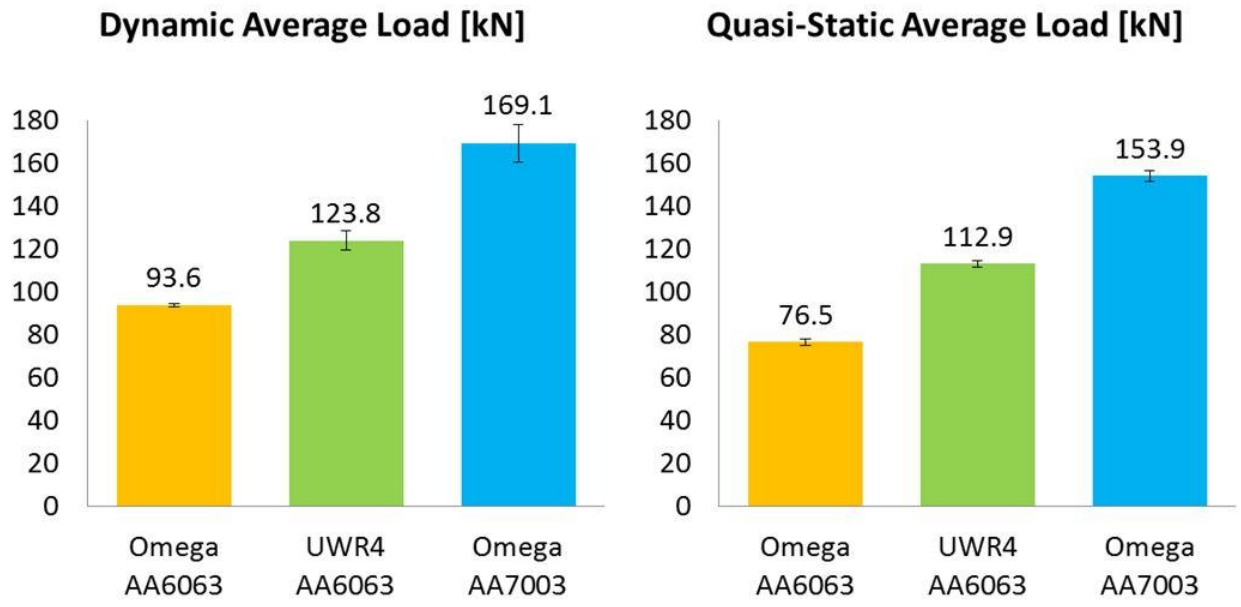

Figure 60 Dynamic and quasi-static axial crush experiment summary – average loads

All of the rails tested showed a dramatic difference between the dynamic and quasi-static peak loads. In general, the peak loads were 94-195% higher under dynamic conditions. This sharp increase under dynamic loading is thought to be due to inertial effects associated with the time for the first fold to form (in addition to the moderate strain rate sensitivity of the alloys).

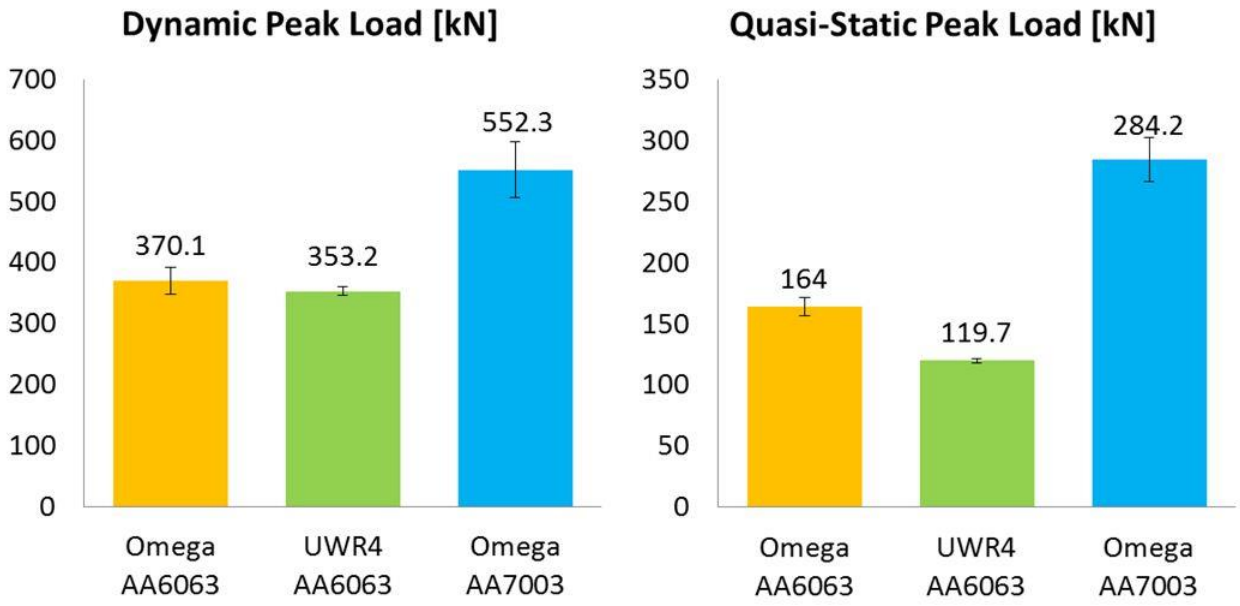

Figure 61 Dynamic and quasi-static axial crush experiment summary – peak loads

Figure 62 summarizes the energy absorbed for a section length of 120 mm for the different rail configurations. The AA6063-T6 Omega rails absorbed 11.3 kJ and 9.2 kJ in the dynamic and quasi-static experiments respectively. The AA6063-T6 UWR4 rails absorbed 29% more energy compared to the AA6063-T6 Omega rails. As expected from the reported average loads, the energy absorbed by the AA7003 Omega rails are the highest among the rails. The energy absorbed by these rails under dynamic and quasi-static loading conditions were 20.3 kJ and 18.5 kJ, respectively.

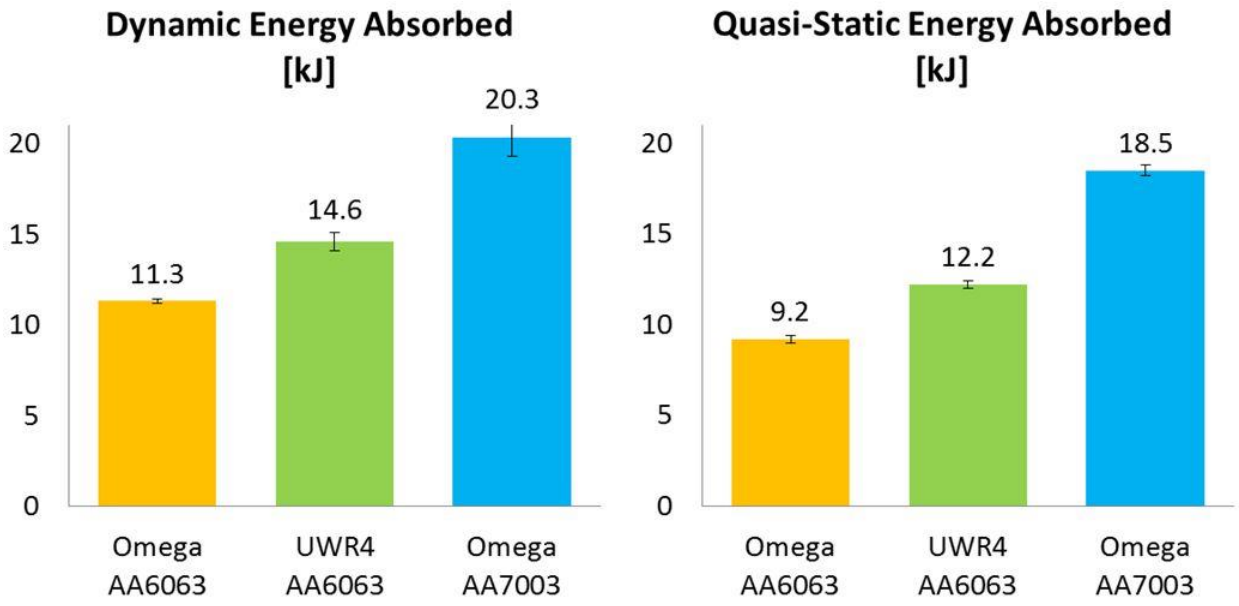

Figure 62 Dynamic and quasi-static axial crush experiment summary – absorbed energy

It is also important to compare the specific energy absorption for the three rail configurations since there were intentional differences between the Omega and UWR4 cross-sections as well as process variations between the two Omega sections (AA6063-T6 versus AA7003-T6 extrusions). Thus the actual masses per unit length for the aluminum rails are summarized in Table 2. As expected from the dynamic energies absorbed, the SEA of the AA7003 Omega rail is the highest compared to the AA6063 rails. The SEA of the AA6063 UWR4 is higher than Omega rail of the same alloy. Taking the SEA of the AA6063 Omega rail as a reference, 36% and 56% relative improvement is observed for UWR4 and AA7003 Omega rails, respectively. It is important to note that accounting for the mass per length of the respective rails better highlights the relative improvement of the UWR4 profile over the Omega. A Similar trend is observed for the quasi-static SEA of the respective rails.

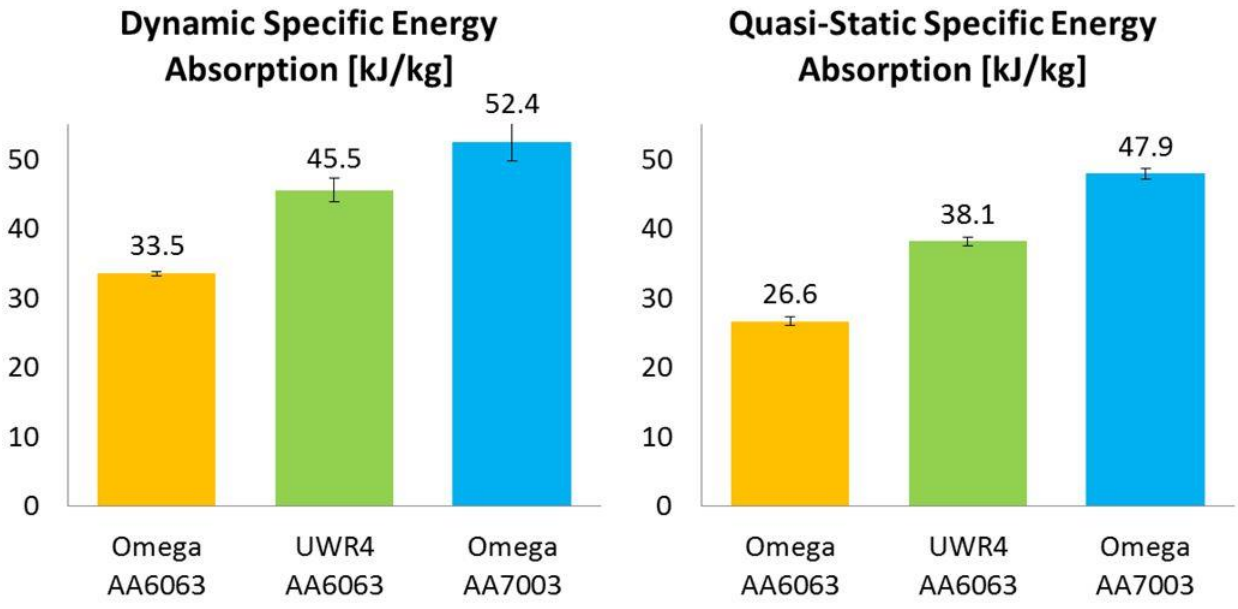

Figure 63 Dynamic and quasi-static axial crush experiment summary – specific energy absorbed

4 Axial Crush Model Development

This section highlights the details associated with the model development of the dynamic and quasi-static axial crush events. The crush experiments were simulated using the commercial FEA software LS-Dyna.

4.1 Constitutive material model

4.1.1 YLD2000-2d

As was discussed in the literature review (Section 1.3), isotropic yield functions are inappropriate for describing the mechanical behaviour of extruded aluminum alloys. The anisotropy of the AA6063-T6 alloy is evident from the tensile experimental results (Section 3.1), where differences in the stress-strain response and r-values (Lankford parameters) manifest with respect to different loading angles. The stress ratios and Lankford parameters required for calibrating the yield surface are obtained from the tensile experiments performed on MJIS samples. The stress ratios for yield function calibration were taken at the same plastic work level of 10.1 MJ/m^3 in each of the experiments. The plastic work for tensile and compression experiments are calculated as shown in the equation below:

$$W_p = \int_0^{\varepsilon_{pl}} \sigma_{true} d\varepsilon_p$$
$$W_p^i = \frac{1}{2}\left(\sigma_{true}^i + \sigma_{true}^{i-1}\right)\left(\varepsilon_p^i - \varepsilon_p^{i-1}\right) + W_p^{i-1} \quad (33)$$

Where W_p denotes the plastic work. The same approach is used for calculating plastic work for uniaxial tension and uniaxial through-thickness compression. The stress ratios are measured as shown below:

$$R_\theta = \frac{\sigma_\theta}{\sigma_{0^o}} \quad (34)$$

Where R_θ, σ_θ and σ_{0^o} represent the stress ratio, the true stress in the θ^o direction and the true stress in the extrusion direction respectively. Figure 64 shows true stress plotted against the plastic work for the tensile, through-thickness compression and shear experiments.

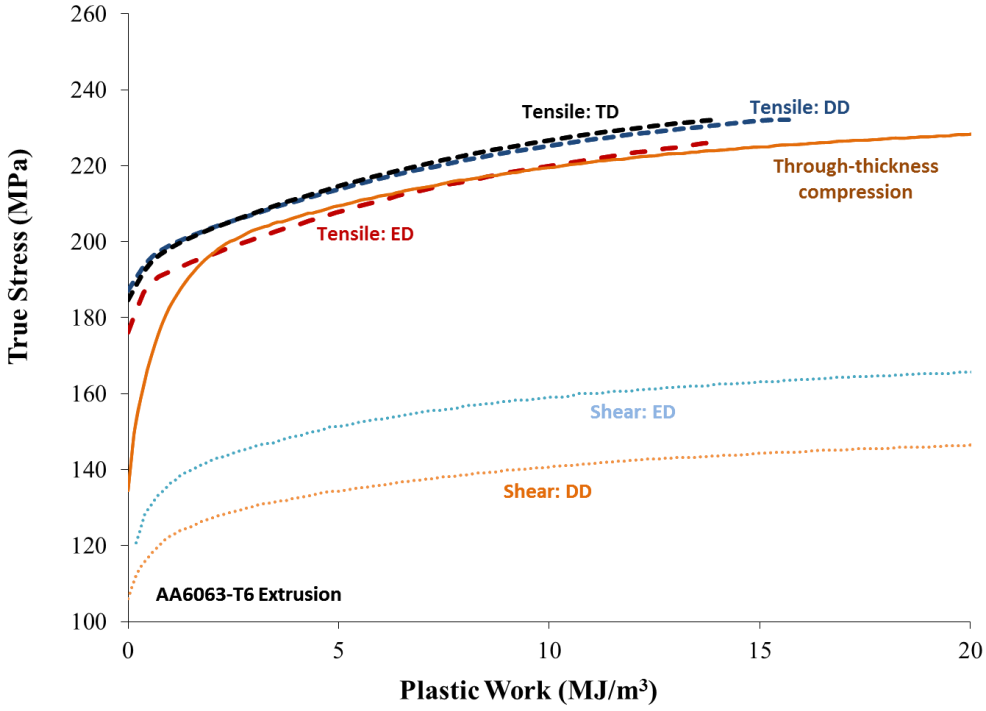

Figure 64 True stress *vs.* plastic work for tensile, compression and shear experiments

All the parameters used to calibrate the yield function are summarized in Table 14.

Table 14 Experimental stress ratios and Lankford parameters used for calibrating YLD2000-2d (taken at the plastic work level of 10.1 MJ/m^3)

Experiment	σ_θ [MPa]	R_θ	r_θ
Uniaxial Tension (ED)	220.1	1	0.37
Uniaxial Tension (DD)	225.6	1.0248	0.43
Uniaxial Tension (TD)	227.0	1.0313	0.86
Through-thickness Compression	219.5	0.9972	0.36
Shear (ED)	159.1	0.7225	N/A
Shear (DD)	140.8	0.6396	N/A

Barlat *et al.* [31] use eight parameters for calibrating the yield function, whereas, in the current study, ten material parameters are used. Shear stress ratios are added to the calibration process to better capture the shear response of the model.

The yield function was calibrated by Butcher [54]. Figure 65 illustrates the result of the YLD2000 function calibrated for the AA6063-T6 aluminum alloy. The isotropic Von-Mises yield locus is plotted on the same graph for comparison purposes. It is important to note that a yield exponent of m=4 resulted [54] in a superior fit for the shear stress ratios as opposed to the recommended m=8 value for FCC materials [31].

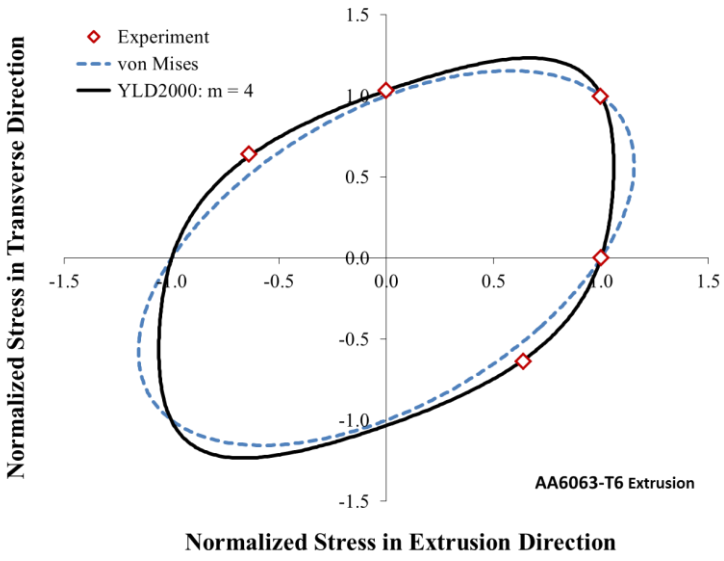

Figure 65 YLD2000 yield surface for AA6063-T6 alloy *vs.* isotropic Von-Mises

The normalized stress ratios (stress normalized by stress in extrusion direction) and r-values resulting from the predictions of the YLD2000 yield locus and the experimental results are plotted as a function of the angle relative to the extrusion direction in Figure 66. The normalized stress values exhibit good agreement with the measured data, while the r-values have good agreement in the transverse direction with some discrepancies along the extrusion and diagonal directions. The normalized shear in the diagonal direction and biaxial stresses also agree well with the measured data as observed in Figure 65. This rather good agreement is expected since the measured data was used in the yield function fitting process.

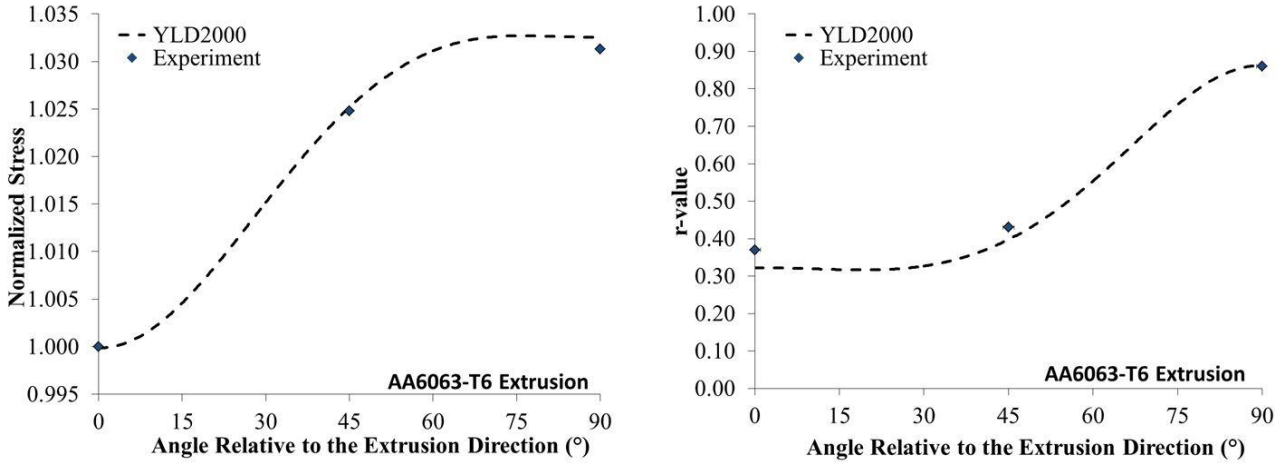

Figure 66 Normalized stress and r-value fits for YLD2000 plotted against material angle

The yield function exponents from the fit by Butcher [54] are summarized in Table 15. This data was input to LS-Dyna and used in the *MAT_133 (*MAT_BARLAT_YLD2000) constitutive model implementation.

Table 15 YLD2000 coefficients

Coefficient	α_1	α_2	α_3	α_4	α_5	α_6	α_7	α_8	m
Value	0.8548	0.8128	0.5054	0.9260	1.1158	1.1459	0.7711	1.2297	4

4.1.2 Hardening and strain rate sensitivity fitting

One of the main approaches to capture the hardening of the behaviour of metals is to fit the flow stress-strain response obtained from uniaxial tensile experiments to appropriate constitutive models. The main challenge in measuring the hardening behaviour of materials is the limited range of data obtained from tensile experiments since samples start to neck at around 8-10% plastic strain (at least for the current AA6063-T6 alloy). Once plastic deformation localizes anywhere in the gauge region of the sample, the state of the stress is not uniaxial anymore and converting the engineering stress-strain to true stress-strain becomes rather complex. On the other hand, shear experiments achieve large plastic strain levels without localization compared to uniaxial tensile tests (refer to Figure 29 and Figure 41). Thus, the large-strain work-hardening behaviour of the AA6063-T6 alloy considered in this study was obtained from quasi-static shear

experiments performed at a strain rate of 10^{-3} s^{-1}. Despite the fact that the hardening behaviour was observed to be different in the ED and DD from the simple shear experiments (Figure 43), it was decided to model the material using an isotropic hardening model. The main reason for adoption of an isotropic hardening assumption was the fact that at its current level of implementation in LS-Dyna, the Barlat-2000 constitutive model (*MAT_133) does not support differential hardening behaviour. To capture this phenomenon more precisely, one would need to implement a user-defined constitutive sub-routine or umat which was judged beyond the scope of the current study.

In order to use the measured shear data to fit the hardening behaviour of the alloy, the shear stress and strain have to be converted to equivalent stress-strain data. As was mentioned in the shear experiment section, the sample orientation and principal loading orientation vary by 45^{o} in the shear experiments. Hence, the results of the shear experiment in the DD are converted to equivalent stress *vs.* plastic strain and used for calibrating the hardening behaviour of the baseline alloy. Shear stresses obtained from simple shear experiments can be converted to equivalent plastic strain through use of work conjugate equivalent plastic strain as described by Rahmaan *et al*. [67] As mentioned in Section 2.3, shear stress can be computed as follows:

$$\tau_{12} = \frac{F}{Lt}$$

where τ, F, L and t are the shear stress, the shear force, the length of the shear region and the thickness of the sample respectively. The logarithmic strain tensor can be decomposed into elastic and plastic components as follows:

$$\varepsilon_{ij} = \varepsilon_{ij}^{e} + \varepsilon_{ij}^{p} \tag{35}$$

where $\varepsilon_{ij}^{e}$and ε_{ij}^{p} are elastic and plastic strain tensors. Using Hooke's law, the elastic strain component can be approximated as (under plain stress assumption, where $\sigma_2 = -\sigma_1, \sigma_3 = 0$):

$$\varepsilon_{1}^{e} = \frac{\tau_{12}}{2G} \tag{36}$$

where G is the shear modulus. Finally, the plastic strain component for shear loading can be computed as

$$\varepsilon_1^p = \varepsilon_1 - \frac{\tau_{12}}{2G} \tag{37}$$

Then, the plastic work increment can be computed using plastic work equivalence:

$$dw_{shear}^p = \int 2\tau_{12} d\varepsilon_1^p = \sigma_{eq} d\varepsilon_{eq}^p \tag{38}$$

Now, the work conjugate equivalent plastic strain increment can be found as:

$$d\varepsilon_{eq}^p = 2\left(\frac{\tau_{12}}{\sigma_{eq}}\right)\left(d\varepsilon_1 - \frac{d\tau_{12}}{2G}\right) \tag{39}$$

where $\frac{\tau_{12}}{\sigma_{eq}}$ is the stress ratio between the shear stress and tensile stress in the reference direction.

Figure 67 illustrates the results of the shear stress to true stress conversion compared to the true stress obtained from the uniaxial tensile experiment.

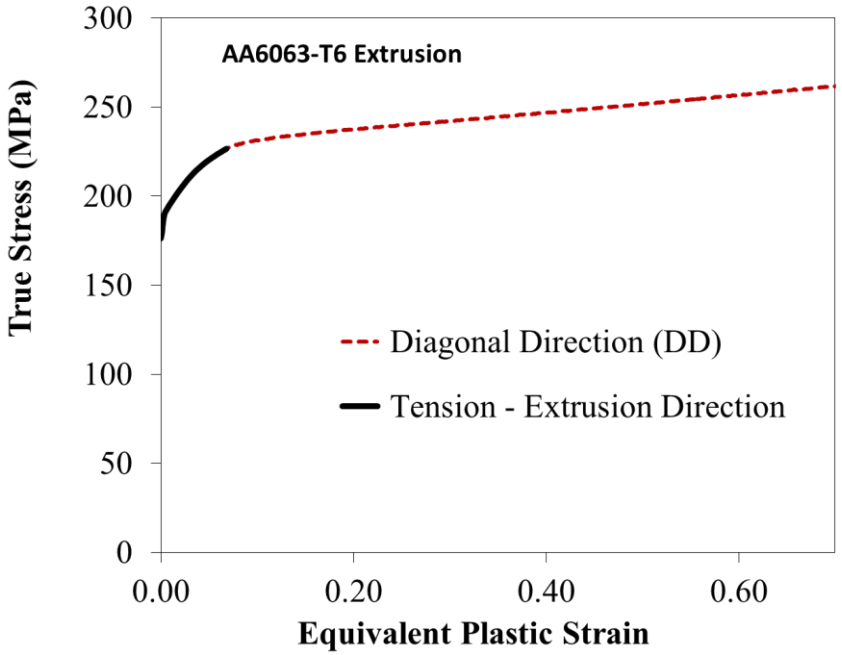

Figure 67 True stress-plastic strain curves obtained from uniaxial tension and simple shear experiments

It is important to note that no yield criterion was assumed in conversion of the shear stress-strain values into true plastic and equivalent plastic strains.

As can be seen from the figure above, true stress-plastic strain curves obtained from the two different experiments have very good agreement. Also the hardening response derived from the shear test extends to much higher plastic strain levels which lends confidence to the large strain hardening model fits. The hardening behaviour of the AA6063-T6 alloy was fit to the generalized Voce constitutive equation given below:

$$\sigma(\varepsilon_{pl}, \beta_{1-4}, \dot{\varepsilon}) = \left[\beta_1 + (\beta_2 + \beta_3 \varepsilon_{pl})(1 - e^{-\beta_4 \varepsilon_{pl}})\right] * (1 + a e^{[b(\dot{\varepsilon}^*)^c]})$$

$$\dot{\varepsilon}^* = ln\left(\frac{\dot{\varepsilon}}{\dot{\varepsilon}_0}\right) \tag{40}$$

$$\dot{\varepsilon}_0 = 0.001 \text{ s}^{-1}$$

Where β_{1-4} are the coefficients governing the hardening behavior and a, b and c are the coefficients governing the strain rate sensitivity. The coefficients of the generalized Voce model are listed in Table 16. The fit was obtained using least squares method with R square value of 0.9993.

Table 16 Generalized Voce model coefficients for AA6063-T6 alloy

Coefficient	$\boldsymbol{\beta_1}$	$\boldsymbol{\beta_2}$	$\boldsymbol{\beta_3}$	$\boldsymbol{\beta_4}$	$\boldsymbol{a}$	$\boldsymbol{b}$	$\boldsymbol{c}$
Value	182.8	44.8	48.6	32.8	0.00224	1.098	0.5066

Figure 68a shows the true stress–equivalent plastic strain curve obtained from the experiments plotted along with the Generalized Voce Model (GVM) fit using the coefficients in Table 16. The GVM captures the experimental stress-strain values rather well. Figure 68b further illustrates how the GVM captures the strain rate sensitivity of the AA6063-T6 alloy compared to the experimental values. The strain rate sensitivity predicted by the GVM is in good agreement with the experimental results obtained from uniaxial tension experiments.

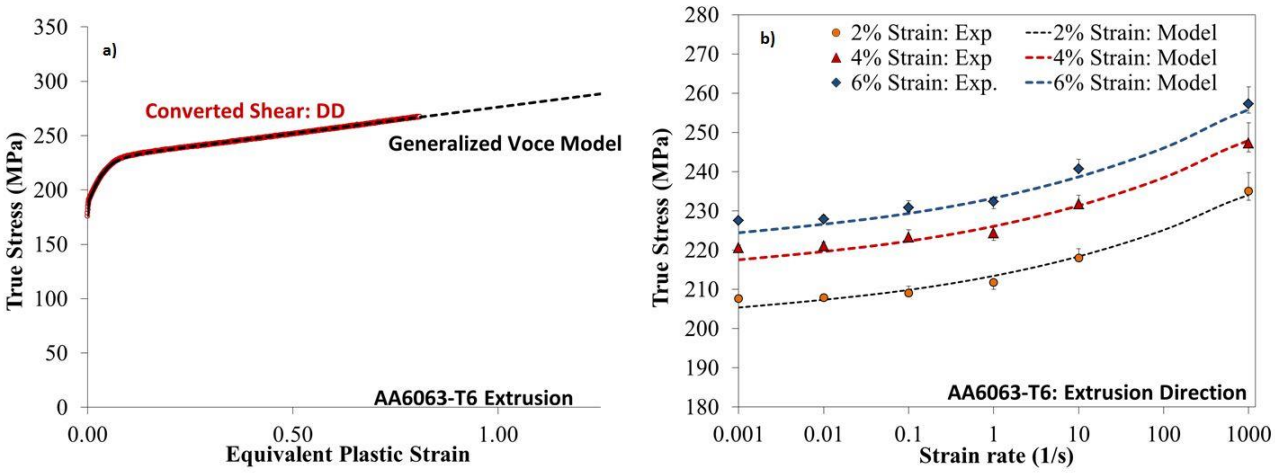

Figure 68 Generalized Voce model a) hardening behaviour b) strain rate sensitivity

4.2 Axial crush simulations

Simulations of the axial crush experiments were performed using the LS-Dyna finite element code. This section outlines the modelling approach, including the material model, boundary conditions and impact loading by the sled. The model predictions are given in Chapter 5 of this thesis.

4.2.1 Aluminum rail model

The aluminum rails are modeled using the Barlat-2000 constitutive model (*MAT_133) fit to the measured material response, as described Section 4.1, above. Shell elements with 7 integration points were adopted to describe the deformable extrusion material. Fully integrated shell elements with 4 quadrature points are employed in the models. A shell element formulation was adopted to better mimic current industrial CAE crash simulation practice in which shell elements are often mandated (as opposed to brick elements) for computational efficiency.

The aluminum rails were split into different parts to ease the material axis assignment. Figure 69 illustrates the meshes for the Omega and UWR4 rails divided into sections. The extruded rails had varying wall thicknesses as a result of the profile topography optimization. The wall thicknesses assigned to the sections in the model are given in Table 17.

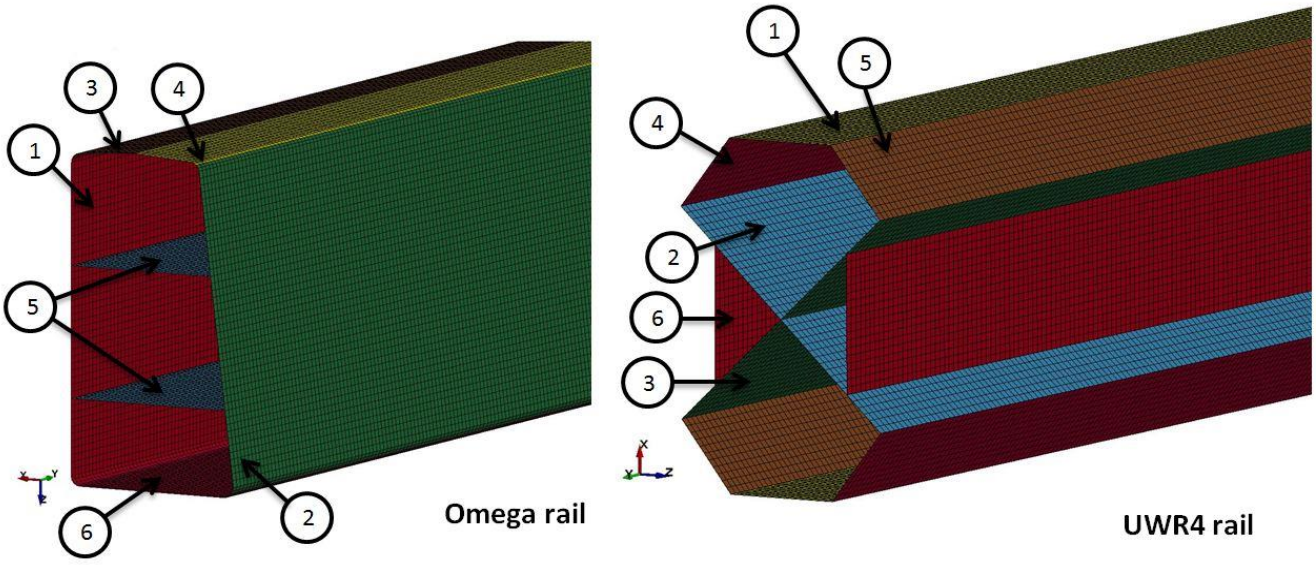

Figure 69 Omega & UWR4 rail mesh broken into sections

Table 17 Profile shell thicknesses in crash modeling

Omega Profile						
Section	1	2	3	4	5	6
Shell Thickness [mm]	1.87	2.0	2.04	1.94	1.94	1.98
UWR4 Profile						
Section	1	2	3	4	5	6
Shell Thickness [mm]	1.79	2.01	2.01	1.81	1.84	1.83

4.2.2 Fracture criterion

A Generalized Incremental Stress-Strain Model (GISSMO) was adopted to model the fracture behaviour of the AA6063-T6 aluminum alloy. The experimental work and calibration of the failure criteria was performed by Nemcko *et al.* and given in more detail in [52]. Figure 70 illustrates the results of the fracture characterization work. As can be seen from Figure 70, the fracture behaviour of the AA6063-T6 extrusion is strongly dependent on the loading direction. The extrusion direction has the lowest fracture curve under compression dominated loading modes. For the equal-biaxial loading mode, failure occurs in a manner in which the maximum

principle strain is applied in the transverse direction. As a result, the transverse direction is the limiting direction for the biaxial condition. Furthermore, the diagonal direction exhibits the lowest failure strain in uniaxial tension.

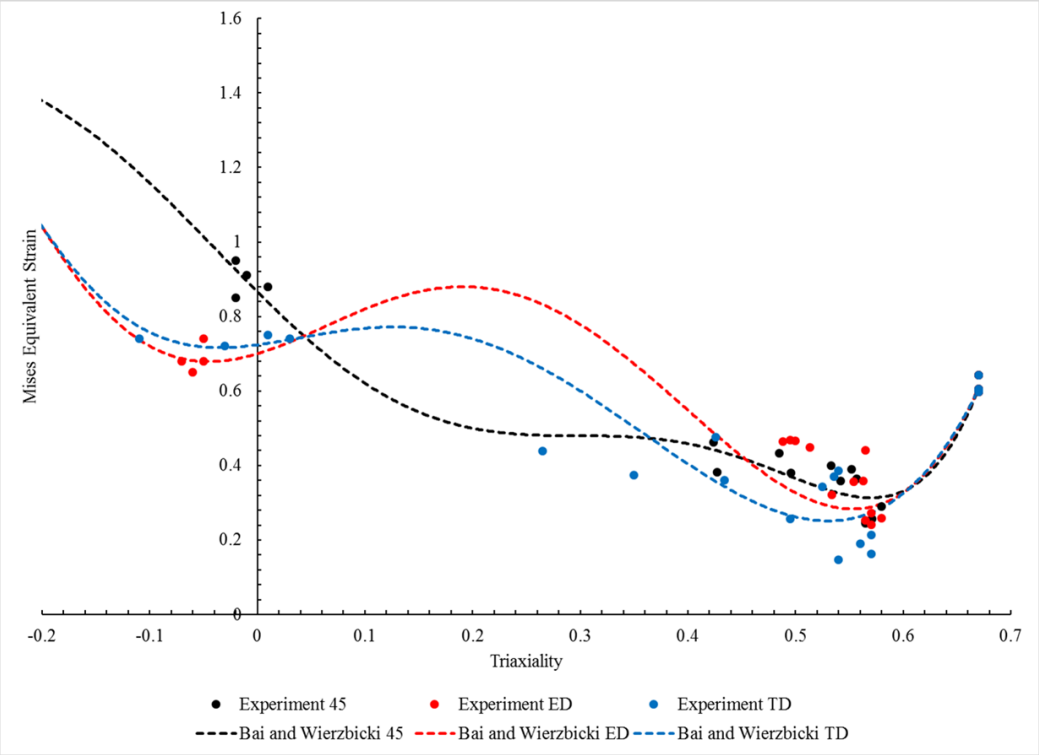

Figure 70 Experimental GISSMO curve [52]

Four sample geometries covering a wide range of stress states are tested in order to obtain experimental points for calibration of the fracture model [52]. The samples investigated included mini shear, hole tension, regular notch and plain strain notch geometries shown in Figure 71.

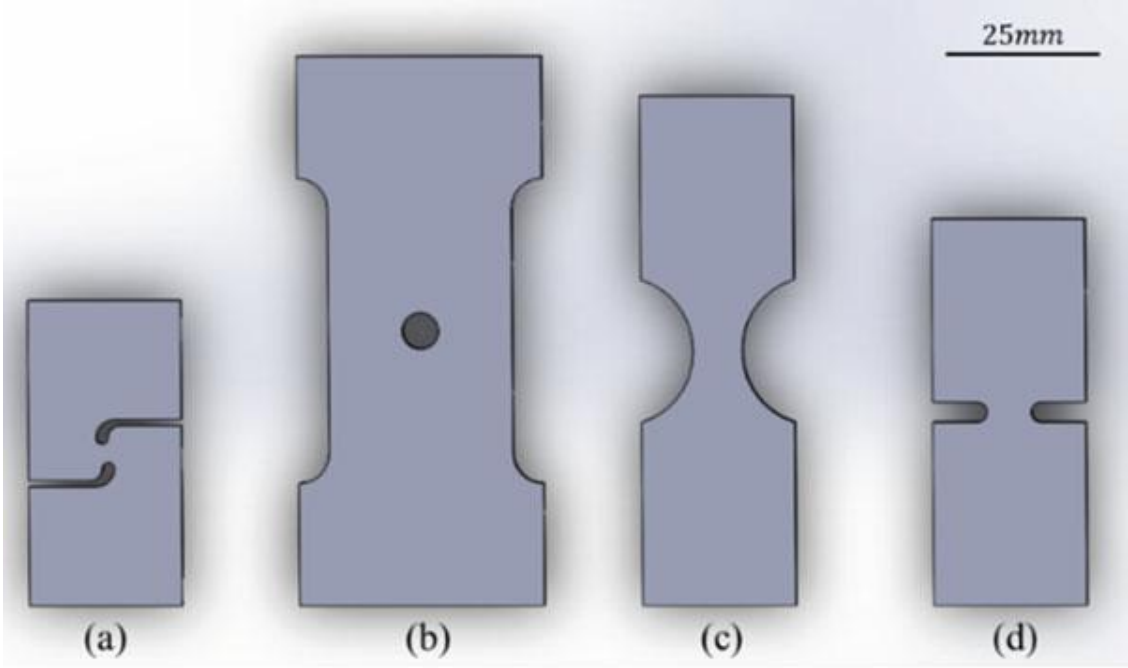

Figure 71 Sample geometries (a) mini shear, (b) hole tension, (c) regular notch, (d) plane strain notch [52]

As a first cut into fracture characterization, the local equivalent strains at failure were calculated assuming a Mises material.

A VSGL (Section 2.5) of 0.3 mm was used for all calculations of strain obtained from the DIC analysis. Hence, mesh regularization on the MJIS samples tested in the extrusion direction was employed to account for larger mesh sizes utilized in the numerical modeling of axial crush events. The resulting mesh regularization curve is shown in Figure 72 [54].

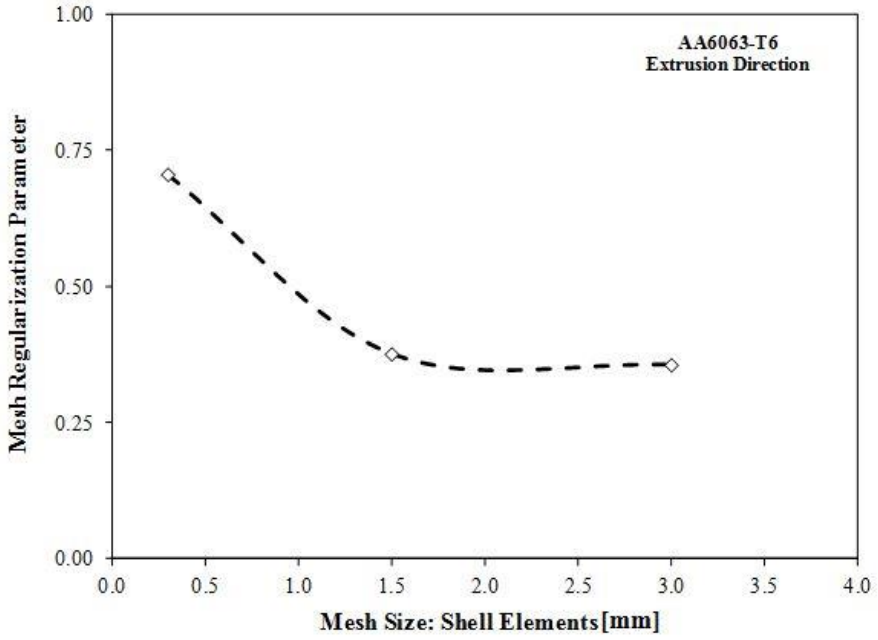

Figure 72 Mesh regularization curve [54]

4.2.3 Mounting fixtures

The clamps and bosses used for mounting the rails during axial crush experiments are modeled using rigid, non-deformable materials with properties of steel. The elastic properties are shown in Table 18 and are used primarily in the contact algorithm. The tools were modeled using a combination of brick and tetrahedron elements with mesh size of 5 mm.

Table 18 Steel elastic constants for rigid material model

Density	7.93 g/cm^3
Young's Modulus	207 GPa
Poisson's	0.3

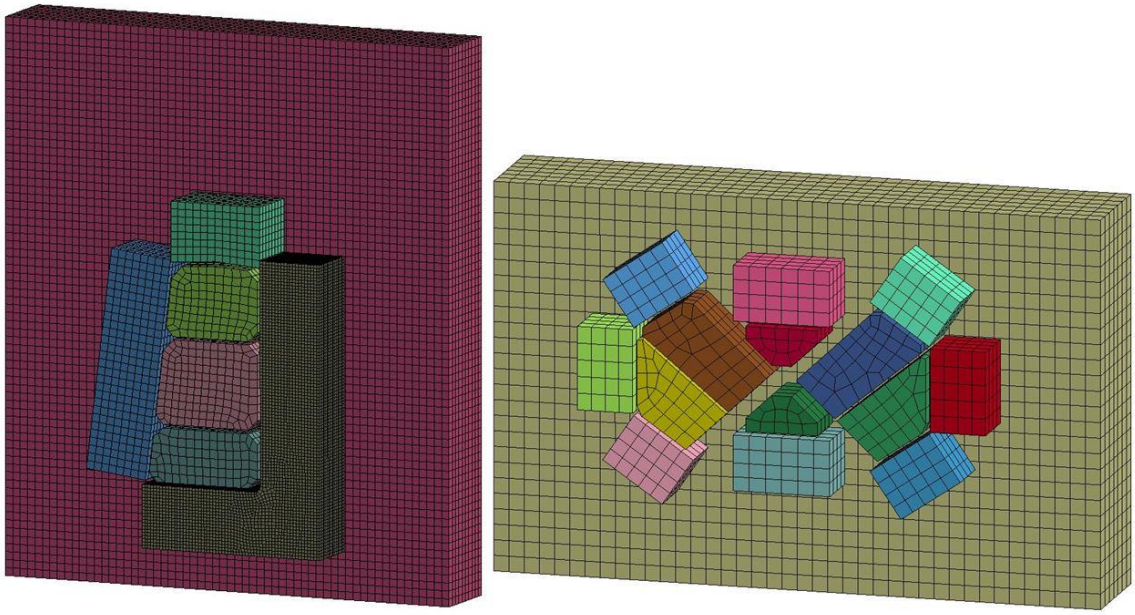

Figure 73 Omega and UWR4 fixture mesh

The bosses and clamps were constrained in all displacement degrees of freedom and the deformable shell elements were rigidly tied to the clamps in regions of contact. This approach was adopted to model the clamping boundary condition in the experiments.

4.2.4 The crash sled

The sled is modeled using rigid, non-deformable shell elements with the elastic constants of steel (Table 18) assigned for contact treatment. For simplicity, the sled is meshed as a wall of shell elements representing the impact face. The sled is assigned a lumped mass of 1141 kg and initial axial velocity of 7.8 m/s to reflect the experimental conditions. The initial velocity and the mass properties for the sled are assigned using *PART_INERTIA card. All the degrees of freedom for the sled are fixed except for the translation in the axial direction of the rail. Figure 74 illustrates the axial crush model setup.

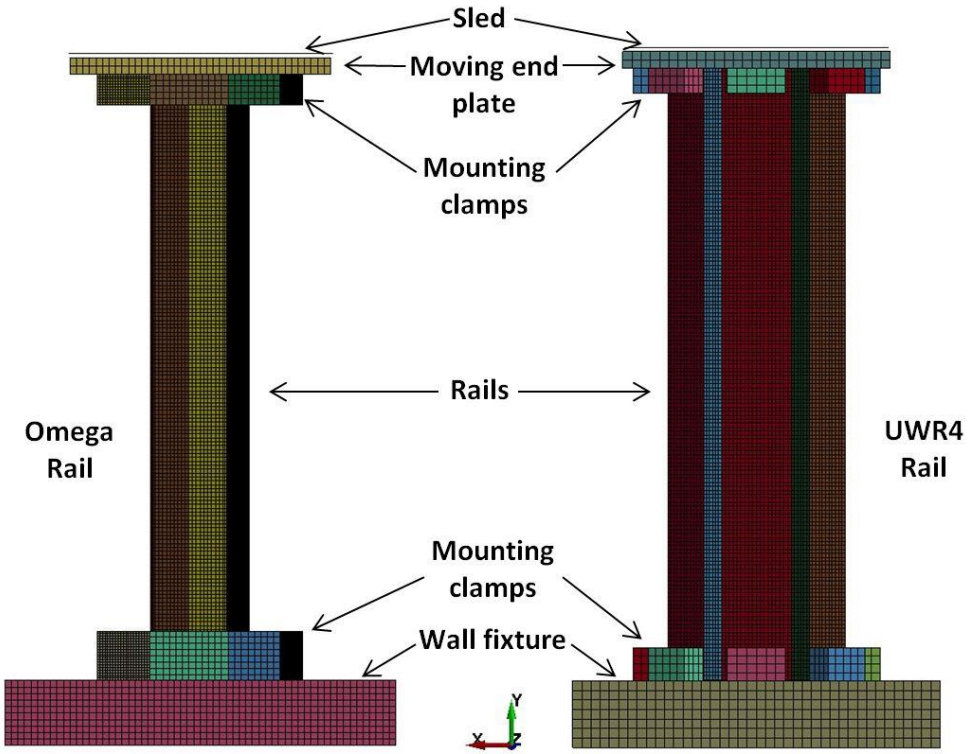

Figure 74 Axial crush model setup

4.2.5 Boundary conditions – dynamic axial crush

The same boundary conditions are employed for modeling axial crush of both the Omega and UWR4 cross-sections. The lateral movement of the rails is constrained by the use of the clamps and fixtures. The fixtures used to mount the rail to the fixed wall are constrained in all degrees of freedom. The fixtures at the sled end are allowed to move in the axial direction only and are constrained to the movement of the sled impact face by the use of the *CONSTRAINED_RIGID_BODIES card. Penalty based surface-to-surface contacts are used between contacting surfaces of the tooling and rails as well as between the tooling and impactor sled. An automatic single-surface contact formulation is used to model the self-contact between the fold regions of the aluminum rails. The friction coefficients in the contact definitions are given in the Table 19. High values of friction were imposed under the assumption that minimal sliding would occur [72].

Table 19 Coefficients of friction employed in the LS-Dyna models

	Static	Dynamic
Fixture-rail	0.61	0.47
Rail-rail	1.05	1.0

4.2.6 Boundary conditions – quasi-static axial crush

The quasi-static axial crush models employ same the boundary conditions as dynamic crush models with a few exceptions. The quasi-static experiment takes too long to model in real time using an explicit dynamic formulation; hence, time scaling is used to reduce the simulation time. A parametric study is performed to observe the effect of the time scaling on the predicted average load of the AA6063-T6 Omega rails. Time scales of 10,000, 7,500, 5,000, 2,500 and 1000 are chosen for the parametric study. The velocity of the hydraulic ram is set 0.508 mm/sec to reflect the hydraulic ram speed during the experiment. The velocity of the hydraulic ram is scaled by a factors mentioned above. The strain rate sensitivity table is scaled by corresponding scale factors in order to compensate the offset created by increased velocity.

5 Modeling results

This section presents the results of the modeling approach taken to simulate the axial crush experiments on the AA6063-T6 Omega and UWR4 rails. The predictions are compared with measured results obtained from the axial crush experiments. Two simulation approaches were taken: the first considers axial crush without a fracture criterion, while the second includes the GISSMO fracture criterion presented in Section 4.2.2.

5.1 Omega profile axial crush model results

This section describes the results of the numerical modeling of the axial crush on the AA6063 Omega rails. Figure 75 illustrates an image of an Omega rail under dynamic axial impact at various crush distances.

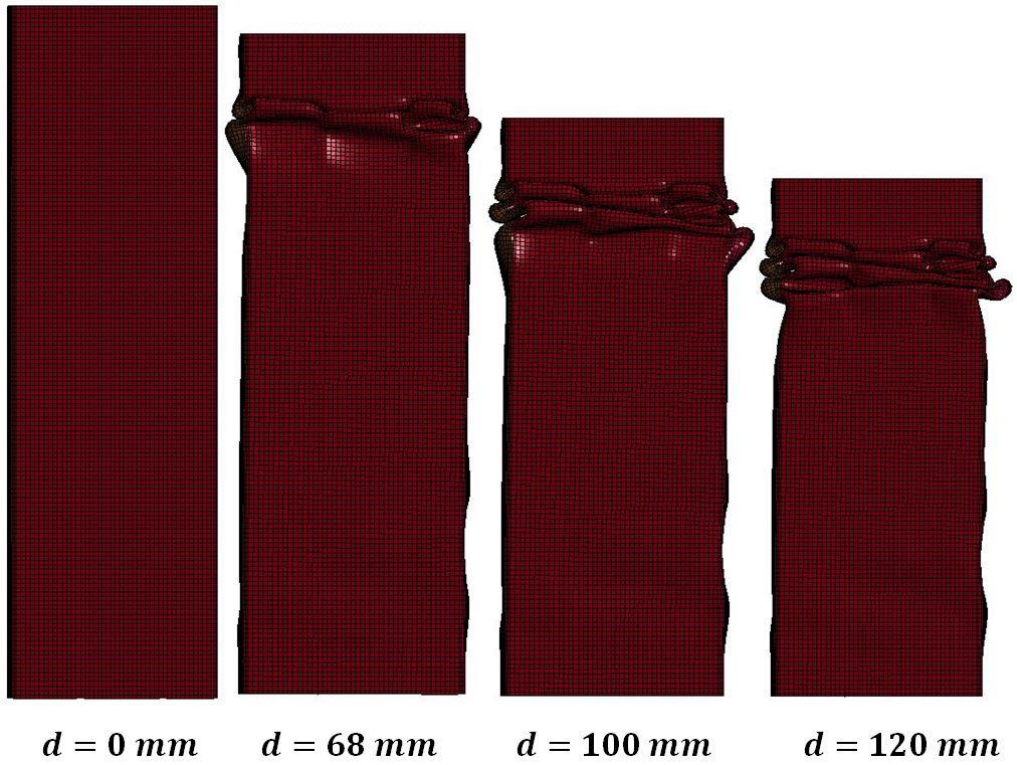

Figure 75 Progressive folding of Omega rail (dynamic prediction) at various crush distances

The crush distance of the numerical predictions is obtained from node displacement on the impact end of the rail. The load exerted by the rail on wall is extracted from the contact forces between the rail and wall mount.

Figure 76 compares the fracture locations on the Omega rails crushed dynamically to those of the numerical prediction using the GISSMO fracture criterion. As can be seen, the locations of the fracture in the numerical prediction closely correlate to the fracture observed experimentally.

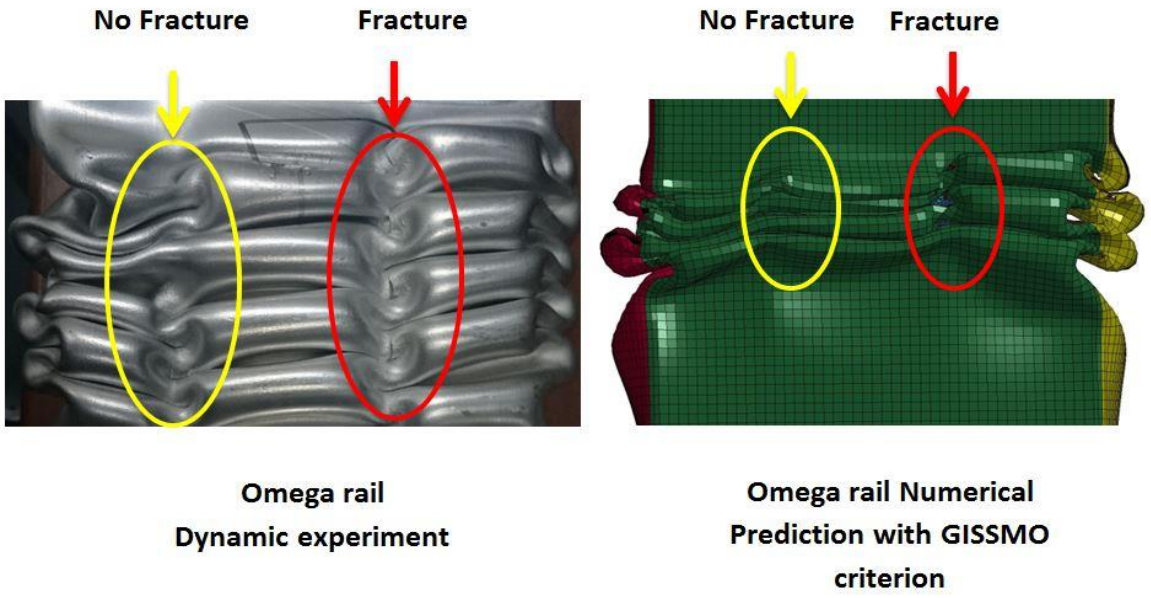

Figure 76 Omega rails crushed dynamically: Experiment vs Numerical prediction

5.1.1 Dynamic axial crush

Figure 77 shows the predicted and measured force-displacement curves for the AA6063-T6 Omega dynamic axial crush experiments. The notable difference between the experimental and simulated curves can be seen in the peak loads required to initiate the first fold, with the model predicted a lower peak load. The average measured crush load for the dynamic axial crush of the Omega rail is 93.6 kN (Figure 60) compared to the model predictions of 87.4 kN without failure and 86.6 kN when GISSMO fracture model is included. The relatively modest effect of the fracture model is consistent with the limited extent of cracking observed in the AA6063-T6 Omega rails (Figure 76)

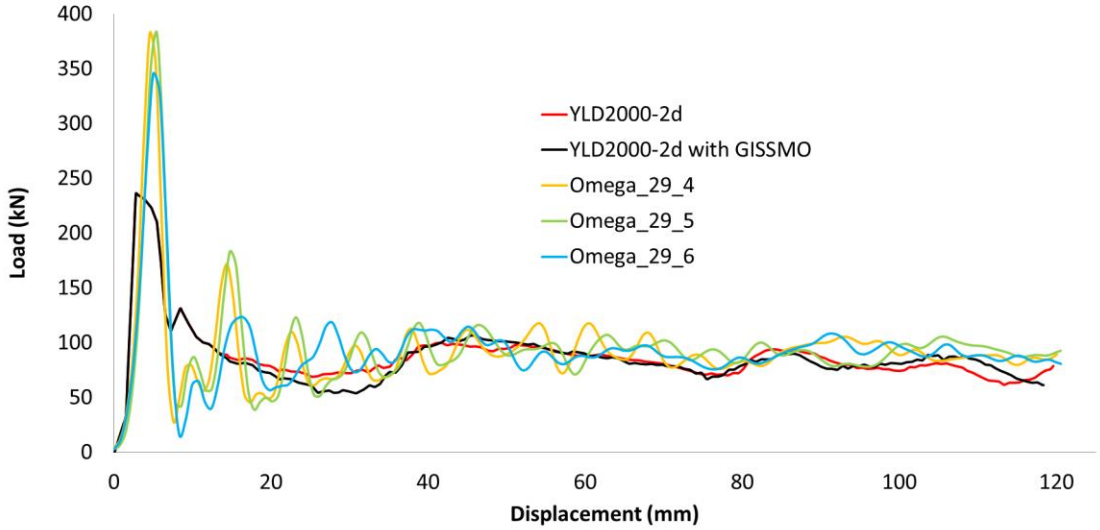

Figure 77 Predicted load-displacement curves for dynamic axial crush of Omega rails

The energy absorbed vs displacement curves are shown in Figure 78. The predicted absorbed energy is initially close to the measured data, but starts to deviate after approximately 70 mm of axial crush. The measured absorbed energy at 120 mm of crush are 11.3 kJ compared to 10.5 kJ and 10.4 kJ from the models without fracture and with fracture, respectively, an error of 7-8%.

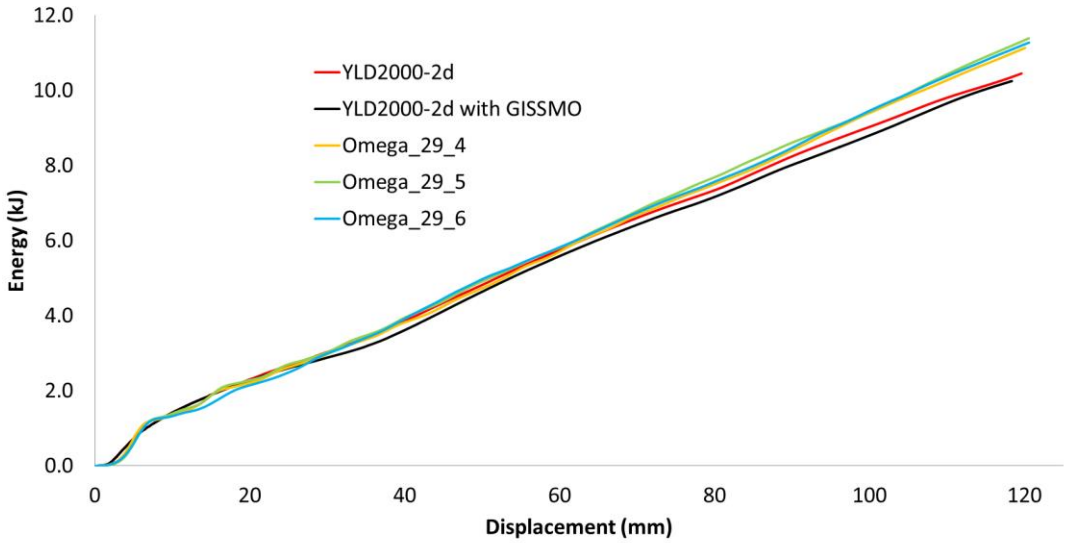

Figure 78 Predicted energy-displacement curves for dynamic axial crush of Omega rails

5.1.2 Quasi-static axial crush

As was described in section 4.2.6, as a first step, a parametric study of dependence of the average crush loads on the time scaling is performed. Figure 79 shows the error convergence *vs.* the time scale factor for the quasi-static numerical predictions, from which it is observed that the error becomes small (<1.5%) at a time scale factor of 2,500. Numerical predictions performed at a time scale factor of 2,500 and 1,000 resulted in 1.1% and 1% respectively.

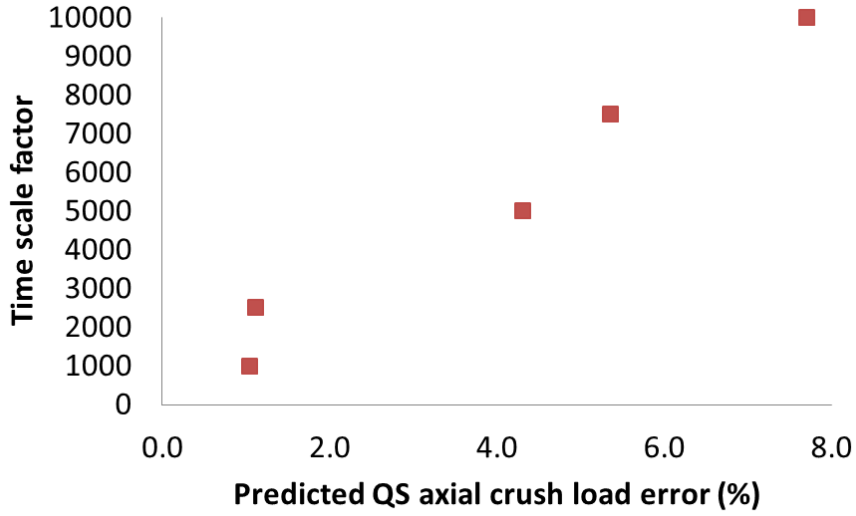

Figure 79 Time scale factor vs. average crush load error convergence

Figure 80 shows CPU run time *vs* time scale factor. The CPU run time for the numerical predictions performed at time scale factors of 2,500 and 1,000 were 176.5 and 573.2 hours respectively. Hence, the rest of the quasi-static numerical predictions are performed at the time scaling factor of 2,500.

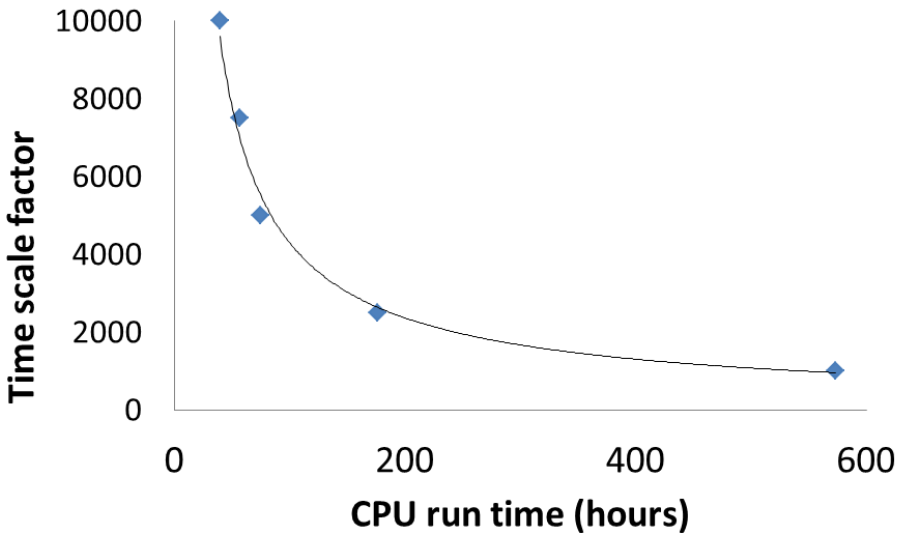

Figure 80 CPU run time vs. time scale factor

The quasi-static axial crush of the baseline profile rails resulted in lower peak and average loads. Figure 81 shows the load-displacement curves from the YLD2000-2d model with and without the GISSMO fracture model along with the experimental results. The models over-predicted peak load to initiate folding, suggesting that the model is not exhibiting the level of inertial effect as in the experiment. This may be due to the "time scaling" of the model (see Section 4.2.6) invoked to shorten the run times using an explicit dynamic formulation to simulate a static event. After folding initiates, the oscillatory response of the model aligns well with the experimental data and fracture has a small effect in reducing the crush load.

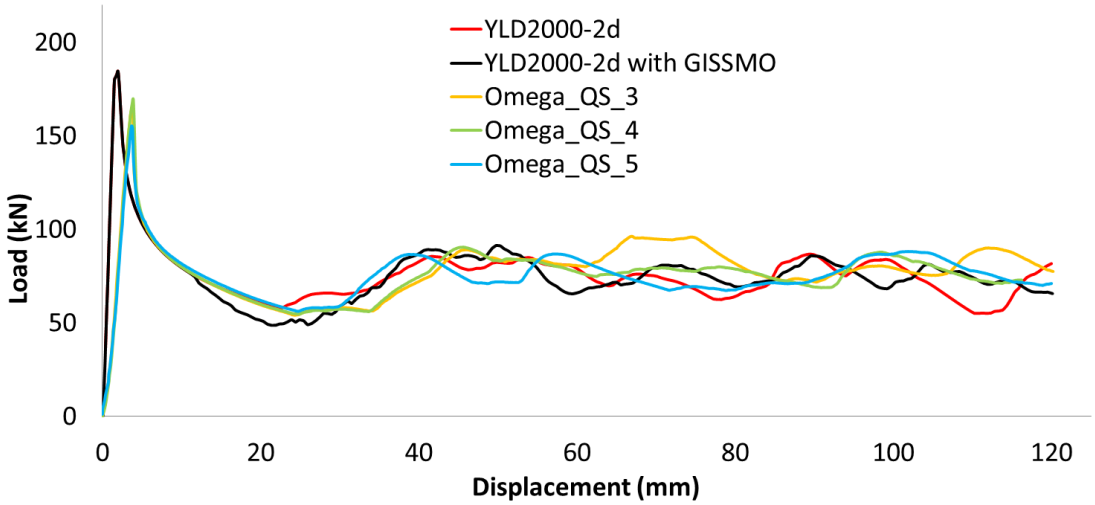

Figure 81 Predicted load-displacement curves for quasi-static axial crush of Omega rails

The absorbed energy for the quasi-static axial crush (Figure 82) shows very good agreement between the measured and predicted behaviour which is less than that of the dynamic axial crush.

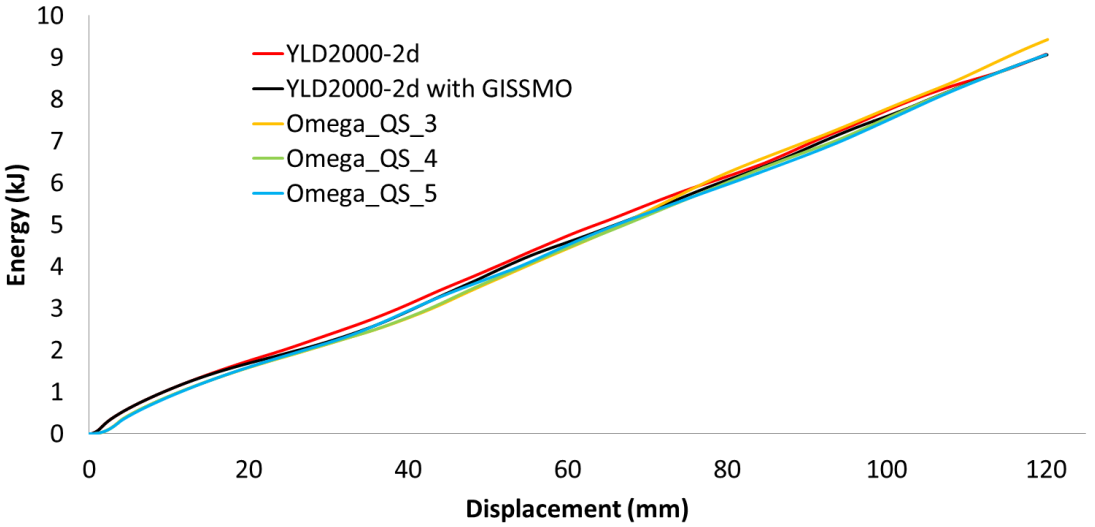

Figure 82 Predicted energy-displacement curves for quasi-static axial crush of Omega rails

Figure 83 provides a summary of the average loads obtained from the numerical modeling and experiments on the axial crush of the Omega profile rails. In general, the predicted average

load without fracture was within 6.6% of the experimental value. The average load predicted with the GISSMO fracture criterion included in the model was slightly lower and within 7.4% of the experimental observation. The predicted average load for the quasi-static experiments was lower than for the dynamic experiments, in general accord with the trends in the experiments, although a larger drop was seen in the experiments.

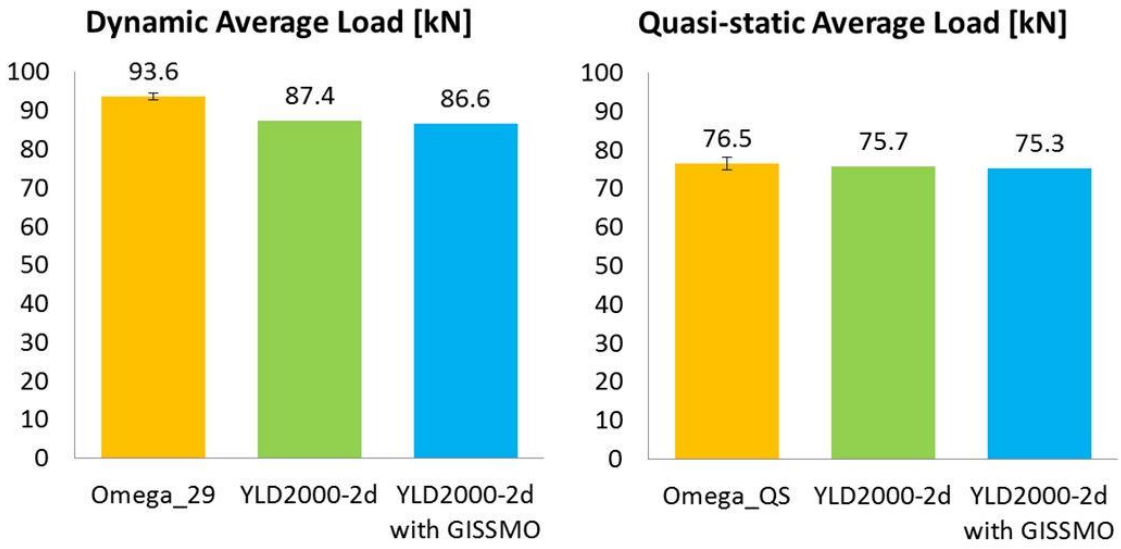

Figure 83 Omega axial crush: summary of model predictions and experiments – average loads

Figure 84 summarizes the peak loads obtained from the modeling of the axial crush in quasi-static and dynamic crush modes compared to that of the experiments. The peak load required to initiate folding of the rail in dynamic axial crush is considerably higher than the peak loads predicted by the models with and without fracture models. The peak loads from the two modeling approaches are the same. The peak load predictions for the quasi-static axial crush are higher than that of the experiments. As in the dynamic crush models, the peak loads of the quasi-static models with and without fracture criterion are equal.

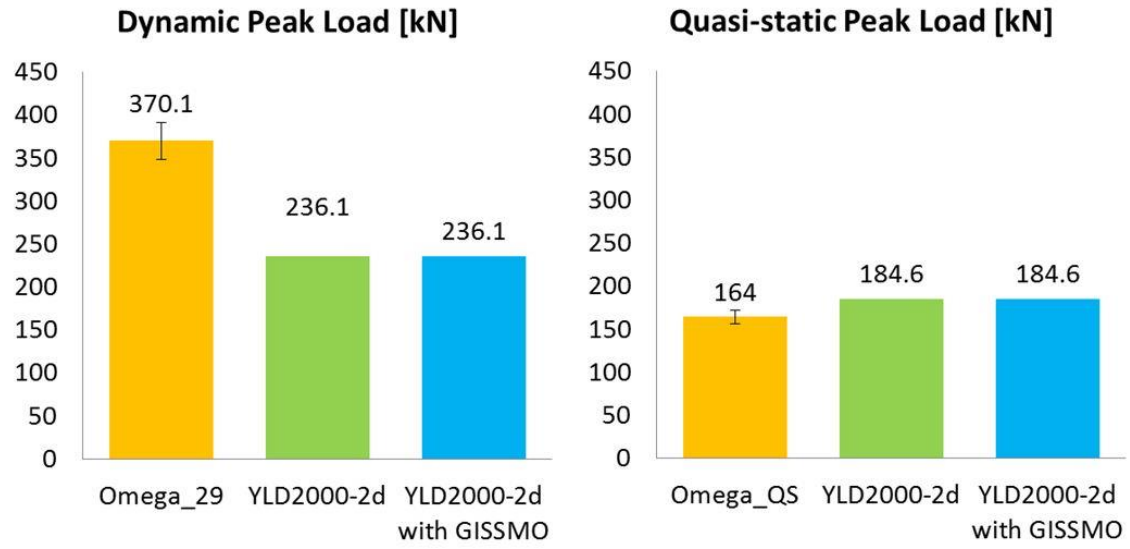

Figure 84 Omega axial crush: summary of model predictions and experiments – Peak loads

Figure 85 summarizes the energies absorbed for 120 mm of crush displacement for the Omega profile rails during the dynamic and quasi-static axial crush experiments, as well as the corresponding predictions. The dynamic predictions of absorbed energy were within 8% of the measured data whereas the error in the quasi-static models was within 1%.

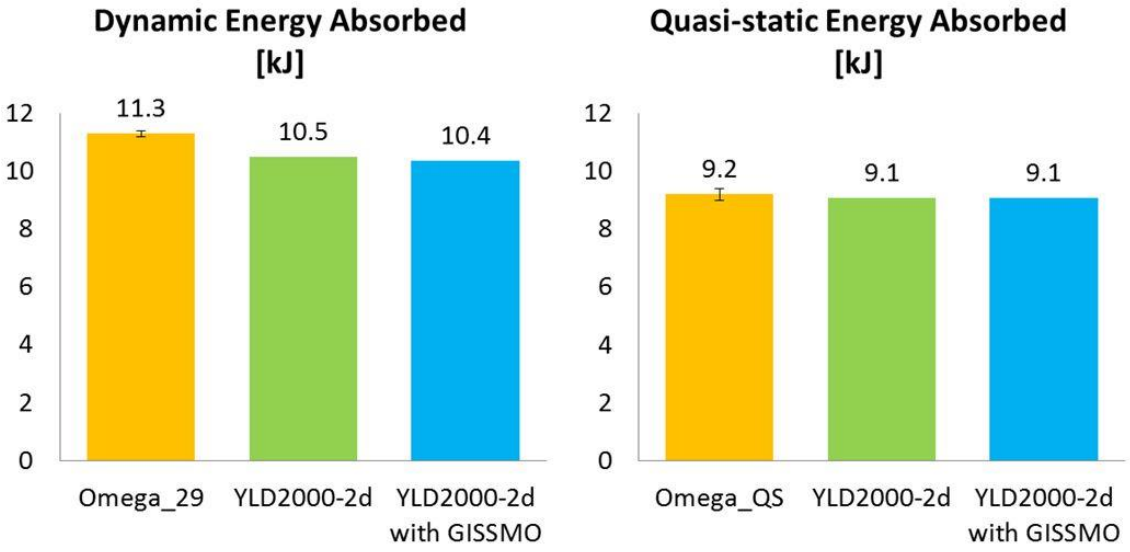

Figure 85 Omega axial crush: summary of model predictions and experiments – Absorbed energy

5.2 UWR4 profile axial crush model results

This section describes the results of the numerical modeling of the axial crush on the AA6063 UWR4 rails. Figure 86 illustrates an image of a UWR4 rails under dynamic axial impact at various crush distances.

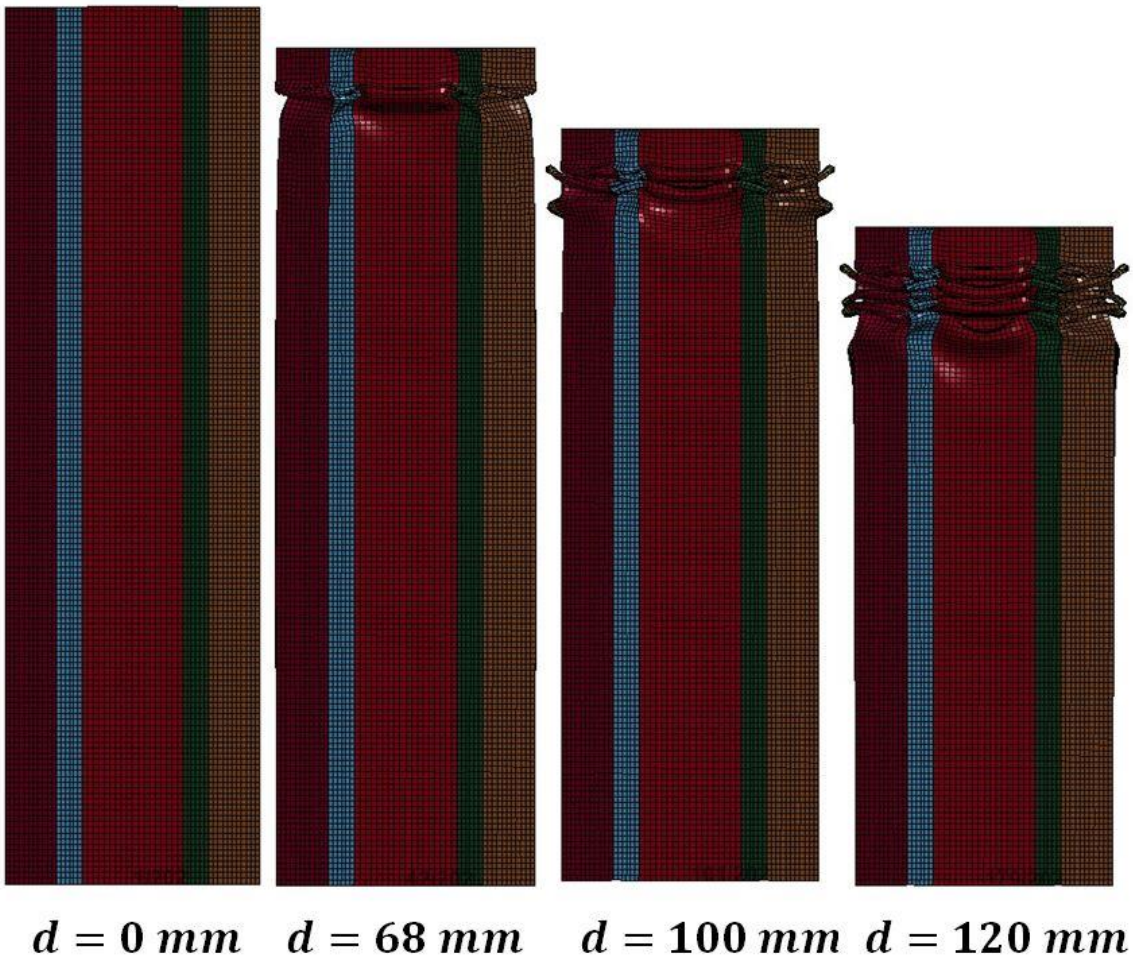

Figure 86 Progressive folding of UWR4 rail (dynamic prediction) at various crush distances

Resulting displacements and loads from the numerical prediction of the UWR4 rails are obtained in a similar manner to Omega rails. Figure 87 compares the fracture locations on UWR4 rails, crushed dynamically, against the corresponding numerical prediction. As can be seen from the image above, the locations of the fracture in the numerical model have a close correlation with those found on rails crushed experimentally. The fracture criterion used in numerical predictions predicts the onset of fracture very well. However, prediction of fracture propagation is typically more challenging and sensitive to numerical artefacts such as mesh sensitivity and unzipping

which may account for the differences in extent of fracture in the numerical models versus experiment.

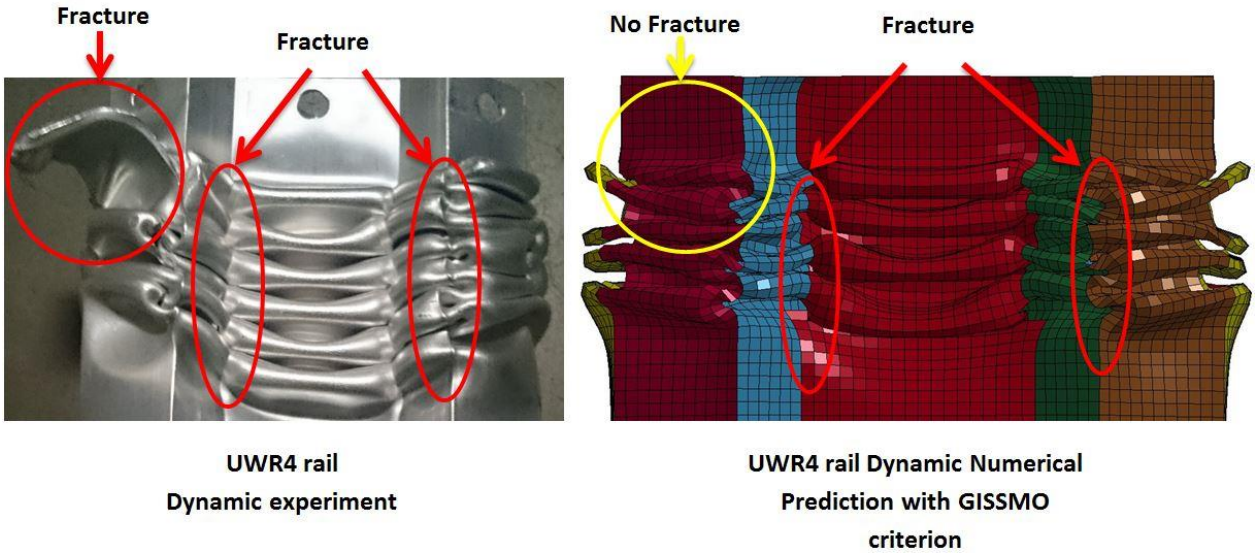

Figure 87 UWR4 rails crushed dynamically: Experiment vs Numerical prediction

Figure 88 compares the fracture locations on UWR4 rails, crushed quasi-statically, against the corresponding numerical prediction. Similar to the dynamic axial crush predictions, the numerical prediction of the quasi-static axial crush of the UWR4 rails closely predicted the fracture locations. Similarly, the extent of fracture is not predicted very well.

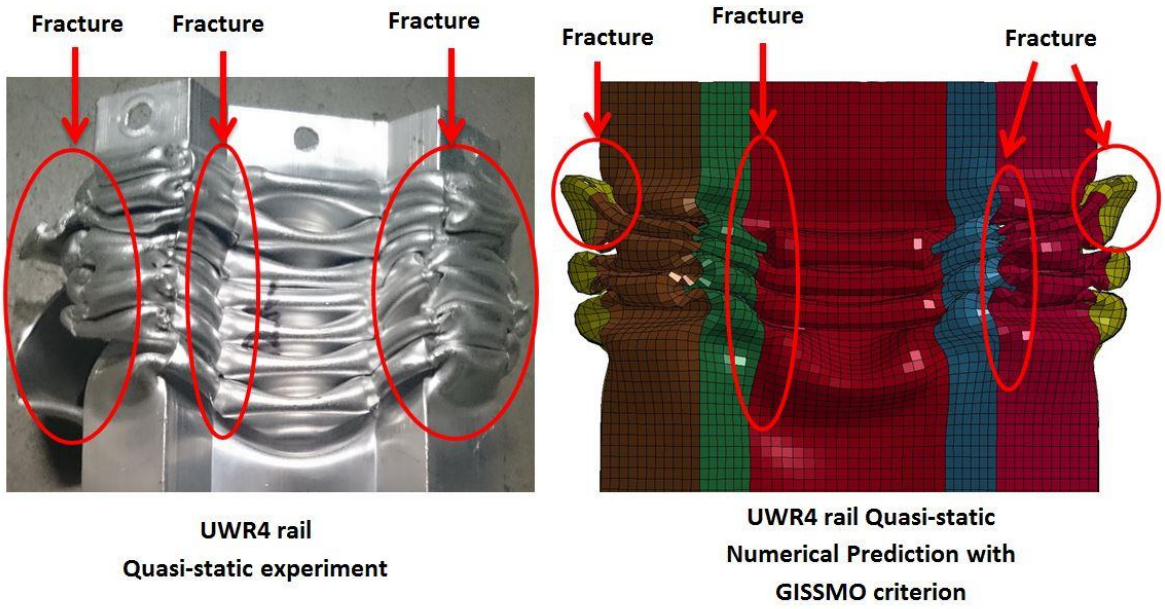

Figure 88 UWR4 rails crushed quasi-statically: Experiment vs Numerical prediction

5.2.1 Dynamic axial crush

Figure 89 illustrates predicted and measured force-displacement curves for AA6063 UWR4 dynamic axial crush. The predicted force displacement curve follows the experimental curve closely. As in the case with the Omega profile rails, the peak forces required to initiate the folding in the rails have a notable difference, with the model predicted lower peak force. The average measured load for the dynamic axial crush of the UWR4 rail is 123.8 kN (Figure 60) compared to the model predictions of 123.8 kN without failure and 112.9 kN when GISSMO fracture model is included. A greater extent of the fracture in UWR4 (Figure 87) model has a larger impact on the average load compared to that of the Omega rail.

Figure 90 illustrates the predicted absorbed energy *vs* displacement curves for the dynamic axial crush of the UWR4 profile rails plotted against the energy absorbed curves obtained experimentally. The predicted energy absorbed lies within the experimental variability.

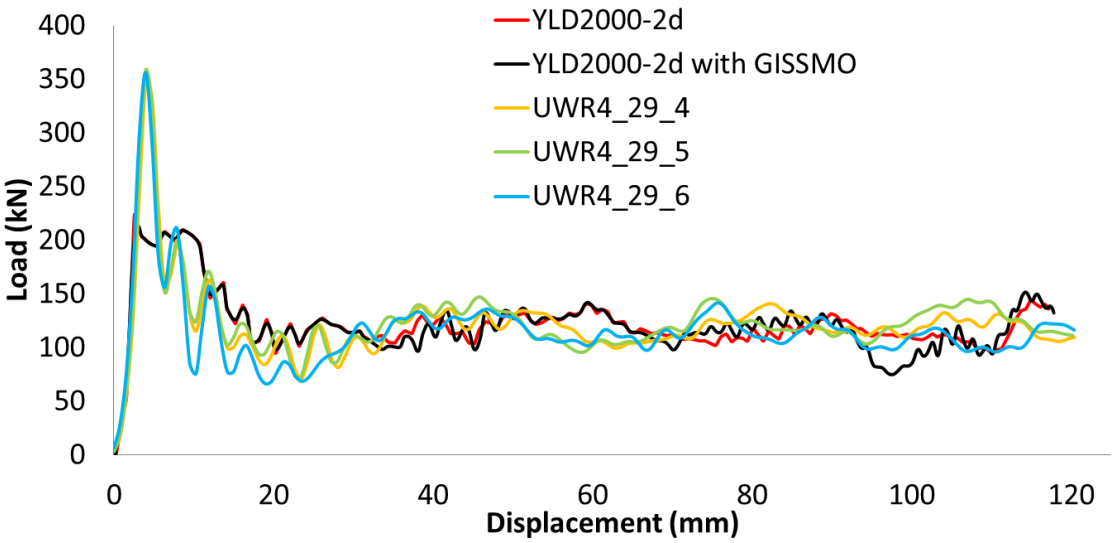

Figure 89 Predicted load-displacement curves for dynamic axial crush of UWR4 rails

The energy absorbed vs displacement curves are shown in Figure 90. The predicted absorbed energy is in a great agreement with the experimental values. The measured absorbed energy at 120 mm of crush are 14.6 kJ compared to 14.9 kJ and 14.7 kJ from the models without fracture and with fracture, respectively.

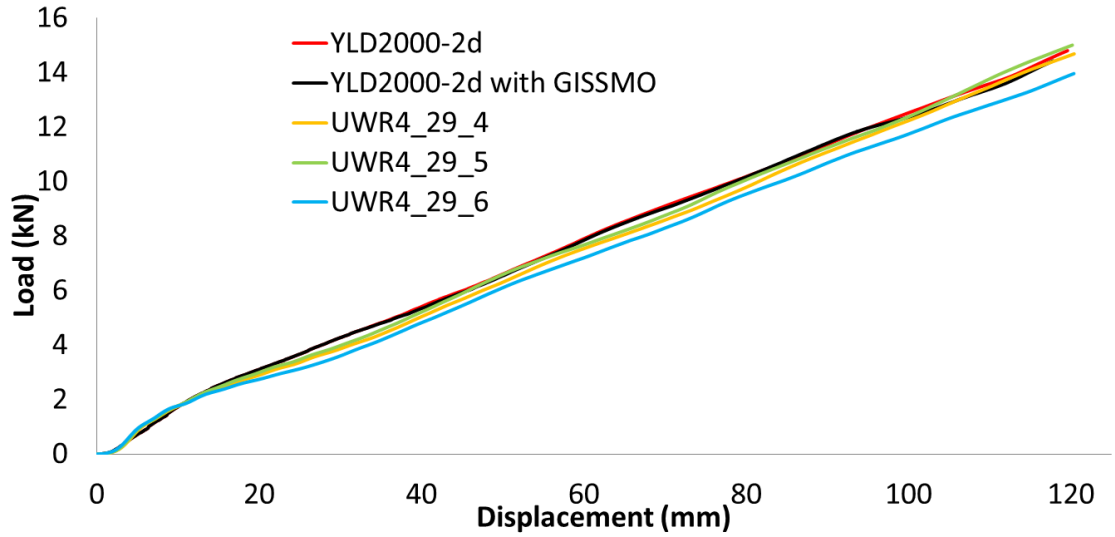

Figure 90 Predicetd energy-displacement curves for dynamic axial crush of UWR4 rails

5.2.2 Quasi-static axial crush

The quasi-static axial crush of the UWR4 profile rails resulted in higher peak and average loads. Figure 91 shows the load-displacement curves from the YLD2000-2d model with and without the GISSMO fracture model along with the experimental results. The models are in good agreement with experimental peak load to initiate folding. After folding initiates, the oscillatory response of the model aligns well with the experimental data. Fracture has a small effect in reducing the average load which is similar to the prediction of the Omega rail.

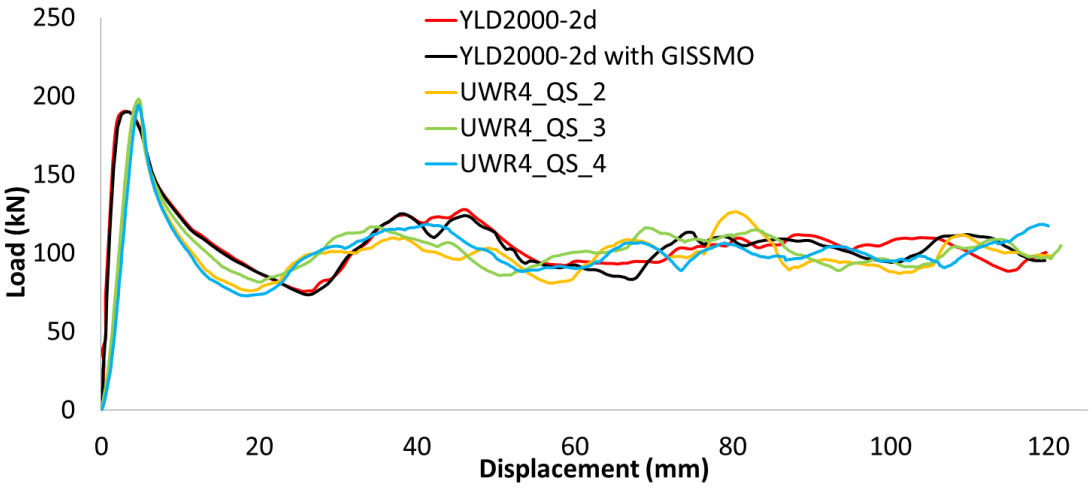

Figure 91 Predicted load-displacement curves for quasi-static axial crush of UWR4 rails

The absorbed energy of the quasi-static numerical predictions overestimates the experimental values as shown in Figure 92. As expected from the average loads, fracture has a small effect on the absorbed energy.

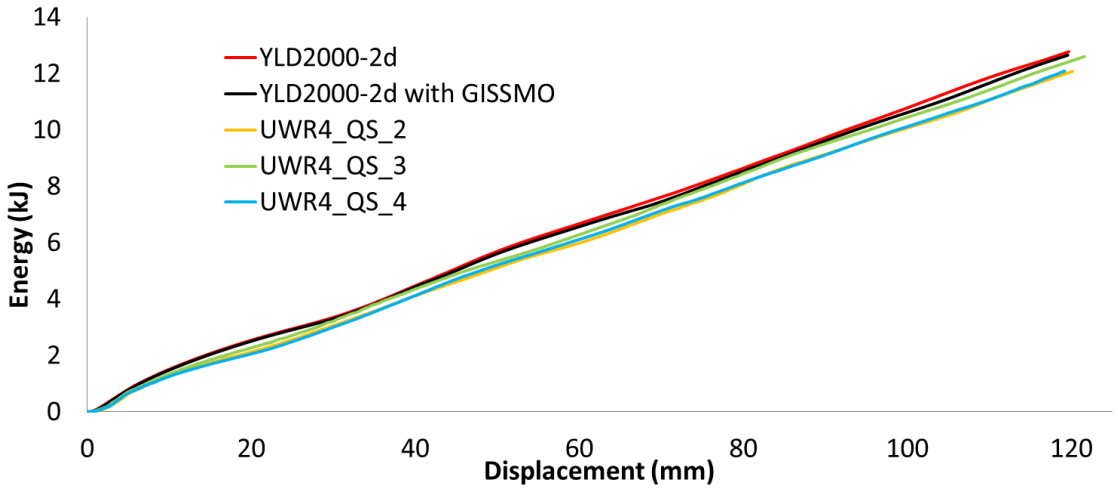

Figure 92 Predicted energy-displacement curves for quasi-static axial crush of UWR4 rails

Figure 93-Figure 95 summarize the numerical predictions of dynamic and quasi-static axial crush experiments for UWR4 profile rails.

Figure 93 provides a summary of the average loads obtained from experiments as well as numerical predictions of the UWR4 profile. In general, numerical models overestimate the experimental average crush load by 2.3% when the fracture criterion is implemented and by 3.4% when fracture is not included for dynamic crush. The quasi-static predictions have a larger discrepancy compared to the dynamic prediction. The error is 5-6% (overestimated).

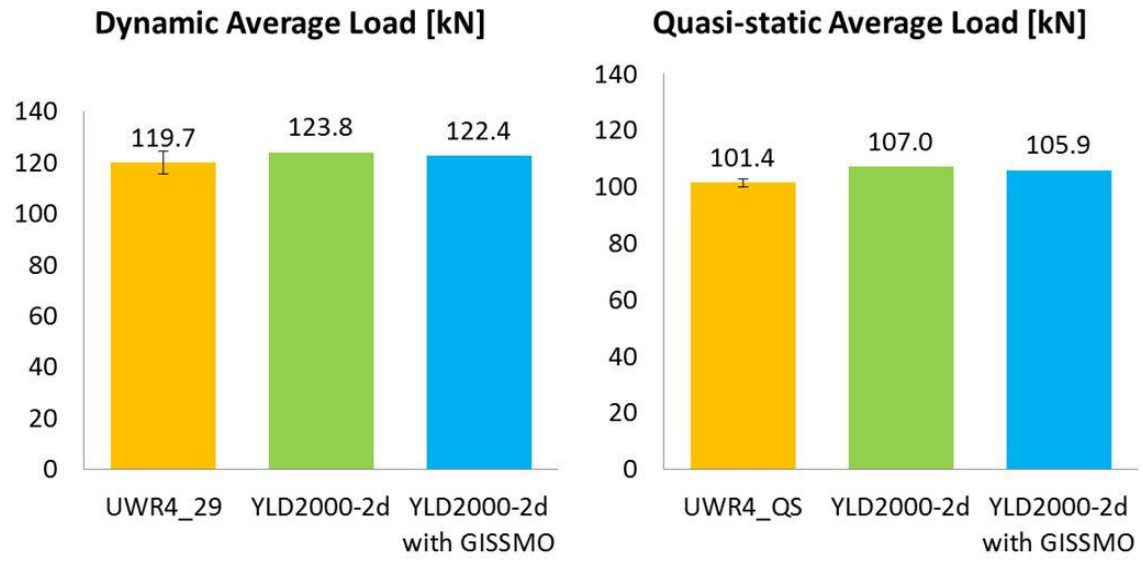

Figure 93 UWR4 axial crush: summary of model predictions and experiments – Average loads

Figure 94 summarizes the peak loads obtained from the experiments and numerical models of the axial crush of the UWR4 profile. The peak loads from the dynamic experiments are considerably higher than those of the numerical predictions. The peak loads of the quasi-static predictions are in a good agreement with the experimental value. In this case, both approaches resulted in a same peak load value.

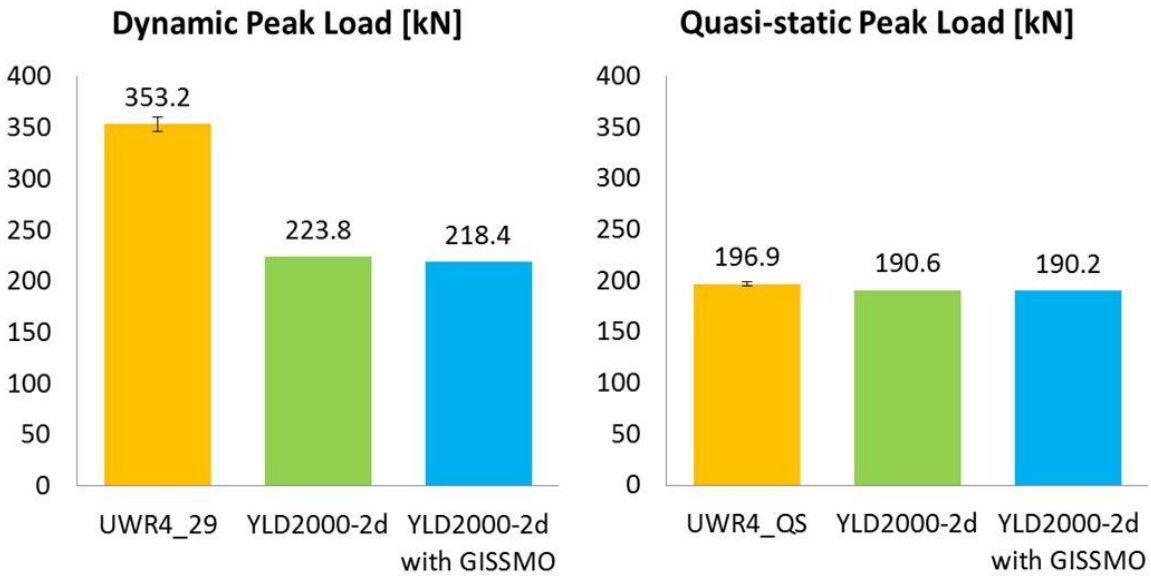

Figure 94 UWR4 axial crush: summary of model predictions and experiments – Peak loads

Figure 95 shows summary of energies absorbed by axial crush of the 120 mm of UWR4 profile rail during dynamic and quasi-static axial crush experiments, as well as the models with and without GISSMO fracture criterion. As expected from the average loads, the energy absorption predictions of the UWR4 rails in dynamic crush are in excellent agreement with experimental values. Quasi-static models overestimate the experimental values by 4.1% and 4.9% with and without fracture criterion.

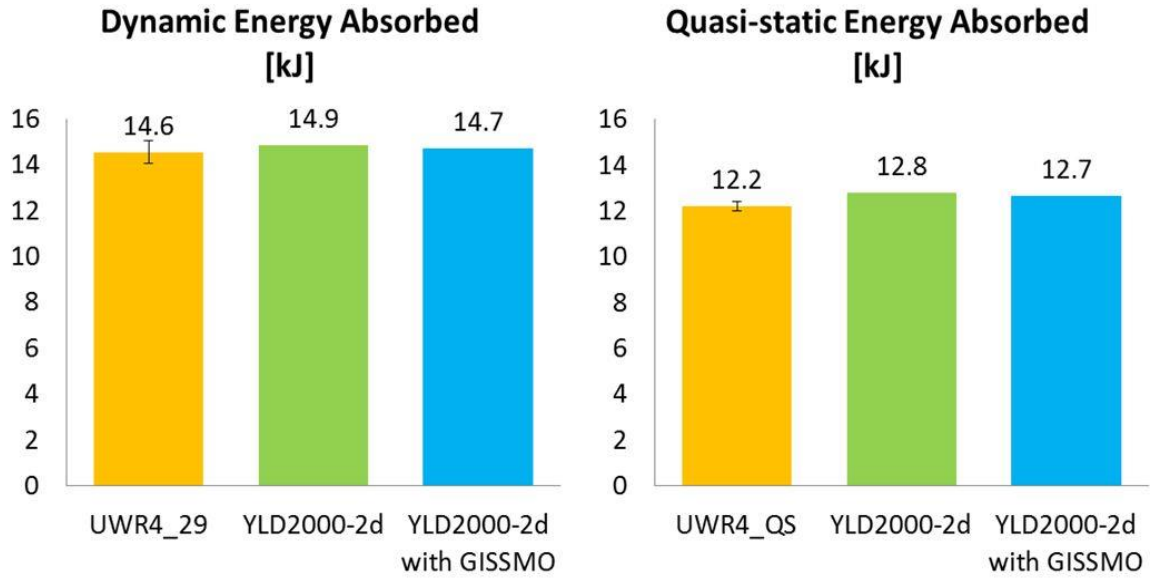

Figure 95 UWR4 axial crush: summary of model predictions and experiments – Absorbed energy

6 Conclusions and Recommendations

6.1 Conclusions

This study has addressed the characterization of the high strain rate constitutive and crash characteristics of the AA6063-T6 extruded Omega and UWR4 crush rails. The following conclusions are drawn from this research:

1. The extruded AA6063-T6 exhibits strong anisotropy in terms of measured r-values which ranged from 0.36 in the extrusion direction, 0.43 in the diagonal direction, to 0.98 in the transverse direction, as well as a biaxial r-value of 0.36;
2. The shear experiments revealed that the material exhibits different hardening behaviours in the extrusion versus the diagonal direction. Such behaviour favours adoption of a differential hardening model; however, this was judged beyond the scope of the current study.
3. The AA6063-T6 exhibited moderate strain rate sensitivity, with an increase in flow stress, measured along the extrusion direction, of approximately 25 MPa for an increase in strain rate from 1 s^{-1} to 1000 s^{-1};
4. The AA6063-T6 UWR4 cross-section developed by Kohar *et al.* [4] exhibited a 36% increase in specific energy absorption (SEA) relative to the AA6063-T6 Omega cross-section (for a 120 mm crush distance).
5. Both rail cross-sections exhibited an increase in SEA with increased loading rate between the quasi-static (0.504 mm/s) and dynamic (7.8 m/s) experiments. The SEA for dynamic loading was 26% higher than the static value for the Omega cross-section and 19% higher for the UWR4 cross-section.
6. The numerical models were able to predict the crush loads and energy absorption to within 5% of the measured values. The predicted dynamic loads were somewhat lower than the measured values whereas the static loads were slightly over-predicted.
7. The error in average load prediction for quasi-static crush experiments was approximately 5% at time scale factor of 2,500.

8. The extent of cracking was higher in the axial crush of UWR4 rails. The numerical models, incorporating the GISSMO [51] calibration due to Nemcko [52] were able to predict the location of cracking very well for both profiles. The extent of cracking was predicted well for the baseline rails, whereas a greater extent of cracking was observed in the UWR4 rails relative to the predictions

6.2 Recommendations

1. Numerical simulation of the axial crush events should consider solid elements (as opposed to the current shell elements) in order to better capture through-thickness stresses and local bending strains in fold regions. Such an approach has been considered by Kohar [73] for these extrusions. This enhancement would require a fully-three dimensional yield surface and fracture criterion and would impose significantly higher computational cost;
2. The strong differential hardening response observed in the shear experiments should be further explored using an advanced constitutive model capable of incorporating such hardening behaviour.
3. Thermal cameras should be used in the tensile and shear experiments in the higher strain rate regime. This would allow the assessment of the adiabatic heating effect on the softening and localization characteristics of the alloy.
4. The axial crush experiments should be performed using DIC techniques to measure local strains. This would allow the validation of the fracture criterion within the fold regions of the rails.

References

[1] O. Lademo, O. S. Hopperstad, and M. Langseth, “An evaluation of yield criteria and ¯ ow rules for aluminium alloys,” *Int. J. Plast.*, vol. 15, no. 749, pp. 191–208, 1999.

[2] P. Oscar and R. L. Eduardo, “Impact Performance of Advanced High Strength Steel Thin-Walled Columns,” *Engineering*, vol. II, no. 0, pp. 2–7, 2008.

[3] J. S. Qiao, J. H. Chen, and H. Y. Che, “Crashworthiness assessment of square aluminum extrusions considering the damage evolution,” *Thin-Walled Struct.*, vol. 44, pp. 692–700, 2006.

[4] C. P. Kohar, A. Zhumagulov, A. Brahme, M. J. Worswick, R. K. Mishra, and K. Inal, “Development of high crush efficient, extrudable aluminium front rails for vehicle lightweighting,” *Int. J. Impact Eng.*, vol. 95, pp. 17–34, 2016.

[5] A. Najafi and M. Rais-Rohani, “Mechanics of axial plastic collapse in multi-cell, multi-corner crush tubes,” *Thin-Walled Struct.*, vol. 49, no. 1, pp. 1–12, 2011.

[6] B. W. Williams, “A study of the axial crush response of hydroformed aluminum alloy tubes,” *ProQuest Diss. Theses*, 2008.

[7] J. M. ALEXANDER, “an Approximate Analysis of the Collapse of Thin Cylindrical Shells Under Axial Loading,” *Q. J. Mech. Appl. Math.*, vol. 13, no. 1, pp. 10–15, 1960.

[8] T. Wierzbicki and W. Abramowicz, “On the Crushing Mechanics of Thin-Walled Structures,” vol. 50, no. 2, pp. 727–734, 1983.

[9] R. J. Hayduk and T. Wierzbicki, “Extensional collapse modes of structural members,” *Comput. Struct.*, vol. 18, no. 3, pp. 447–458, 1983.

[10] W. Abramowicz and T. Wierzbicki, “Axial Crushing of Multicorner Sheet Metal Columns,” *J. Appl. Mech.*, vol. 56, no. March 1989, pp. 113–120, 1989.

[11] W. Chen and T. Wierzbicki, “Relative merits of single-cell, multi-cell and foam-filled thin-walled structures in energy absorption,” *Thin-Walled Struct.*, vol. 39, no. 4, pp. 287–306, 2001.

[12] H. S. Kim, “New extruded multi-cell aluminum profile for maximum crash energy absorption and weight efficiency,” *Thin-Walled Struct.*, vol. 40, no. 4, pp. 311–327, 2002.

[13] M. Langseth and O. S. Hopperstad, “Static and Dynamic Axial Crushing of Square Thin-Walled Aluminum Extrusions,” *Int. J. Impact Eng.*, vol. 18, no. 96, pp. 949–968, 1996.

[14] M. Langseth, O. S. Hopperstad, and T. Berstad, “Crashworthiness of aluminium extrusions: validation of numerical simulation, effect of mass ratio and impact velocity,” *Int. J. Impact Eng.*, vol. 22, no. 9–10, pp. 829–854, 1999.

[15] S. S. Hsu and N. Jones, “Quasi-static and dynamic axial crushing of thin-walled circular stainless steel, mild steel and aluminium alloy tubes,” *Int. J. Crashworthiness*, vol. 9, no. 2, pp. 195–217, 2004.

[16] K. Omer, L. ten Kortenaar, C. Butcher, M. Worswick, S. Malcolm, D. Detwiler, N. Adam, L. ten Kortenaar, C. Butcher, M. Worswick, S. Malcolm, and D. Detwiler, “Testing of a Hot Stamped Axial Crush Member with Tailored Properties – Experiments and Models,” *Int. J. Impact Eng.*, vol. 103, pp. 12–28, 2017.

[17] B. W. Williams, D. a. Oliveira, C. H. M. Simha, M. J. Worswick, and R. Mayer, “Crashworthiness of straight section hydroformed aluminium tubes,” *Int. J. Impact Eng.*, vol. 34, no. 8, pp. 1451–1464, 2007.

[18] R. Grantab, D. a Oliveira, B. W. Williams, M. J. Worswick, and R. Mayer, “Numerical modeling of a dual crush mode welded aluminum crash structure,” *Int. J. Crashworthiness*, vol. 11, no. 2, pp. 165–175, 2006.

[19] R. Smerd, S. Winkler, C. Salisbury, M. Worswick, D. Lloyd, and M. Finn, “High strain rate tensile testing of automotive aluminum alloy sheet,” *Int. J. Impact Eng.*, vol. 32, no. 1–4, pp. 541–560, 2005.

[20] T. Mukai, K. Higashi, and S. Tanimura, “Influence of the magnesium concentration on the relationship between fracture mechanism and strain rate in high purity A1-Mg alloys,” vol. 176, pp. 181–189, 1994.

[21] T. Rahmaan, A. Bardelcik, J. Imbert, C. Butcher, and M. J. Worswick, “Effect of strain

rate on flow stress and anisotropy of DP600, TRIP780, and AA5182-O sheet metal alloys," *Int. J. Impact Eng.*, vol. 88, pp. 72–90, 2016.

[22] G. R. Johnson and W. H. Cook, "A constitutive model and data for metals subjected to large strains, high strain rates and high temperatures," *Proceedings of the 7th International Symposium on Ballistics*, vol. 547. pp. 541–547, 1983.

[23] F. J. Zerilli and R. W. Armstrong, "Dislocation-mechanics-based constitutive relations for material dynamics calculations," *J. Appl. Phys.*, vol. 61, no. 5, pp. 1816–1825, 1987.

[24] E. Voce, "The relationship between stress and strain for homogeneous deformations," *J. Inst. Met.*, vol. 74, pp. 537–562, 1948.

[25] M. T. Rahmaan, "Low to High Strain Rate Characterization of DP600, TRIP780, AA5182-O," University of Waterloo, 2015.

[26] D. M. Bissot, "Development of a constituitive equation for HSLA-100 at cryogenic temperatures," 1987.

[27] A. Bardelcik, M. J. Worswick, and M. A. Wells, "The influence of martensite, bainite and ferrite on the as-quenched constitutive response of simultaneously quenched and deformed boron steel - Experiments and model," *Mater. Des.*, vol. 55, pp. 509–525, 2014.

[28] A. Fjeldly and H. J. Roven, "Observations and Calculations and Plastic Flow on Mechanical Anisotropy and Plastic Flow of an AlZnMg Extrusion," vol. 44, no. 9, pp. 3497–3504, 1996.

[29] A. Fjeldly and H. J. Roven, "Phenomenological modeling of the mechanical anisotropy in AlZnMg extruded profiles," *Mater. Sci. Eng. A*, vol. 234–236, pp. 606–609, 1997.

[30] D. Achani, O. S. Hopperstad, and O. G. Lademo, "Behaviour of extruded aluminium alloys under proportional and non-proportional strain paths," *J. Mater. Process. Technol.*, vol. 209, no. 10, pp. 4750–4764, 2009.

[31] F. Barlat, J. C. Brem, J. W. Yoon, K. Chung, R. E. Dick, D. J. Lege, F. Pourboghrat, S. H. Choi, and E. Chu, "Plane stress yield function for aluminum alloy sheets - Part 1:

Theory," *Int. J. Plast.*, vol. 19, no. 9, pp. 1297–1319, 2003.

[32] F. Barlat, H. Aretz, J. W. Yoon, M. E. Karabin, J. C. Brem, and R. E. Dick, "Linear transfomation-based anisotropic yield functions," *Int. J. Plast.*, vol. 21, no. 5, pp. 1009–1039, 2005.

[33] K. Inal, P. D. Wu, and K. W. Neale, "Large strain behaviour of aluminium sheets subjected to in-plane simple shear," *Model. Simul. Mater. Sci. Eng.*, vol. 10, no. 2, pp. 237–252, 2002.

[34] B. Plunkett, R. A. Lebensohn, O. Cazacu, and F. Barlat, "Anisotropic yield function of hexagonal materials taking into account texture development and anisotropic hardening," *Acta Mater.*, vol. 54, no. 16, pp. 4159–4169, 2006.

[35] K. Inal and R. K. Mishra, "Crystal plasticity based numerical modelling of large strain deformation in hexagonal closed packed metals," *Procedia IUTAM*, vol. 3, pp. 239–273, 2012.

[36] G. Rousselier and M. Luo, "A fully coupled void damage and Mohr-Coulomb based ductile fracture model in the framework of a Reduced Texture Methodology," *Int. J. Plast.*, vol. 55, pp. 1–24, 2014.

[37] W. F. Hosford, "A Generalized Isotropic Yield Criterion," *J. Appl. Mech.*, pp. 607–609, 1972.

[38] F. Barlat and O. Richmond, "Prediction of tricomponent plane stress yield surfaces and associated flow and failure behavior of strongly textured f.c.c. polycrystalline sheets," *Mater. Sci. Eng.*, vol. 95, no. C, pp. 15–29, 1987.

[39] Y. Bai and T. Wierzbicki, "A new model of metal plasticity and fracture with pressure and Lode dependence," *Int. J. Plast.*, vol. 24, no. 6, pp. 1071–1096, 2008.

[40] R. Hill, "A Theory of the Yielding and Plastic Flow of Anisotropic Metals Author (s): R . Hill Source : Proceedings of the Royal Society of London . Series A , Mathematical and Physical Published by : Royal Society Stable URL : http://www.jstor.org/stable/97993 A," *Proceeding R. Soc. London*, vol. 193, no. 1033, pp. 281–297, 1948.

[41] F. Barlat and K. Lian, “Plastic behavior and stretchability of sheet metals. Part I: A yield function for orthotropic sheets under plane stress conditions,” *Int. J. Plast.*, vol. 5, no. 1, pp. 51–66, 1989.

[42] F. Barlat, D. J. Lege, and J. C. Brem, “A six-component yield function for anisotropic materials,” *Int. J. Plast.*, vol. 7, no. 7, pp. 693–712, 1991.

[43] F. Barlat, Y. Maeda, K. Chung, M. Yanagawa, J. C. Brem, Y. Hayashida, D. J. Lege, K. Matsui, S. J. Murtha, S. Hattori, R. C. Becker, and S. Makosey, “Yield function development for aluminum alloy sheets,” *J. Mech. Phys. Solids*, vol. 45, no. 11–12, pp. 1727–1763, 1997.

[44] Z. Chen, “The Role of Heterogeneous Particle Distribution in the Prediction of Ductile Fracture,” University of Waterloo, 2004.

[45] J. Lemaitre, “A Continuous Damage Mechanics Model for Ductile Fracture,” *J. Eng. Mater. Technol.*, vol. 107, no. January 1985, pp. 83–89, 1985.

[46] M. Luo and T. Wierzbicki, “Numerical failure analysis of a stretch-bending test on dual-phase steel sheets using a phenomenological fracture model,” *Int. J. Solids Struct.*, vol. 47, no. 22–23, pp. 3084–3102, 2010.

[47] M. Oyane, T. Sato, K. Okimoto, and S. Shima, “Criteria for ductile fracture and their applications,” *J. Mech. Work. Technol.*, vol. 4, no. 1, pp. 65–81, Apr. 1980.

[48] Y. Bao and T. Wierzbicki, “On fracture locus in the equivalent strain and stress triaxiality space,” *Int. J. Mech. Sci.*, vol. 46, no. 1, pp. 81–98, 2004.

[49] L. ten Kortenaar, “Failure Characterization of Hot Formed Boron Steels with Tailored Mechanical Properties,” University of Waterloo, 2016.

[50] K. Omer, “Development and Testing of a Hot Stamped Axial Crush Member with Tailored Properties,” 2014.

[51] F. Neukamm, M. Feucht, A. Haufe, and D. Ag, “Considering damage history in crashworthiness simulations,” *7th Eur. LS-DYNA Conf. Salzbg.*, 2009.

[52] M. J. Nemcko, C. Butcher, and M. J. Worswick, “Determination of Fracture Loci for Anisotropic AA6063-T6 Extrusions,” *Int. Digit. Imaging Correl. Soc.*, pp. 145–149, 2017.

[53] Y. Prajogo, “Hot Stamping of a Boron Steel Side Impact Beam,” 2015.

[54] C. Butcher, *Personal communication*. Waterloo, 2016.

[55] W. Muhammad, B. A. P., J. Kang, M. R. K., and I. Kaan, “Experimental and numerical investigation of texture evolution and the effects of intragranular backstresses in aluminum alloys subjected to large strain cyclic simple shear,” *Int. J. Plast.*, vol. Accepted, pp. 1–27, 2016.

[56] T. Rahmaan, C. Butcher, A. Abedini, and M. Worswick, “Effect of Strain Rate on Shear Properties and Fracture Characteristics of DP600 and AA5182-O Sheet Metal Alloys,” *11th Int. DYMAT Conf.*, vol. 1033, 2015.

[57] J. Peirs, P. Verleysen, and J. Degrieck, “Novel Technique for Static and Dynamic Shear Testing of Ti6Al4V Sheet,” *Exp. Mech.*, vol. 52, no. 7, pp. 729–741, 2012.

[58] A. Abedini, C. Butcher, D. Anderson, M. Worswick, and T. Skszek, “Fracture Characterization of Automotive Alloys in Shear Loading,” *SAE Int. J. Mater. Manuf.*, vol. 8, no. 3, 2015.

[59] A. Abedini, C. Butcher, and M. J. Worswick, “Fracture Characterization of Rolled Sheet Alloys in Shear Loading: Studies of Specimen Geometry, Anisotropy, and Rate Sensitivity,” *Exp. Mech.*, pp. 1–14, 2017.

[60] A. Abedini, C. Butcher, M. J. Nemcko, S. Kurukuri, and M. J. Worswick, “Constitutive Characterization of Rare-Erath Magnesium Alloy Sheet,” *Int. J. Mech. Sci.*, no. DOI: 10.1016/j.ijmecsci.2017.04.013, 2017.

[61] J.-W. Yoon, F. Barlat, R. E. Dick, K. Chung, and T. J. Kang, “Plane stress yield function for aluminum alloy sheets—part II: FE formulation and its implementation,” *Int. J. Plast.*, vol. 20, no. 3, pp. 495–522, 2004.

[62] D. Steglich, X. Tian, J. Bohlen, and T. Kuwabara, “Mechanical Testing of Thin Sheet

Magnesium Alloys in Biaxial Tension and Uniaxial Compression," *Exp. Mech.*, vol. 54, no. 7, pp. 1247–1258, 2014.

[63] S. Kurukuri, M. J. Worswick, D. G. Tari, R. K. Mishra, and J. T. Carter, "Rate sensitivity and tension – compression asymmetry in AZ31B magnesium alloy sheet," *Phil. Trans. R. Soc. A*, vol. 372, pp. 1–16, 2014.

[64] S. Kurukuri, D. G. Tari, M. J. Worswick, R. K. Mishra, and J. T. Carter, "Dynamic Characterization of Az31B and Zek100 Magnesium Alloy Sheets," *9th Int. Conf. Magnes. Alloy. Their Appl.*, no. August, pp. 2–7, 2012.

[65] Y. H. Wang, J. H. Jiang, C. Wanintrudal, C. Du, D. Zhou, L. M. Smith, and L. X. Yang, "Whole field sheet-metal tensile test using digital image correlation," *Exp. Tech.*, vol. 34, no. 2, pp. 54–59, 2010.

[66] A. M. Sutton, J.-J. Orteu, and W. H. Schreier, *Image Correlation for Shape, Motion and Deformation Measurements: Basic Consepts, Theory and Applications*, vol. 1. Springer Science+Business Media, LLC, 2009.

[67] T. Rahmaan, A. Abedini, C. Butcher, N. Pathak, and M. J. Worswick, "Investigation into the shear stress , localization and fracture behaviour of DP600 and AA5182-O sheet metal alloys under elevated strain rates," *Int. J. Impact Eng.*, no. DOI:10.1016/j.ijmecsci.2017.04.013.

[68] T. Tryland, O. S. Hopperstad, and M. Langseth, "Design of experiments to identify material properties," *Mater. Des.*, vol. 21, no. 5, pp. 477–492, 2000.

[69] A. H. Clausen, T. Tryland, and S. Remseth, "An investigation of material properties and geometrical dimensions of aluminium extrusions," 2001.

[70] S. Onaka, "Equivalent strain in simple shear deformation described by using the Hencky strain," *Philos. Mag. Lett.*, vol. 90, no. 9, pp. 633–639, 2010.

[71] T. Rahmaan, *Personal communication*. Waterloo, 2016.

[72] "http://www.engineeringtoolbox.com/friction-coefficients-d_778.html." [Online].

Available: http://www.engineeringtoolbox.com/friction-coefficients-d_778.html. [Accessed: 20-Jan-2016].

[73] C. P. Kohar, A. Brahme, R. K. Mishra, and K. Inal, “Effects of Coupling Anisotropic Yield Fucntions with the Optimization Process of Extruded Aluminum Front Rail Geometries in Crashworthiness,” *Int. J. Solids Struct.*, vol. Under revi, no. (IJSS-S-16-01573), 2017.